Title
Eccentric Planets around Evolved Stars

Author
Frewen, Shane Franklin Nishi

Publication Date
2015

Peer reviewed|Thesis/dissertation

University of California
Los Angeles

Eccentric Planets Around Evolved Stars

A dissertation submitted in partial satisfaction
of the requirements for the degree
Doctor of Philosophy in Astronomy

by

Shane Franklin Nishi Frewen

2015

Abstract of the Dissertation

Eccentric Planets Around Evolved Stars

by

Shane Franklin Nishi Frewen

Doctor of Philosophy in Astronomy

University of California, Los Angeles, 2015

Professor Bradley M. Hansen, Chair

Planets are now known to be near ubiquitous around main-sequence stars in our galaxy, as evidenced by the results of radial velocity and transit surveys such as the *Kepler* mission. In spite of this accomplishment, our understanding of how planetary systems form and are affected by stellar evolution is far from complete. Observations of polluted white dwarfs, which show evidence for planetesimal accretion in their atmospheres, indicate that planets must be orbiting them in order to perturb planetesimals into their tidal radius. Yet no planets have themselves been detected, leaving the population uncharacterized. Meanwhile, main-sequence stars host a significant number of eccentric warm jupiters, massive planets orbiting on 10- to 100-day periods, which are not observed around evolved stars. These planets were likely born at much larger distances, but the mechanism by which they migrated inward remains unclear.

This dissertation is composed of two projects, each investigating one of these populations. In the first I use numerical simulations to test eccentric planets as the source of white dwarf pollution, finding a strong relationship between planetary properties and the white dwarf accretion rate. Small and eccentric planets prove to be the most efficient perturbers, capable of producing the observed pollution levels so long as the surviving disk of planetesimals is massive enough. In the second I test the hypothesis that warm jupiters are migrating as a result of large oscillations in eccentricity caused by a more distant planet. Our numerical simulations show that these oscillations lead to planetary removal earlier in the evolution of

the host star than constant eccentricity, and can explain the observed lack of warm jupiters around evolved stars.

The dissertation of Shane Franklin Nishi Frewen is approved.

Kevin D. McKeegan

Jean-Luc Margot

Bradley M. Hansen, Committee Chair

University of California, Los Angeles

2015

To my grandfather,

the first scientist I ever met

Table of Contents

List of Figures

Acknowledgments

This dissertation never would have happened if it weren't for the constant love and support of so many people in my life. First and foremost, my family: I owe this thesis to you. For instilling a love of learning from before I can remember, for always being excited about my work and my interests, even when they didn't make sense, and for teaching me that life is an adventure worth exploring, I thank you from the bottom of my heart. I'd be remiss if I didn't also include the family I've gained along the way: the Gallivans, the Baileys, and Dr. Myles Herbert. I never felt far from home in the last six years.

I would like to thank the entire UCLA astronomy graduate community. I honestly can't imagine a better group of people to work with day in and day out. To Nate Ross, Robin & Thomas Rehagan, Tom Esposito: I am so lucky to have been a part of such a wonderful, fun class. I'm so excited for us to move on to the next stage of our lives, pursuing such incredible array of careers. To Breann Sitarski and Laura Vican, champions of *Astronomy Live!*: I feel so priviledged to have worked closely with two people who have done such amazing things for education and outreach at UCLA. And to Fred Davies, whose enthusiasm for astronomy was a constant source of motivation for me. I look forward to seeing the amazing things that everyone will accomplish in the coming years.

I'd also like to thank many of the alumni of UCLA, who meant so much to my grad career. First, Greg Mace and Kristin Kulas, who created something amazing when they started *Astronomy Live!* and without whom I wouldn't have discovered my passion for education. Ian Crossfield, as a mentor not just to me but to many of the grads, for his kindness and mentorship even when our fields were completely different. Kathy Kornei, who showed me that you could do more with an astronomy doctorate than a postdoc. Kevin Hainline, who showed me what it meant to do outreach and whose passion for teaching is an inspiration for graduate students.

I would also like to thank my advisor Brad Hansen, for his stalwart support and understanding, even when I decided to take a very different path than his.

Finally, I would like to thank my wife, Lindsay Frewen. For her infinite patience, strength, and understanding, who showed me that even if I don't believe in myself, there's always someone does. I love you so incredibly much.

Chapter 2 of this dissertation is a version of Frewen & Hansen (2014) and is reproduced by permission of Oxford Journals. We thank Ian Crossfield, Julia Fang, and Siyi Xu for their helpful comments. This work was supported by NASA grant HST-G0-12971.01

Chapter 3 is based on a version of a soon-to-be published article. I thank Smadar Naoz for her tremendous assistance, including use of her secular code and useful manuscript comments, as well as Jean-Luc for his comprehensive comments. This work was supported by the UCLA Dissertation Year Fellowship.

Vita

2009	B.A. (Physics, Astrophysics) University of California, Berkeley.
2012	M.S. (Astronomy) University of California, Los Angeles.

Publications and Presentations

Frewen, S. & Hansen, B. *The Effect of Stellar Evolution on Kozai-Lidov Oscillating, Migrating Warm Jupiters.* To be submitted June 2015

Hansen, B., Richer, H., Kalirai, J., Goldsbury, R., Frewen, S., & Heyl, J., *Constraining Neutrino Cooling using the Hot White Dwarf Luminosity Function in the Globular Cluster 47 Tucanae.* Submitted to ApJ on May 3, 2015

Frewen, S. & Hansen, B. *Eccentric Planets and Stellar Evolution as a Cause of Polluted White Dwarfs*, 2014, MNRAS, 439, 2442

Eccentric Planets and Stellar Evolution as a Source of Polluted White Dwarfs, Planets Around Stellar Remnants, Arecibo, PR, Jan. 2012

Orbital Stability of Test Particles over the Course of Stellar Evolution, Theoretical Astrophysics in Southern California Meeting, Pasadena, Ca, Oct. 2010

Hudson, H., MacKinnon, A., De Rosa, M., & Frewen, S. *Coronal Radiation Belts*, 2009, ApJ, 698, 86

CHAPTER 1

Introduction

Planetary systems around other stars have now been studied for nearly twenty years; as a result, a great deal of information has been collected regarding the nature of planets around a wide variety of main-sequence (MS) stars. Surveys measuring stellar radial velocities and planetary transits have detected over 1,800 planets, along with thousands of planetary candidates (Mullally et al., 2015). Careful analysis of observations has also determined planetary properties, including masses, sizes, and orbital parameters, proving that extrasolar planets are a hugely diverse population. Perhaps somewhat surprisingly, a significant number of these planets are different from anything that exists in our solar system. Arguably the most dramatic example is the population of extrasolar planets first to be discovered: hot jupiters (HJ). These massive planets orbit on periods under than 10 days, which is less than 10 percent that of Mercury (Mayor & Queloz, 1995; Butler et al., 1997). While HJs are far from the most common type of extrasolar planet, having been detected first due to their high detectability rather than ubiquity, their existence points to physical processes which do not, or no longer, play a role in our own solar system.

The differences between extrasolar planets and our solar system extend outside of this short-period regime as well. Warm jupiters (WJs) are an unexpected population of extrasolar planets that, like HJs, are too near to their host to have formed in situ, but are distant enough to retain a significant eccentric population. Notably, while the largest eccentricity in our solar system is 0.21 (Mercury), radial velocity surveys have shown that exoplanets with periods longer than 10 days have a wide range of eccentricities (Butler et al., 2006), and a cursory examination of the current Exoplanet Orbit Database (Wright et al., 2011) shows that over 50 percent of such planets have eccentricities larger than 0.2 (Figure 1.1).

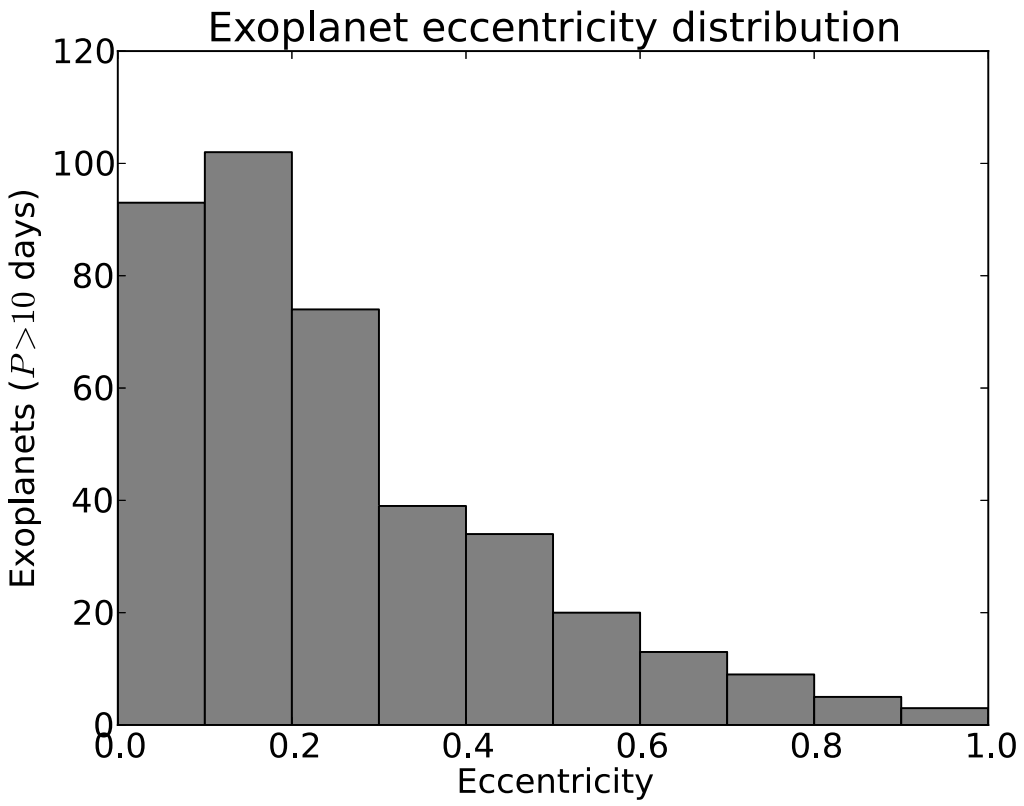

Figure 1.1 The distribution of eccentricities for planets with periods longer than 10 days, from the Exoplanet Orbit Database (Wright et al., 2011). The substantial tail above at eccentricities greater than 0.2 composes over 50 percent of the planets, highlighting the importance of understanding planetary eccentricity in exoplanet systems.

This result has important implications for the formation of both exoplanets and exoplanet systems, as well as their fate during and after stellar evolution.

Meanwhile, only recently have planet searches begun to probe the existence of planets around evolved stars, so the manner in which stellar evolution affects planetary systems is still far from understood (Johnson et al., 2007, 2011). While gradual expansion occurs during the MS, stars increase in radius by more than an order of magnitude after core hydrogen fusion is finished and they evolve onto the giant branch. This growth can have dramatic effects on an orbiting planetary system, causing planets to be removed by engulfment or inspiral via tides and stellar wind drag. Additionally, large amounts of mass loss occur near the end of stellar evolution as the star evolves into a white dwarf (WD), leading to orbital

expansion for surrounding material. Because of these effects, stellar evolution is likely to play an important role in a range of planetary systems. This dissertation consists of two projects, both investigating planetary systems where eccentricity and stellar evolution play a major role.

As of 2015, no planet has been observed around a WD. The large surface gravity requires massive, close-in planets to produce radial velocity signals that are detectable, and their small size lowers the probability of a planet transit occuring. However, a significant fraction of WDs are observed to be polluted with metals, in spite of having high surface gravities and short settling times. The current model for this pollution is accretion of rocky bodies, which are delivered to the WD through perturbations by orbiting planets. While these inferred planets are believed to be orbiting a significant number of WDs, due to the high rate of pollution, their physical and orbital properties are only very weakly constrained.

Chapter 2 is an examination of single planet systems around WDs and their effect on a co-orbiting disc to better understand these properties. Using N–body simulations, we examine the possibility that a single planet is the source of WD pollution. We determine the stability of test particles on circular orbits in systems with a single planet located at 4 AU for a range of masses and eccentricities, comparing the fractions that are ejected and accreted by the star. In particular, we compare the instabilities that develop before and after the star loses mass to form a WD, a process which causes the semi-major axes of orbiting bodies to expand adiabatically. We determine that a planet must be eccentric ($e > 0.02$) to deliver significant (> 0.5 per cent) amounts of material to the central body, and that the amount increases with the planetary eccentricity. We also find that the efficiency of the pollution is enhanced as planetary mass is reduced. We demonstrate that a 0.03 M_{Jup} planet with substantial eccentricity ($e > 0.4$) can account for the observed levels of pollution for initial disc masses of order 1 $M_{\oplus}$.

Chapter 3 is our study of migrating WJs undergoing eccentricity oscillations and the effect of stellar expansion on their population (Frewen & Hansen, in prep.). We investigate Kozai-Lidov oscillations as a cause for their absence around evolved stars, with the planets being engulfed or dragged in by their host during tidal evolution. Using numerical simulations we

determine the relationship between periapse distance and orbital migration rate for planets 0.1 to 10 Jupiter masses and and the period range 10 to 100 days. We find that Kozai-Lidov oscillations effectively result in planetary removal early in the evolution of the host star, possibly accounting for the observed deficit. While the observed eccentricity distribution is inconsistent with the simulated distribution for and oscillating and migrating WJ population, observational biases may explain the discrepancy.

CHAPTER 2

Eccentric planets and stellar evolution as a cause of polluted white dwarfs

Reproduced by permission of Oxford Journals
(Frewen, S. & Hansen, B. 2014, MNRAS, 439, 2442)

2.1 Introduction

Studies of hydrogen-dominated (DA) and helium-dominated (DB) WD spectra have found that roughly 25 per cent of all WDs show weak metal lines, despite the theoretical prediction that metals should gravitationally settle below the photosphere (Zuckerman et al., 2003; Koester, 2009; Zuckerman et al., 2010). Given settling time-scales as small as days for the more-common DAs and under 10^5 years for DBs, the rapid rate at which gravitational settling occurs in these dense objects indicates the pollution must have occurred recently compared to their cooling ages and is likely ongoing (Paquette et al., 1986; Koester & Wilken, 2006; Koester, 2009). Furthermore, infrared excesses have been detected in a number of these WD systems (Zuckerman & Becklin, 1987; von Hippel et al., 2007; Farihi et al., 2009; Xu & Jura, 2012). The cause of these excesses appears to be debris disks near the WDs, which are delivering the polluting material (Chary et al., 1999; Jura, 2003; Kilic et al., 2006). These detections support the theory that the observed pollution is due to accreted orbiting bodies, which are perturbed towards and tidally disrupted by the central WD (Jura, 2006). The primary alternative, accretion of interstellar material, has been proven inconsistent with elemental abundances determined from WD spectra (Jura, 2006; Klein et al., 2010; Farihi et al., 2010a; Klein et al., 2011) as well as spectra of the debris disks (Reach et al., 2005;

Jura et al., 2009). Estimates for total mass accreted by polluted WDs are on the order of 6×10^{23} g, which is similar to the mass of minor bodies in the solar system such as Ceres (Zuckerman et al., 2010).

While the source of the pollution has become more clear in recent years, the mechanism for delivering such material to the star is still uncertain. Early work investigated the possibility that planetary systems close to instability during the main sequence (MS) can be destabilized by stellar mass loss during post-MS evolution (Debes & Sigurdsson, 2002). Upon scattering, the planets could settle into a new, dynamically-young configuration that would allow them to perturb other orbiting bodies, such as asteroids or comets, that were previously stable. However, the high frequency of polluted WDs means this mechanism would require a large fraction of WD progenitors to have planetary systems on the edge of stability.

More recently, Bonsor et al. (2011) simulated planets on circular orbits interacting with a Kuiper-Belt analog over the course of stellar evolution. To determine the ability of the planet to pollute its host WD, the authors looked at the fraction of bodies scattered into the inner solar system, interior to the orbit of the planet. They did not simulate impacts with the WD; instead, they assumed additional planets in this region, which could further scatter bodies. The authors found that a planet near 30 AU and a Kuiper Belt analog extending to 46.7 AU could match the observed frequency of polluted WDs as well as the distribution of accretion rates as a function of cooling age. This result requires an inner planetary system to cause secondary scatterings, which delivers the material the full distance to the WD; a lone planet at 30 AU was unable to scatter particles on to stellar-collision orbits. Bonsor et al. (2011) also found that the mass of the simulated planet had only a weak effect on the amount of material delivered to the inner system. While massive planets removed more bodies from the original belt, higher fractions were ejected relative to less-massive planets.

Another recent work, Debes et al. (2012), focused on rocky bodies interior to a planet as source of pollution. The authors examined the ability of a single planet to deliver material originating in the inner 2:1 Mean Motion Resonance (MMR) to a WD, through the increase in resonance width with stellar evolution. Using Jupiter and the asteroids located near the 2:1 MMR as a test case, they found that a single planet is capable of delivering enough

material to the star provided the interior debris belt is large enough. Assuming a similar size distribution to the solar system asteroid belt, the authors determined that the total mass of the debris belt would need to be between 4 times and 6×10^5 times larger to account for WD observations. While massive debris disks have been observed, they often exist at greater distances from their host star (Wyatt, 2008) and their incidence appears to drop off rapidly with age (Rieke et al., 2005).

In a paper related to Debes & Sigurdsson (2002), Veras et al. (2013) examined the stability of two-planet systems over the entirety of stellar evolution, including MS, post-MS (including mass loss), and WD. The authors performed N-body integrations of the system for stellar masses 3–8 $M_\odot$, with equal planetary masses of both $M_{\rm Jup}$ and $M_\oplus$. They found that planetary interactions leading to ejection or accretion by the star primarily occurred after $\sim 10^7$ years, supporting the possibility of planetary instability as a source of WD pollution. However, in addition to selecting large stellar masses dissimilar to the progenitors of observed polluted WDs (1–2.5 $M_\odot$), the authors did not investigate the effect of the unstable planets on planetesimals remaining in the system, which limits the applicability of their results to WD pollution.

In this work we use N-body simulations of a single planet and massless test particles (TPs) to systematically examine the degree to which planetary properties affect WD pollution. In particular, we investigate the influence of planetary mass and eccentricity, which have largely been neglected in this context until now. Radial velocity surveys have shown that exoplanets orbiting beyond 0.1 AU have a wide range of eccentricities (Butler et al., 2006), and a cursory examination of the current Exoplanet Orbit Database shows that over over 50 per cent of such planets have eccentricities larger than 0.2 (Wright et al., 2011). Therefore, testing a range of eccentricities for the perturbing planet gives us greater generality than before as well as insight into the overlooked parameter space of eccentric planets. Additionally, high-resolution spectroscopy has shown that the accreted material is more consistent with the composition of solar-system asteroids or the rocky planets than comets (Zuckerman et al., 2007; Klein et al., 2010). As a result, we investigate the region near to the star interior and exterior to planetary orbit, as opposed to the distant planet and outer belt of material used

in Bonsor et al. (2011). Furthermore, we simulate the entire region near the planet unlike the very detailed, single-MMR approach of Debes et al. (2012). These simulations allow us to better understand the ability of a single planet to account for observed WD pollution rates, particularly as a function of planetary mass and eccentricity.

The layout of the paper is as follows: In Section 2 we review important features of the dynamics we expect to occur in the systems simulated. In Section 3 we discuss the setup and results of our initial simulation, and repeat that for a range of masses and eccentricities in Section 4 where we find that smaller and more eccentric planets are more efficient at delivering material to the host star. Section 5 details the theoretical effects of stellar evolution, and Section 6 presents the results of our WD simulations along with a comparison to the MS simulations, which show that stellar evolution can result in a significant population of newly unstable bodies. We finish with a discussion of results and comparison to other work in Section 7 and a conclusion in Section 8.

2.2 System Dynamics

The classical orbit of a single body in the gravitational field of a star will be a Keplerian ellipse, fixed in space. However, the orbit of a third, small body, such as an asteroid, will be affected by both the star and the planet and as a result be non-integrable. The orbit of such a body can be rapidly and dramatically changed upon close encounters with the planet, leading to ejection or collision with the star. In the case of bodies much less massive than the planet, the planetary orbit will remain unchanged. Beyond scattering, the orbits of small bodies can be perturbed by planets through both global secular effects and localized resonant effects. Through secular effects, orbits near an eccentric planet will slowly increase in eccentricity. This contribution is called 'forced eccentricity': it is greatest for orbits near the planet and drops off with distance. As eccentricity increases so does the likelihood of scatterings, which further alters the orbit.

Resonant effects occur at MMRs, and result from repeated encounters between bodies near the same location or locations over each orbit. These encounters can produce a rapid

evolution of orbital elements such as eccentricity, or can act as a protection mechanism by preventing closer encounters between two bodies for long periods of time. MMRs are highly-localized and as such relatively small shifts in semi-major axis (SMA) can dramatically alter the stability of orbiting bodies, as will be shown in Section 2.4. MMRs exist where the mean motions of two bodies form an integer ratio:

$$\frac{n_2}{n_1} = \frac{p}{p+q} \tag{2.1}$$

Here n_1 and n_2 are the mean motions of the inner and outer bodies, respectively, while p and q are integers. For orbits interior to the planet, the resonance is given by $p+q : p$ (so that n_1 is the mean motion of the planet), while for exterior orbits the resonance is $p : p+q$, with n_2 being the mean motion of the planet. The strength of the resonance is determined in part by the order of the resonance, q: smaller q values generally correspond to stronger resonances. However, at larger planetary eccentricities higher-order MMRs are no longer negligible, which increases the number of trapping regions for small bodies. Particles located in resonances have been shown to become unstable at late times (Wisdom, 1982; Debes et al., 2012), indicating that unstable MMRs will not be immediately cleared of bodies and can function as a source of material for the star even at late times.

2.2.1 The nominal chaotic zone

MMRs have a finite width that is determined by both the planet causing them, via its eccentricity and planet-to-star mass ratio, as well as the location and order of the resonance (Murray & Dermott, 2000). As described in Chirikov (1979), when resonances overlap in a system it results in stochastic motion and orbital instability. In the context of planetary systems, as p increases and the mean motion of the orbit approaches that of the planet, first-order ($q = 1$) MMRs are spaced more closely and eventually overlap. This region of overlap is known as the 'chaotic zone' (CZ) and within it orbits are chaotic, frequently becoming unstable. Wisdom (1980) showed that for a planet on a circular orbit, nearby bodies become unstable when the distance between them is

$$\varepsilon = \frac{a - a_p}{a_p} < 1.3\mu^{2/7} \tag{2.2}$$

where a and a_p are the SMAs of the nearby body and planet, respectively, and $\mu = \mathrm{M_{Pl}}/\mathrm{M_*}$ is the mass ratio between the planet and the central star. Numerical work by Duncan et al. (1989) showed the same mass dependence with a slightly different coefficient:

$$\varepsilon_{\mathrm{cz}} = 1.5\mu^{2/7} \tag{2.3}$$

This equation indicates that larger planets produce larger CZs, for constant stellar mass. However, a corresponding equation for planets with moderate eccentricity does not exist: such a planet causes orbits of a third body to be non-integrable. Finally, this mass-ratio dependence also has important implications for the system as the star evolves off the MS, which will be covered in Section 2.5.

From the preceding paragraphs we can predict the general behavior of small bodies in the presence of a massive planet: Those closest to the planet will start between planetary periapse and apoapse, and will rapidly be removed from the system by a collision or scattering in close encounter. Particles beyond the physical reach of the planet will be inside the CZ, and will likely go unstable as orbits become chaotic. Beyond the CZ, most particles should be stable with slight eccentricities, caused by secular effects. The exception is particles in MMRs, which may show anomalous behavior both in the CZ, where they may be more stable than their neighbors, and outside of the CZ, where they may be more unstable. Of those that are removed from the system, particles inside the orbit of the planet should have a higher likelihood of being accreted by the star, while those beyond the planet, being more weakly bound, should show a greater preference for ejection.

2.3 The first simulation

Due to the non-integrable nature of planetary systems with an eccentric planet and other bodies, we required numerical simulations to determine the orbital behavior of the small

bodies. We began by simulating a MS star and a planet of moderate eccentricity, for the purposes of comparing the results to our predictions from Section 2.2. While we are primarily interested in the accretion rates around WDs, simulating a planet around both a MS and WD star allowed us to compare the dynamics of the system and understand the effect of stellar evolution.

2.3.1 Setup

Our first simulation was composed of a solar-mass star, a single 0.3 M_{Jup} planet orbiting with $a_p = 4$ AU and $e = 0.2$, and 500 massless TPs distributed throughout the system. The stellar mass was selected due to the high frequency of solar-mass stars relative to more-massive stars, as well as for consistency with prior papers on the subject, specifically Bonsor et al. (2011) and Debes et al. (2012). The planetary parameters were chosen to match theoretical predictions: exoplanets near to their host star will not survive post-MS evolution (Rasio et al., 1996), but distant planets are unlikely to direct as much material to the star. To balance each factor the SMA was chosen to be 4 AU, while the mass was selected to be in the middle of the observed eccentric exoplanet population, similar to 0.27 M_{Jup} eccentric Saturn-analog OGLE-2006-BLG-109L c (Gaudi et al., 2008; Bennett et al., 2010).

The TPs were spaced 0.02 AU apart from 0.06 AU to 10 AU, allowing us to determine stability at a range of locations. While the planet was placed on an eccentric orbit, the TPs were placed on circular orbits at random mean longitudes. This decision was made for simplicity, and represents the case where secular effects have not had time pump the eccentricities of small bodies. Such a situation could occur in a young disk recently void of gas, or if the planet gained eccentricity impulsively (as would be the case in the model of Debes & Sigurdsson (2002)). Non-zero initial eccentricities are discussed later in Section 2.4.5. In addition, each TP was assigned a random inclination within 0.5° of the planet to avoid the artificial constraint of perfect coplanarity. The particles were assumed to be massless because of the minute mass estimated to be accreted by polluted WDs ($\sim 5 \times 10^{-7}$ M_{Jup}) compared to our planet size, indicating a negligible effect by polluting material on the

planet.

We also ran separate simulations of the strongest MMRs in greater detail: three interior to the planet at 3:1, 2:1, and 3:2; three exterior at 2:3, 1:2, and 1:3; and one co-orbital. We populated these resonances over a width of 0.2 AU with a higher density of TPs, spacing them 0.004 AU apart, and assigned them the same orbital properties as above. Additionally, we simulated a second set in the same locations with the same spacing but with an initial eccentricity of 0.2 to match the planet. The initial longitude of periapse of these remained random for consistency between all simulations. These non-circular TPs allowed us to determine the sensitivity of processes and results on initial eccentricity, particularly if it could lead to increased stability over the duration of the simulation. Additionally, by comparing these two very closely spaced populations we were able to test the dependence of the loss mechanism on the initial mean longitude, which was random for all particles.

During the simulations TPs were removed via one of three mechanisms: ejection from the system, occurring at 100 AU; collision with the planet, which had a radius of 0.65 R_{Jup} given the assumed planetary density of 1.33 g cm^{-3}; or accretion by the central body, occurring when particles approached within 0.005 AU. TPs that survived the ∼100 million year duration of the simulation were considered stable. The ejection radius was chosen to limit computation time, and it was found that increasing it to 1000 AU had a negligible effect on the simulation results: the stability of particles was identical and the average lifetime in log space increased by less than five per cent. It should be noted that the majority of polluted WDs show cooling ages greater than the duration of our simulations, ranging from $10^{7.5}$ to 10^{10} years (Debes et al., 2012). Such time-spans were computationally too expensive to run for this work, so behavior late in the simulations (10^6–10^8 years) was used as a proxy.

2.3.2 Computation

We ran the simulation, as well as those in Sections 2.4 and 2.6, on the UCLA Institute for Digital Research and Education (IDRE) Hoffman2 cluster using the Mercury integrator package (Chambers, 1999). The package contains five N-body algorithms; we initially chose

the hybrid symplectic integrator, which primarily uses a second-order mixed-variable symplectic algorithm and switches to a Bulirsch-Stoer (BS) algorithm upon close encounters, in our case 3 Hill radii. This combination has the advantage of shorter integration times than non-symplectic algorithms (e.g. BS) while still allowing close encounters, which are crucial for the scattering and accretion of TPs.

To test the accuracy of the hybrid integrator we repeated the simulation using the non-symplectic BS integrator. We found that, while the former was faster and accurate in determining the stability of TPs in our simulations, the loss mechanism for a given particle was frequently inconsistent with the latter. The difference originates from the known issue that the hybrid integrator has difficulty with very large eccentricities (Chambers, 1999), as in the case of accreted particles. As a result, particles are ejected when they should be accreted, as shown in Figure 2.1. Given the importance of the accretion fraction on the stellar accretion rate, it was necessary for us to use the most accurate method available within the constraints of computation time. Therefore we used the hybrid simulation to determine the size of the unstable zone around the planet, which defined our eccentric chaotic zone (ECZ), and followed with a simulation of the ECZ using the BS integrator. We defined the edges of the ECZ as the region nearest to the planet having 19 out of 20 adjacent TPs stable (corresponding to a 0.4 AU wide region with at least 95 per cent of small bodies stable), to ideally include all major instabilities near the planet. We integrated the MMRs using only the BS integrator, as they were narrow and unique in stability relative to the surrounding region.

2.3.3 Results

Upon completion, the simulation returned the orbital elements as a function of time, the loss mechanisms, and the lifetimes of each individual TP. As shown in Figure 2.1, TPs that started near the planet rapidly went unstable, forming the ECZ between the range of ~ 2.4 and ~ 6.3 AU. Inside of this region some islands of stability existed, corresponding to low-order MMRs such as 2:1 and 3:4 at 3.05 and 4.85 AU, respectively. The size of this ECZ

was much larger than the predicted CZ for a planet on a circular orbit, which according to Equation 2.3 should have extended from 3.4 to 4.6 AU.

Individual particle motion depended on interactions with the planet and varied not only between TPs, but over the course of the simulation as well. One particle, representative of many others, started at 5.3 AU and remained in the 2:3 MMR for nearly 400,000 years before scattering and undergoing chaotic motion (Figure 2.2). This particle appeared to be trapped in other MMRs during the remainder of the simulation, including the 1:2 resonance at 425,000 years and the 2:1 resonance at 725,000 years, shortly before accretion. Many unstable particles showed similar orbital motion that varied dramatically over the course of the simulation, spending some time apparently trapped in MMRs between periods of more chaotic motion, eventually being ejected or accreted as the eccentricity approached unity. Particles that collided with the planet also showed such motion, but failed to reach highly-eccentric orbits before being removed early in the simulation.

The final fates of particles were influenced by their starting locations: Particles that were accreted generally retained an apoapse near the planet, increasing in eccentricity through scattering until periapse reached the surface of the star. Particles that were ejected often did so with a periapse near the planet, as both the SMA and eccentricity increased. Because of this behavior, a larger fraction of unstable particles starting interior to the planet were accreted (24 per cent) than exterior (14 per cent). However, particles were lost via all three mechanisms in both starting regions due to chaotic motion.

The higher-density MMR simulations were analyzed separately and showed consistency with the above results, including behaving as islands: particles starting very near to some low-order MMRs, such as the 2:3 and 3:2 resonances, were much more stable than the surrounding particles (Figure 2.3, top). Additionally, the 2:1 resonance was found to be a major source of accreted particles at late times. Within 0.1 AU of the resonance, 15 out of 16 unstable particles were accreted and 11 of those survived more than 1 million years. The $e = 0.2$ populations in each MMR were also stable in some of the same locations, but in general had shorter lifetimes. This result was evidence that such particles would be more rapidly removed from a planetary system, and TPs that were started on circular orbits more

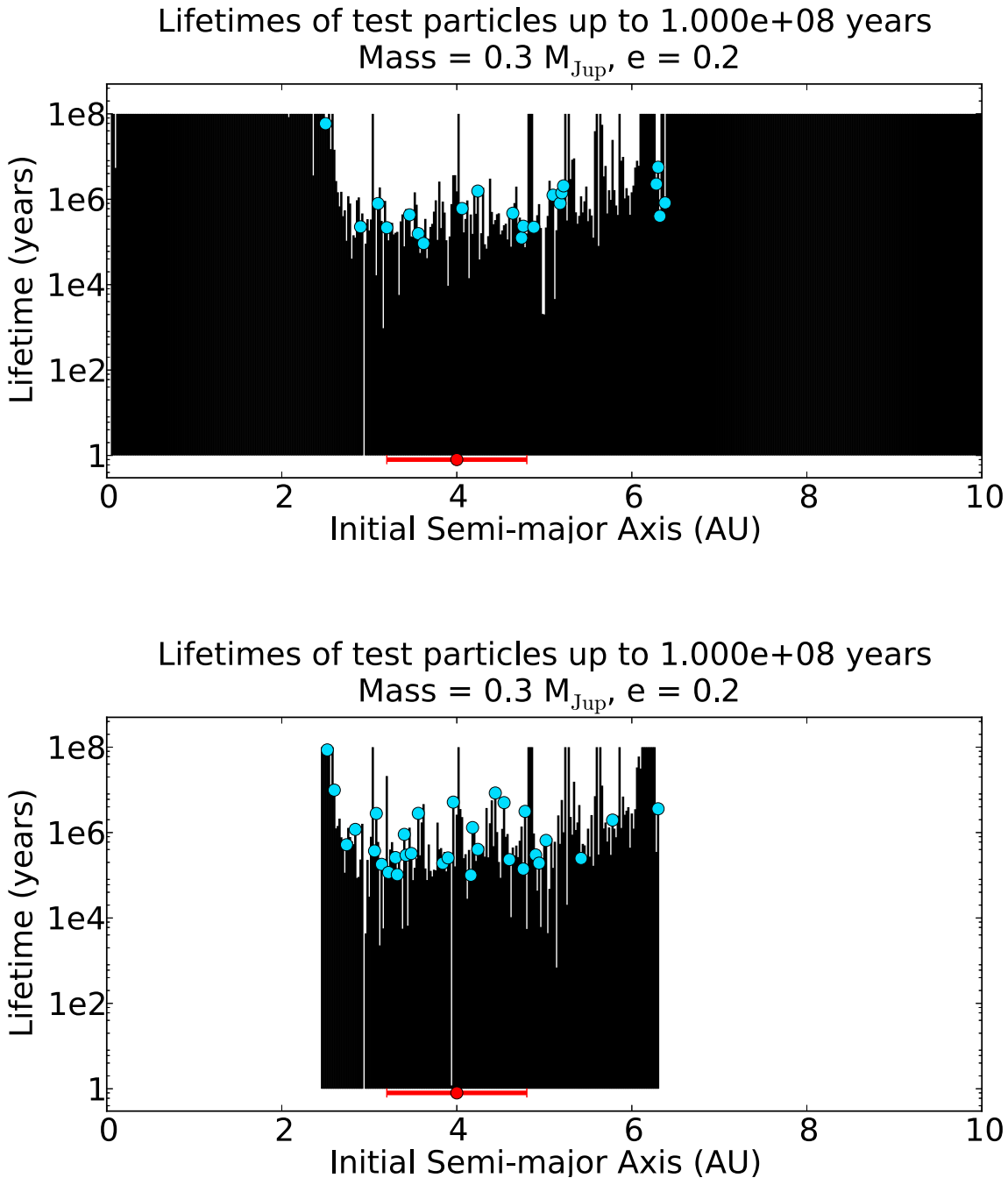

Figure 2.1 Comparison of hybrid integrator (top) and BS integrator (bottom) results, showing particle lifetime as a function of initial SMA. Note the similarity in stability of TPs (black lines) around the planet (red point, error bars for periapse and apoapse), but the difference in number of accreted particles (cyan points): 21 particles in the hybrid case and 31 in the BS case. Simulations using the BS integrator were limited to regions with unstable particles to reduce computation time, as described in Section 2.3.2.

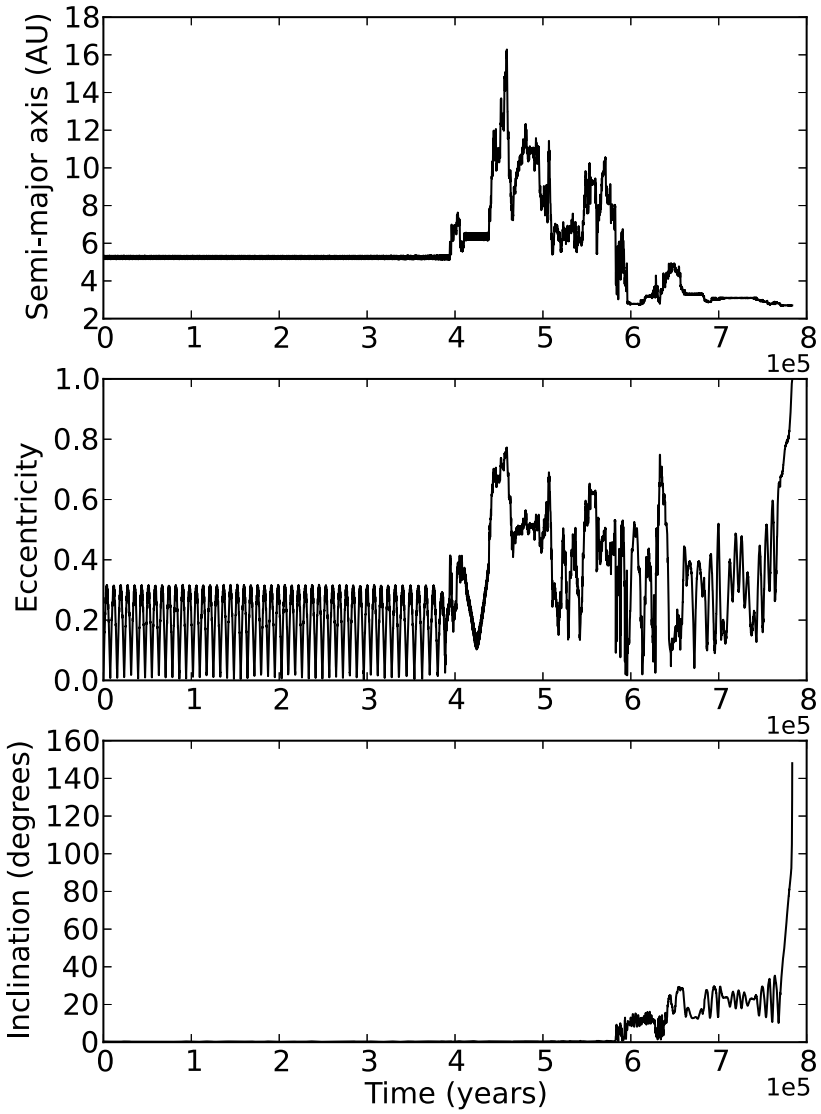

Figure 2.2 Individual particle motion for an accreted TP starting at 5.3 AU with $e = 0$, showing periods of chaotic motion and apparent entrapment in MMRs. Also note the large increase in inclination before accretion occurred, which was common for accreted particles in the presence of the $e = 0.2$ planet.

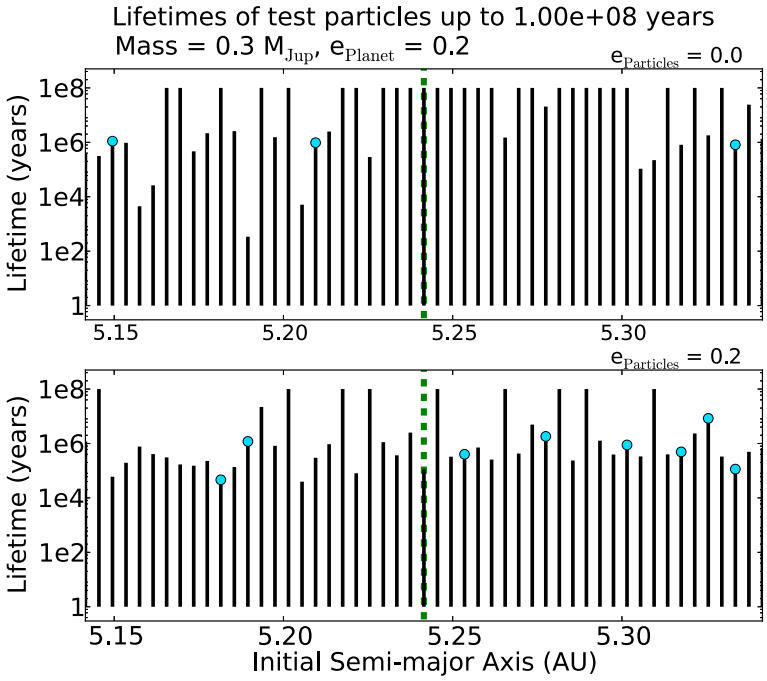

Figure 2.3 Lifetimes of the particles around the 2:3 MMR (dashed line), initially circular orbits on top and initially eccentric orbits ($e = 0.2$) on bottom. The circular particles are consistent with the results from the global simulations, while the eccentric particles were on average shorter-lived; this result supported our use of the initially-circular TPs in the other simulations.

accurately represented the material around a star that would exist at later times. Since our primary interest was the behavior of TPs at late times, this result reinforced our decision to use the particles on circular orbits for the large scale simulations.

2.4 Results for range of eccentricities and masses

To investigate the effect of planetary properties on the stability of surrounding bodies, we repeated the previous simulation for each combination of four planetary masses and five orbital eccentricities. We chose the mass values 0.03, 0.3, 1.0, and 4.0 M_{Jup} and the eccentricities 0.02, 0.2, 0.4, 0.6, 0.8 to probe the wide range in orbits of known exoplanets. Aside from eccentricity and mass, all planets started with the same initial conditions in all simulations, such as mean anomaly and argument of periapse. The SMA remained 4 AU for

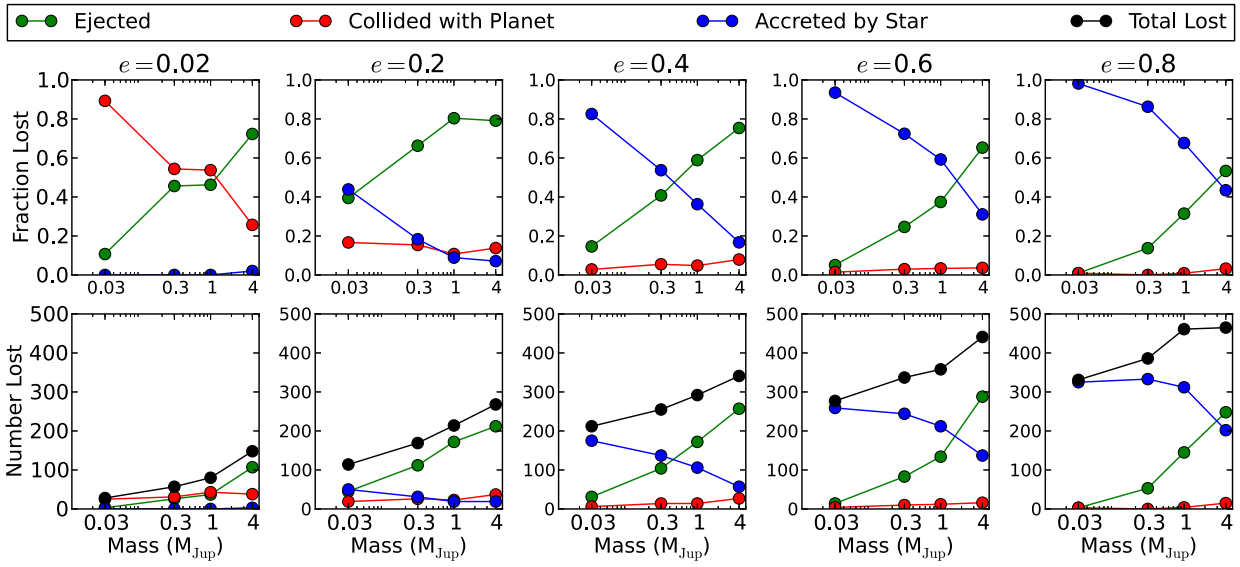

Figure 2.4 (top) Fraction of unstable TPs lost by each mechanism as a function of planetary mass, $N_{mechanism}/N_{Lost}$, for each planetary eccentricity over 10^8 years. In all cases with $e \geq 0.2$ the accretion fraction is a monotonically decreasing function of the mass. (bottom) Total number of particles lost by each mechanism. Despite increasing the amounts of unstable particles, increasing planetary mass resulted in fewer accreted particles.

all simulations as well, as probing a third dimension of parameter space would have been too computationally expensive.

2.4.1 Mass Effects

Our simulations showed that the total number of particles accreted by the star decreased with increasing planetary mass for all but the most eccentric planets (Figure 2.4, bottom, blue lines). Two factors contributed to this weak dependence: the size of the unstable region and the fraction of unstable particles accreted by the star. We found that while a larger planetary mass corresponded to a larger ECZ and a higher total number of unstable particles (black lines), it dramatically reduced the fraction accreted (Figure 2.4, top, blue lines). This reduced fraction more than offset the increased ECZ size, reducing the total number of particles accreted. The physical cause of this relationship is the strength of gravitational interactions: while the ≥ 1 M_{Jup} planets rapidly ejected most particles, smaller planets repeatedly interacted more weakly with the TPs and allowed them to slowly diffuse inward

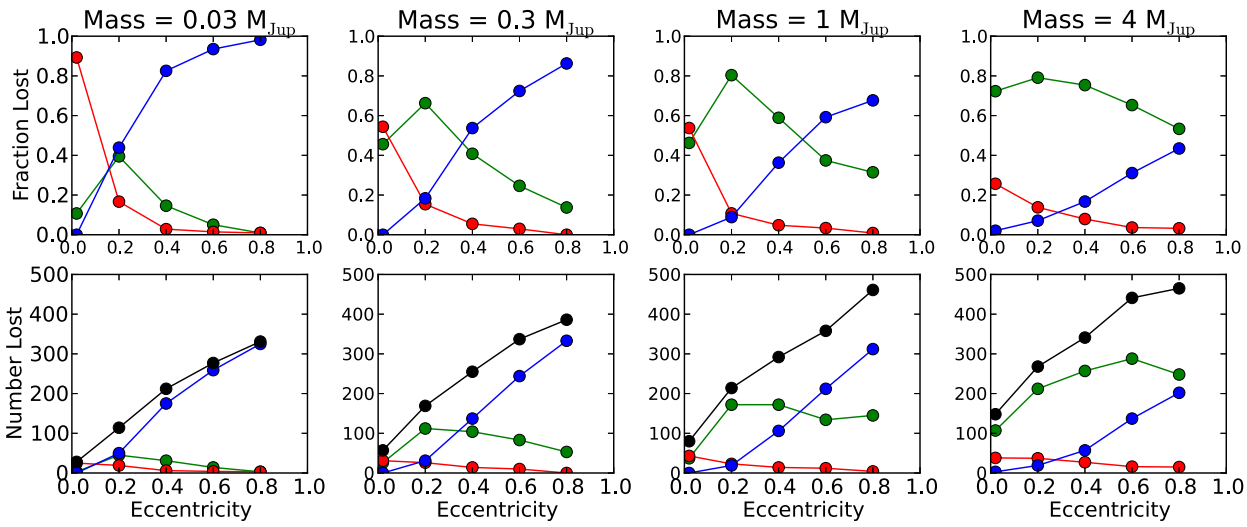

Figure 2.5 (top) Fraction of unstable TPs lost by each mechanism as a function of planetary eccentricity, for each planetary mass over 10^8 years. The dramatic and monotonic increase in accretion fraction with eccentricity is clear over all masses. (bottom) Total number of particles lost by each mechanism. Due to the growth of the ECZ, the increase with eccentricity is even greater.

and be accreted by the star.

In addition to changing the fraction of TPs accreted and ejected, planetary mass also affected the time-scale for instability to set in. Physically, more-massive planets are more capable of removing small bodies after a single scattering event, while smaller planets depend on the cumulative effect of multiple scatterings. As a result, the TPs in simulations with massive planets had shorter lifetimes than those in simulations with small planets. Figure 2.6 illustrates this effect with the lifetimes of TPs perturbed by the most massive planet (4 M_{Jup}) and a lower mass planet (0.3 M_{Jup}); Section 2.6.2.2 examines the characteristic lifetimes of particles in greater detail.

2.4.2 Eccentricity Effects

The planetary eccentricity had an equally powerful effect on the TPs. As it increased the periapse and apoapse of the planet shrank and grew, respectively, which widened the region around the star that the planet probed and expanded the ECZ. As a result, the planet caused

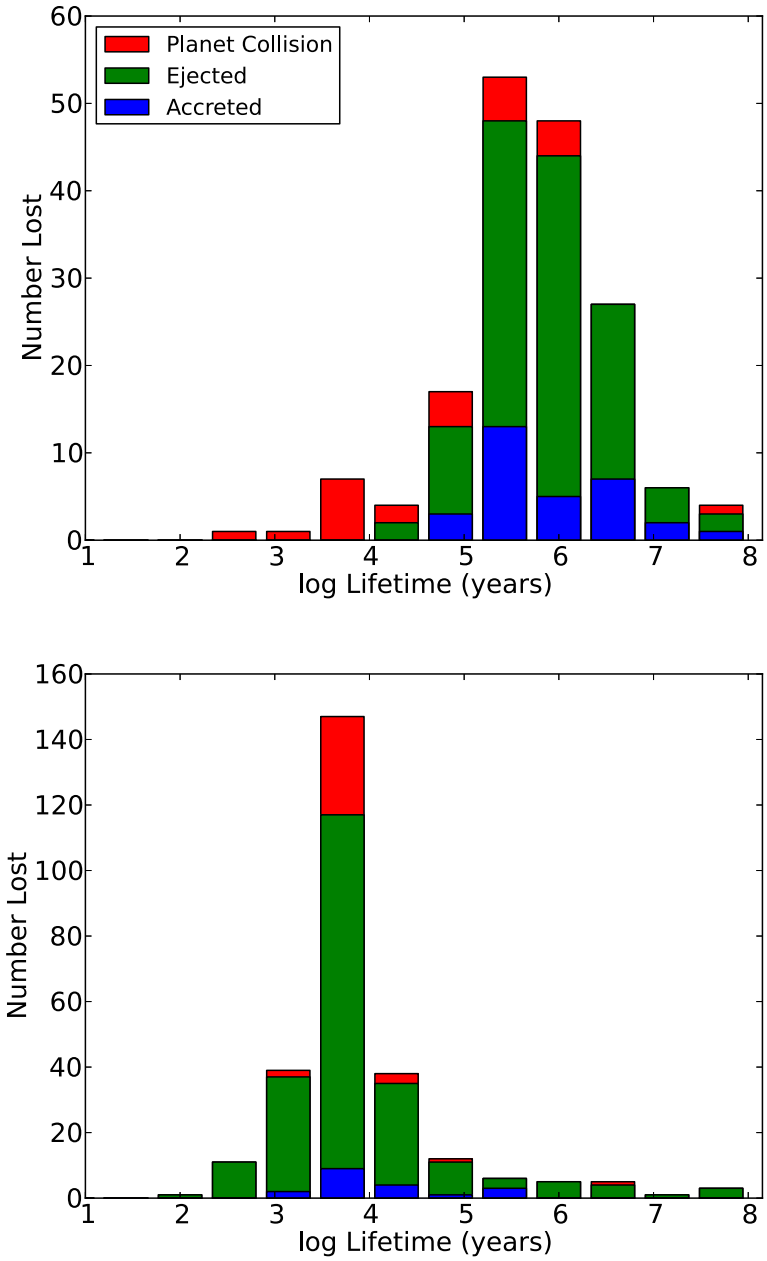

Figure 2.6 A comparison of the lifetimes for TPs lost in a system with a lower mass planet (0.3 M_{Jup}, top) and a massive planet (4 M_{Jup}, bottom), both with planetary eccentricity $e = 0.2$. The smaller planet resulted in longer lifetimes for unstable TPs as well as a larger fraction lost via accretion (blue bars).

a larger number of TPs to be destabilized and accreted (Figure 2.5, bottom, black lines). We also found that the eccentricity affected the fraction of TPs accreted, in fact more strongly than the planetary mass (Figure 2.5, top, blue lines). Physically, eccentric planets drive the forced eccentricity of particles up to higher values, while simultaneously having more and wider MMRs that can increase the eccentricity of the particles in them. Higher eccentricity causes a higher accretion probability. Finally, increasing planetary eccentricity resulted in the stellar accretion rate peaking earlier, as characterized by the mean accretion time in log space. We discuss this effect in greater detail and with respect to WD accretion in Section 2.6.

In the nearly-circular ($e = 0.02$) runs, planet-TP collisions dominated the loss mechanism, particularly at low mass. We were not hugely surprised by this behavior, as few TPs had eccentricities pumped to values large enough to eject or accrete. In these simulations most particles maintained a nearly constant Tisserand parameter, defined as

$$T = \frac{1}{a/a_p} + 2\sqrt{\frac{a}{a_p}(1-e^2)}\cos I \tag{2.4}$$

Here a and a_p are the SMAs of the particle and planet, respectively, while e and I are the particle eccentricity and inclination relative to the planetary orbit (Murray & Dermott, 2000). For small inclinations, an increase in eccentricity requires the SMA to increase as well. The Tisserand parameter determines the region of parameter space a particle can explore in the presence of a planet with zero eccentricity, including a minimum periapse.

As described in Bonsor & Wyatt (2012), for an accretion distance of 0.005 AU and an ejection distance of 100 AU only particles with $T < 2.1$ or $T < 2.85$ can be accreted or ejected, respectively. With the initial conditions $e = 0$ and $\cos I \approx 1$, all TPs started out with $T > 3$ and were incapable of close approach with the central star. The small eccentricity of 0.02 was enough, however, for particles to deviate slightly from a constant Tisserand parameter and be ejected. Ejections were most common in simulations with the more-massive planets, which were capable of ejecting particles even when on circular orbits (Bonsor & Wyatt, 2012). For planetary eccentricities larger than 0.02, the Tisserand parameter was not a

constant of motion (due to being derived from the restricted 3-body problem, where the planet is on a circular orbit). As a result, particle eccentricity was frequently increased with no corresponding growth in SMA.

2.4.3 ECZ width

In the case of a planet on a circular orbit, the interior and exterior edges of the CZ should be equal and scale simply with $\mu^{2/7}$ as described in Section 2.2.1. In our simulations we found that both mass and eccentricity served to increase the size of the ECZ, as shown by the points in Figure 2.7. Additionally, we found that the influence of planetary eccentricity served to produce interior and exterior edges at markedly different distances from the planet. To fit the eccentricity-ECZ effect we needed a model with three properties: showed edge asymmetry; increased with planetary eccentricity; and reduced to $\varepsilon_{\rm chaos} = 1.5\mu^{2/7}$ for $e_{\rm p} = 0$.

From a physical standpoint, a particle can be removed from the system when it crosses the path of the planet. Particles within the CZ in the zero-eccentricity case are simply those that undergo chaotic motion, and can therefore enter the path of the planet. For a given planet eccentricity and particle eccentricity, orbital crossing occurs at

$$a_{\rm in} = a_{\rm p}(1 - e_{\rm p})/(1 + e'_{\rm in}) \tag{2.5}$$

$$a_{\rm out} = a_{\rm p}(1 + e_{\rm p})/(1 + e'_{\rm out}) \tag{2.6}$$

where $a_{\rm in}$ ($a_{\rm out}$) is the inner (outer) edge of the ECZ, and $e'_{\rm in}$ ($e'_{\rm out}$) is the characteristic eccentricity leading to instability for the inner (outer) region. In this case,

$$\varepsilon_{\rm in} = \frac{e_{\rm p} + e'_{\rm in}}{1 + e'_{\rm in}}, \qquad\qquad \varepsilon_{\rm out} = \frac{e_{\rm p} + e'_{\rm out}}{1 - e'_{\rm out}} \tag{2.7}$$

To determine $e'_{\rm out}$ and $e'_{\rm in}$, both edges were assumed to obey the condition $\varepsilon(e_{\rm p} = 0) = \varepsilon_{\rm cz} = 1.5\mu^{2/7}$, the size of the CZ as determined by Duncan et al. (1989) for a planet on a

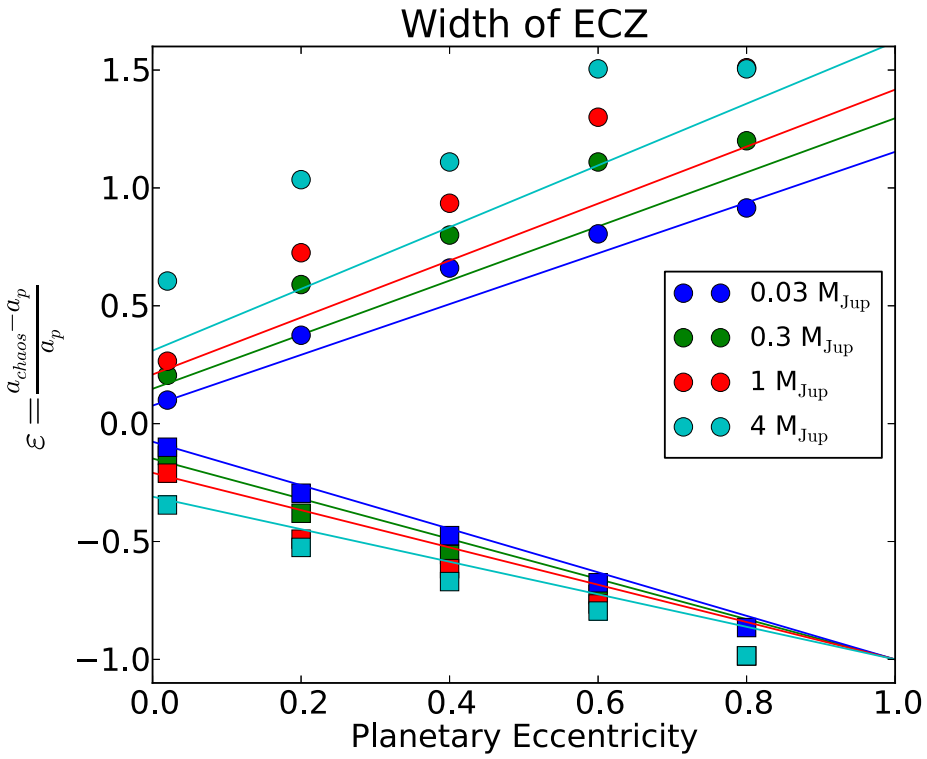

Figure 2.7 Scaled distance to the interior (squares) and exterior (circles) edges of the ECZ, as a function of eccentricity and planetary mass. The lines represent our interior and exterior model fits: $\varepsilon_{\rm in} = e_{\rm p}(1 - \varepsilon_{\rm cz}) + \varepsilon_{\rm cz}$ and $\varepsilon_{\rm out} = e_{\rm p}(1 + \varepsilon_{\rm cz}) + \varepsilon_{\rm cz}$.

circular orbit. Substituting for $e'_{\rm out}$ and $e'_{\rm in}$, the edges of the ECZ are defined by

$$\varepsilon_{\rm in} = e_{\rm p}(1 - \varepsilon_{\rm cz}) + \varepsilon_{\rm cz}, \qquad \varepsilon_{\rm out} = e_{\rm p}(1 + \varepsilon_{\rm cz}) + \varepsilon_{\rm cz} \tag{2.8}$$

as shown by the lines in Figure 2.7. While this function does not match our results perfectly, it does exhibit the asymmetry and expansion with eccentricity found in our simulation results, and does so with physical motivation. Finally, this model does not explicitly include the increase in resonance width with eccentricity and resulting change in resonance overlap, so it is unsurprising to see deviations from the fit.

2.4.4 Mean motion resonances

As described in Section 2.3.3, though many TPs that started in the vicinity of an MMR behaved similarly to the adjacent regions, some were stable inside of the ECZ (islands) and others were unstable outside of the ECZ (holes). Many of these holes became islands as the eccentricity of the planet increased and the MMR went from outside the ECZ to inside of it. In the case of 1 M_{Jup}, the 1:2 resonance at 6.4 AU changed from nearly the only unstable location outside of the ECZ at $e = 0.02$ to the only region of instability inside the ECZ at $e = 0.4$ (Figure 2.8). As a result, these holes were more rare in the higher-eccentricity simulations, due to the fact that the nearly all first-order MMRs were contained within the ECZ. Even so, they played an important role in delivering material to the star for some planets. In the case of $e = 0.2$ and the largest masses, 4 M_{Jup} and 1 M_{Jup}, the 3:1 resonance had a much higher fraction of TPs accreted by the star. In the 4 M_{Jup} case, 56 per cent of unstable TPs near the MMR were accreted, significantly larger than the accreted fraction of all unstable particle interior to the planet, 13 per cent.

We also found that the 1:1 resonance frequently retained TPs through the end of the simulation, for planets of eccentricity of 0.02 and 0.2. Most of these particles were on stable Trojan orbits. The mass of the planet determined the limiting eccentricity for Trojans. While the smallest planet (0.03 M_{Jup}) had Trojans when the eccentricity was up to and including 0.4, the planets with mass 0.3 M_{Jup} and 1 M_{Jup} only saw Trojans for $e = 0.2$ and 0.02. The most massive planet, 4 M_{Jup}, only had Trojans at the lowest eccentricity.

Finally, we again ran simulations with TP eccentricity matching planetary eccentricity. These simulations, while generally less stable than those with circular TPs, exhibited the same dependencies on planetary eccentricity and mass as those with TPs on circular orbits in all cases. We therefore believe these relationships do not depend strongly on particle eccentricity, though they may depend on particle inclination or longitude of periapse.

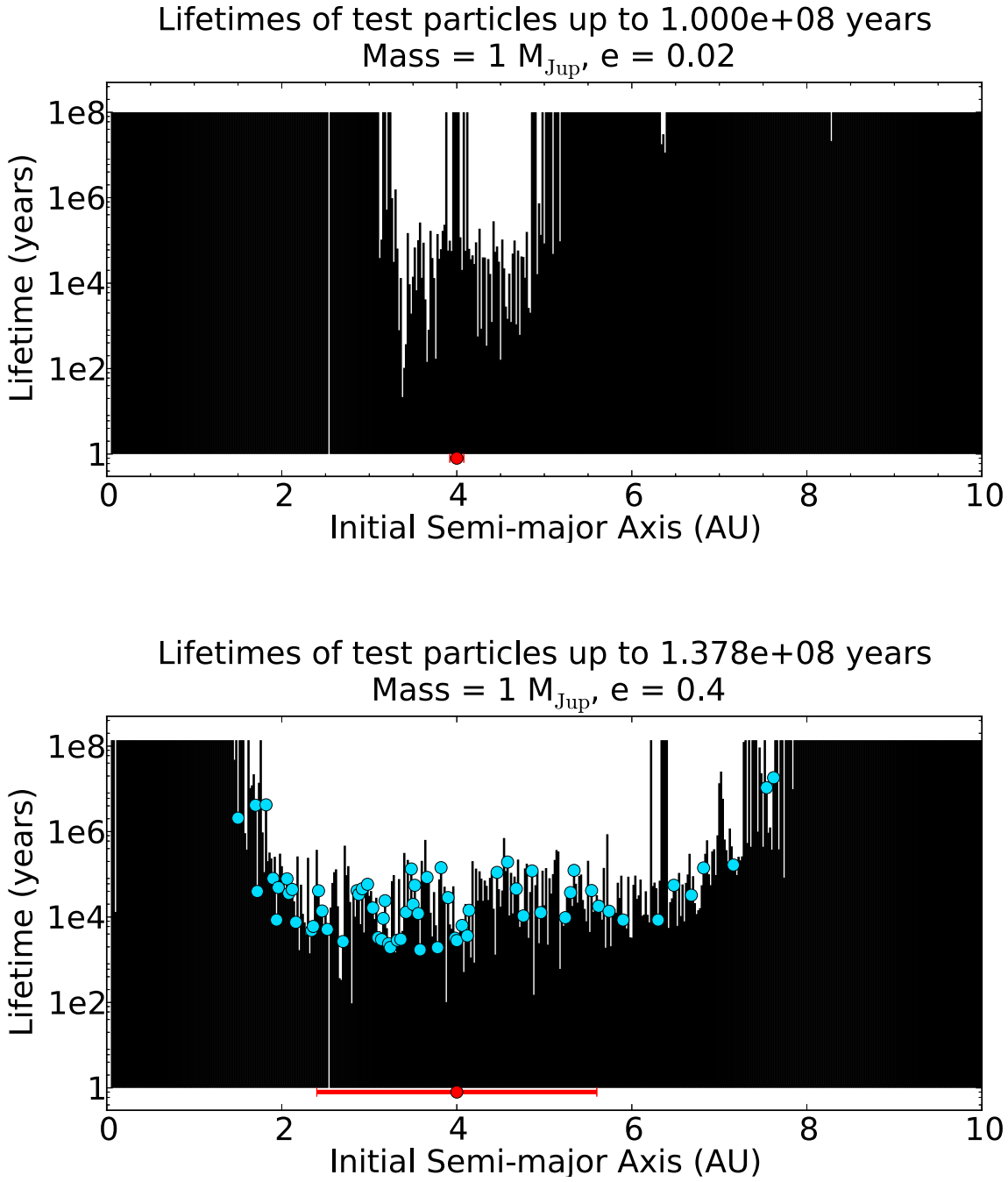

Figure 2.8 Lifetimes of TPs for a 1 M_{Jup} planet for planetary eccentricity $e = 0.02$ (top) and $e = 0.4$ (bottom). Note the change in the stability of the 1:2 MMR at 6.35 AU: in the low eccentricity case particles in the MMR are short-lived and unstable, while in the case of high eccentricity planet the MMR acts as a safe haven in a region of instability.

2.4.5 Comparison with previous work

Other research has also found similar trends with respect to planetary mass, such as Bonsor et al. (2011). In both cases, larger planets produced shorter TP lifetimes, higher ejection fractions, and reduced fractions either in the inner system (for Bonsor et al. (2011)) or accreted by the star (our result). While the total belt size differed in each case, we obtained consistent results for the total number of particles accreted as a function of planetary mass: where Bonsor et al. (2011) saw a weak decrease in the total mass scattered to the inner system as the mass of the planet increased, we saw the analogous result of fewer TPs accreted as the planet mass increased (at non-zero eccentricities).

Conversely, our results deviate from those of Quillen & Faber (2006), who found that the size of the CZ is independent of planetary eccentricity up to values of 0.3 regardless of planetary mass. By running our simulations with the TP initial conditions changed to those of the prior authors (coplanar particles given the predicted forced eccentricity and planetary longitude of periapse at their initial SMA), we matched their results and thus identified the different starting conditions as the source of discrepancy. While our TPs began with random longitude of periapse, Quillen & Faber (2006) used the expected forced eccentricity at that location along with the same longitude of periapse as the planet. Given that our simulations behaved similar for TPs with both planetary eccentricity and zero eccentricity, the difference is likely the longitude of periapse in conjunction with the forced eccentricity, which can prevent close encounters. Additionally, coplanarity prevents particles from reaching inclined orbits, which often occurred for the unstable particles in our simulations.

We also found that even with the changed initial conditions, planetary eccentricity larger than 0.2 still increased the size of the ECZ, albeit in a manner different from Figure 2.7. While the external edge remained close to the value expected from Equation 2.3, the internal edge changed dramatically, resulting in a much larger ECZ (Figure 2.9). This effect was only noticeable in the larger eccentricities, which were not investigated in Quillen & Faber (2006). Additionally, the effect of eccentricity on the number and fraction of accreted particles, as in Figure 2.5, remained. The effect of planetary mass on accretion fraction remained as well,

but was markedly weaker. As a result, the number of accreted particles was affected more strongly by the wider ECZ for massive planets, and increased with larger planetary mass. These simulations, along with the results described in Section 2.4.3, appear to indicate that the initial conditions of the particles play an important role in the some aspects of the system (such as size of ECZ), while other aspects are less affected (like the eccentricity-accretion relation). Therefore the importance of planetary eccentricity on WD accretion cannot be ignored.

2.5 Stellar Evolution

Until this point we have examined the stability of TPs in planetary systems around only an unevolved MS star. However, to estimate the WD accretion rate we also need to account for the reaction of the planetary system to the mass loss that occurs during post-MS evolution. Research shows that stellar evolution can change the stability of some orbits in the system due to the large amount of mass lost during the asymptotic giant branch and to a lesser extent the red giant branch (Mustill et al., 2014; Veras et al., 2013). From a purely gravitational standpoint, the ECZ dependence on the planet-to-star mass ratio (Equation 2.3) indicates that the ECZ will widen, due to the decrease in stellar mass. Additionally, the mass dependence of the MMR widths causes them to grow as well, as was shown in Debes et al. (2012).

The final mass of a WD can be estimated according to the equation for the empirical initial-final mass relation from Wood (1992):

$$\mathrm{M_{WD}} = 0.49 \exp[0.095 \mathrm{M_{MS}}] \tag{2.9}$$

Here $\mathrm{M_{MS}}$ and $\mathrm{M_{WD}}$ are the initial (MS) mass and final (WD) mass, respectively, of the star in solar masses. For stars near a solar-mass star this equation gives a WD mass of 0.539 $\mathrm{M_\odot}$, which is consistent with more recent work on the relation including Weidemann (2000) and Kalirai et al. (2008).

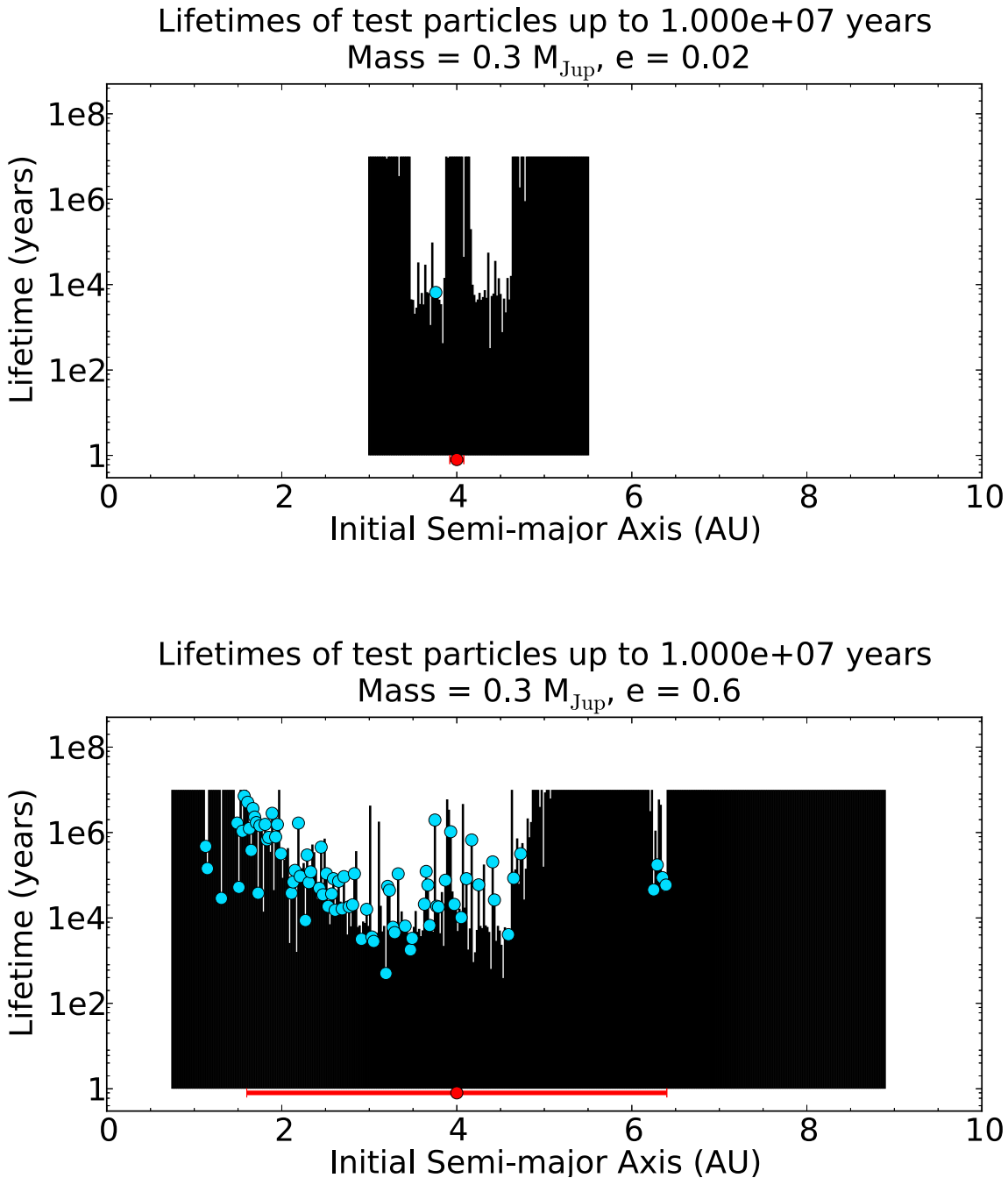

Figure 2.9 Particle lifetimes in the presence of a 0.3 M_{Jup} planet with eccentricity $e = 0.02$ (top) and $e = 0.6$ (bottom). In these simulations the TPs began on orbits with the forced eccentricity at their starting location and the same argument of periapse as the planet. In this case, the size of the ECZ changes, but the expansion is limited almost entirely to the region interior the planet.

Given adiabatic mass loss, conservation of angular momentum dictates the SMAs of orbiting planets will increase by an amount determined by the initial-to-final mass ratio (Debes & Sigurdsson, 2002):

$$a_f = a_0 \left(\frac{\mathrm{M_{MS}}}{\mathrm{M_{WD}}} \right) \tag{2.10}$$

For a body around a solar-mass star the orbit will expand by a factor of 1.86. A planet with an SMA of 4 AU will then reach a new orbit of 7.42 AU. Since this orbital expansion affects all bodies in the system equally (ignoring non-gravitational effects), the period ratios between them will remain the same and bodies already in MMR with a planet will remain so. However, the larger planet-to-star mass ratio results in larger widths for MMRs, which can result in new objects entering resonance. The change in central mass also affects the size of the ECZ. From Equation 2.3 we can predict the magnitude of this increase in the case of zero eccentricity:

$$\varepsilon_{\mathrm{WD}}/\varepsilon_{\mathrm{MS}} = (\mu_{\mathrm{WD}}/\mu_{\mathrm{MS}})^{2/7} = (\mathrm{M_{MS}}/\mathrm{M_{WD}})^{2/7} \tag{2.11}$$

For our star the mass loss should produce a widening of 19 per cent. However, we saw in Section 2.4.3 that eccentric planets do not follow this relation closely. Assuming the edges of the ECZ are actually defined by Equation 2.8, which more closely matches our MS simulations, the relative growth would drop with increasing planetary eccentricity. As the eccentricity increases, the contribution from the classic CZ ($\varepsilon_{\mathrm{cz}}$) to the size of the ECZ decreases and the orbital excursions of the planet dominate. The ratio in that case is given by

$$\varepsilon_{\mathrm{WD}}/\varepsilon_{\mathrm{MS}} = \frac{e_{\mathrm{p}}(1 \pm 1.5\mu_{\mathrm{WD}}^{2/7}) + 1.5\mu_{\mathrm{WD}}^{2/7}}{e_{\mathrm{p}}(1 \pm 1.5\mu_{\mathrm{MS}}^{2/7}) + 1.5\mu_{\mathrm{WD}}^{2/7}} \tag{2.12}$$

As a result, more-eccentric planets with ECZs following this relation will have a relatively smaller amount of expansion. However, the physical growth of the unstable region ($\varepsilon_{\mathrm{WD}} - \varepsilon_{\mathrm{MS}}$) will increase with planetary eccentricity for the exterior edge, and the greater fraction of TPs accreted in the presence of an eccentric planet still supports the latter as a better source of pollution.

2.5.1 Non-gravitational forces

Post-MS evolution can have further implications for the orbits of small bodies due to non-gravitational effects. Wind drag during the giant branches can hinder the ability of small bodies to move outward, causing them to move relative to the ECZ and MMRs of a planet (Dong et al., 2010; Jura, 2008). Furthermore, the luminosity of the star increases dramatically during the giant phases. This brightening can produce a non-negligible Yarkovsky force on some small bodies (Bottke et al., 2006), moving them inwards or outwards. Both of these effects result in rearrangement of previously stable particles, repopulating some unstable regions and resulting in a new source of WD pollution.

The wind resulting from stellar mass loss can strongly affect small bodies, particularly near the star. Dong et al. (2010) examined this effect on objects orbiting more massive stars (3–4 $M_\odot$) at greater distances (> 10 AU) than our simulations, and found that wind drag can change the final orbit of even moderately-sized bodies (1–10 km) as well as cause resonance capture for a range of initial conditions. Using our own parameters, we analytically estimated the effect of wind drag on bodies located at 7 AU around a 1 $M_\odot$ star. We found that at this distance 250-m diameter objects moved AU-scale distances, and even 10-km diameter objects showed significant changes to their final orbit: roughly 0.04 AU inwards compared to the adiabatic case. Assuming a number distribution inversely proportional to size and a disk spanning 7 to 9 AU, this wind drag results in approximately 1.5 per cent of the material entering the ECZ. While it depends on the width (due to larger objects moving less) and location of the disk, this order-of-magnitude calculation does indicate substantial amounts of mass can change location for large disks.

The Yarkovsky effect depends heavily on the physical properties of the small bodies, including size, shape, composition, and rotational state. However, by following prior research into the topic we estimated the change in SMA through this mechanism. According to Spitale & Greenberg (2001), 100-m objects around the Sun have $\mathrm{d}a/\mathrm{d}t \sim 0.1$ km yr^{-1} motion for most eccentricities. While changes to the spin states of the object reduce the long-term importance of the Yarkovsky effect during the MS (Farinella et al., 1998), the brief period

over which the giant branches last should result in few (if any) reorientations for objects 1 km in diameter or larger. Smaller objects will likely move rapidly, allowing for large changes in SMA even with reorientation.

If we assume this motion scales inversely with the size of the object, the SMA of a 10-km body will then change by 0.0037 to 0.18 km yr^{-1}, or 2.4×10^{-11} to 1.2×10^{-9} AU yr^{-1}, around an RGB star (average luminosity $\bar{L} \approx 180 L_{\odot}$), depending on the luminosity dependence of this effect: an asteroid with poor heat conduction will see the Yarkovsky effect increase linearly with the surface flux, but efficient heat conduction will reduce the temperature difference between the hot and cold faces and weaken the effect. We account for this uncertainty by considering a scaling of the strength of the effect with stellar luminosity (L) or with stellar effective temperature ($L^{0.25}$). Over the duration of the RGB branch, 80 Myr, the body would move a distance $\Delta a \approx$0.002–0.1 AU. While this estimate ignores the impact of mass loss (due to the complicated dependence on SMA), it nevertheless illustrates the power of the Yarkovsky effect during periods of high luminosity.

Both of these effects also impact the eccentricity of surviving bodies. The Yarkovsky effect is capable of pumping or damping it depending on the spin orientation of the body (Spitale & Greenberg, 2002), while wind drag exclusively causes damping (Dong et al., 2010). The latter affects eccentricity more strongly, causing the orbits of small bodies to become more circular during stellar evolution. Meanwhile, neither wind drag nor the Yarkovsky effect excite inclination (the latter as a result of orbital precession caused by the planet (Bottke et al., 2000)), leaving low-inclination bodies particles to continue on roughly coplanar orbits.

Finally, it is important to note that the location and composition of the planet are crucial for its survival during stellar evolution. Planets near the star will be engulfed, while those just outside the envelope can still spiral in due to tidal effects (Rasio et al., 1996). For massive planets farther out, the high flux received during and after the giant phases might result in planetary evaporation and mass loss (Villaver & Livio, 2007).

2.6 White dwarf simulations

To determine how stellar evolution affects the stability of orbiting TPs, we ran two sets of simulations. The first used the final orbital elements of the planet and surviving TPs from the MS simulations translated outward; the second used a new set of particles in the region around the WD.

2.6.1 *In situ* evolved simulations

For the simulations that left particles in place during evolution, we first came up with a model for the evolution itself. We used a simple transition in which we reduced the mass of the star linearly over 2700 years, while leaving the planet and TPs *in situ* with the orbital elements they had at the end of the MS simulations. We note that there are myriad ways to model mass loss in post-MS stars, including various durations and time dependencies. Additionally, a more accurate and complicated treatment would include the non-gravitational forces described in Section 2.5.1. However, this evolution is not our focus and as such we did not consider other, more-complicated models. Furthermore, the orbital expansion does not depend on the time-scale for mass loss, as long as the latter is much longer than the orbital periods (the adiabatic approximation).

We implemented the mass loss in our code again using the BS integrator, with the stellar mass reduced by 5.61×10^{-6} $M_\odot$ after each 12-day time-step. We chose the duration of the mass loss to minimize computation time while still being adiabatic, which is necessary for Equation 2.10 to hold. In all the WD simulations the ejection and accretion distances remained the same at 100 AU and 0.05 AU, respectively. While the radius of a WD is dramatically smaller than that of a MS star, the Roche limit is approximately the same.

We also mention that while our MS simulations did not reach the actual MS lifetime of a 1 $M_\odot$ star ($\sim 10^{10}$ years), the vast majority of unstable particles were removed by 10^8 years (as illustrated by the number lost at late times in Figure 2.6). Using the change in loss rates over time, we estimate approximately 30 per cent of the unstable particles in these evolved systems were unstable in the MS system at times beyond 5×10^7 years. As such, we were

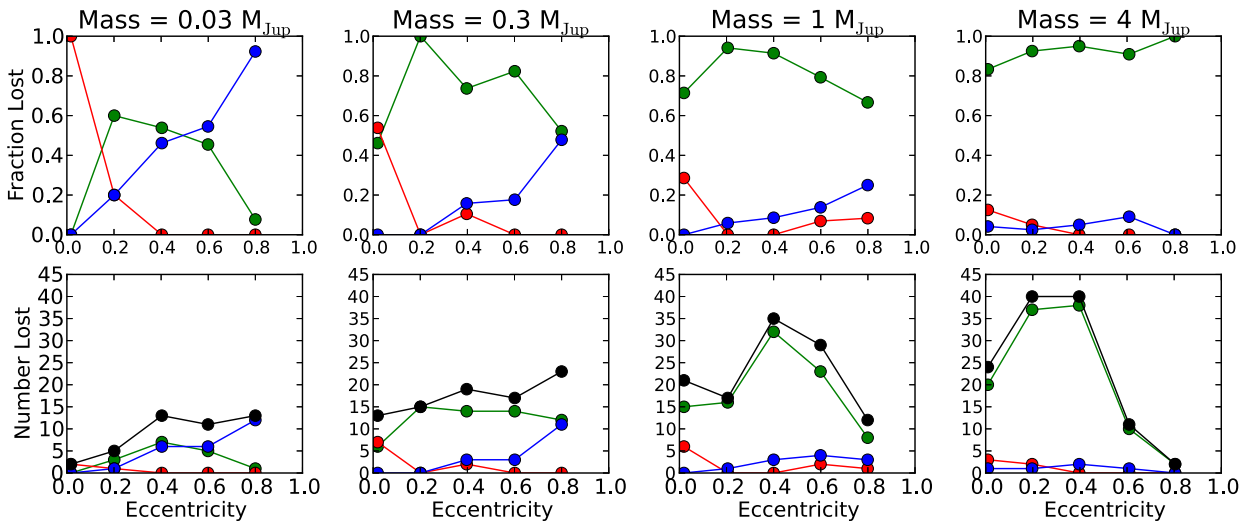

Figure 2.10 Same plots as Figure 2.5, fraction lost (top) and number lost (bottom) for each mechanism as a function of eccentricity, but for our evolved simulations. The eccentricity dependence still remains in most cases, but disappears in the highest-mass, highest-eccentricity cases due to the ECZ exceeding the bounds of the simulation.

able to approximately remove this contribution to the WD simulations and determine the instabilities introduced by mass loss. The 0.03 M_{Jup} simulations were an exception to this rule, due to longer particle lifetimes, and are addressed in Section 2.6.1.2.

2.6.1.1 Results

These simulations followed the same eccentricity–fraction-accreted relationship: increasing planetary eccentricity resulted in a larger percentage of unstable particles accreted by the star in all cases (Figure 2.10). Unlike the MS simulations, however, this relationship did not correspond to a larger number of TPs accreted in every case. For the 1 and 4 $_{Jup}$ planets at eccentricities of 0.6 and 0.8, the ECZ spanned nearly the entire 10 AU disk in the MS, leading to fewer unstable particles in these simulations (Figure 2.10, bottom right panels). Had the initial disk extended beyond 10 AU initially, it is likely that the more-eccentric planets would have resulted in more unstable particles, similarly to planets with mass 0.03 and 0.3 M_{Jup} and as they did in the MS case.

For the simulations with ECZs that did not span the entire disk during the MS, the

total number of unstable particles varied more strongly with planetary mass than during the MS. As described in Section 2.5, the ECZ and MMRs widen as a result of mass loss, which produces newly unstable particles. Both the fractional growth in the ECZ (Equation 2.11) and absolute change in size depend on planetary mass. Therefore it is not surprising to see this stronger mass dependence on total number of unstable particles. We observed the ECZ expansion in the results of some simulations, but did not see it consistently between masses or eccentricities as a result of small number statistics, particularly in the higher eccentricity cases where few TPs survived from the MS.

2.6.1.2 Extended simulation

Due to the late onset of instability in the MS 0.03 M_{Jup} case, we expected a significant fraction of unstable TPs to be unstable on time-scales greater than 10^8 years, resulting in contamination to the evolved simulations. To combat this issue and the low number of TPs noted above, we repeated the 0.03 M_{Jup}, $e = 0.4$ simulation with quintuple the TP resolution (reducing the separation between TPs to 0.004 AU) and for a longer duration: 2×10^8 years for the MS and 1×10^9 years for the WD phase. Long computation times prevented us from repeating this simulation for additional planetary masses and eccentricities. Such a high density of TPs remedied the issue of few survivors in the post-evolution simulation, allowing us to better test the potential of a single, ideal planet to pollute a WD without non-gravitational forces.

The MS simulation behaved identically to the same planet in Section 2.4, with the exception of better statistics and an increased duration. The lost particles peaked near 5×10^6 years, and accretion dominated the unstable particles while collisions with the planet occurred infrequently. The extra 100 Myr behaved similar to the prior 50 Myr, showing both accretion events and ejections at a much reduced rate from the peak. Extrapolating from the accretion rate as a function of time, we found that that only ~ 25 particles were expected to go unstable in the subsequent 1 Gyr, which allowed us to account for contamination in our next simulation. Finally, as the number of TPs were not a limiting factor in the prior

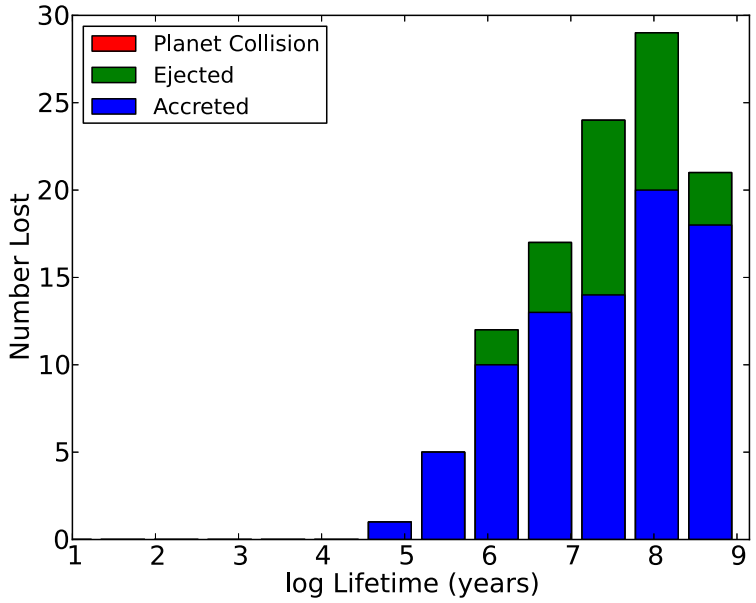

Figure 2.11 The lifetimes of unstable particles for the evolved system with 0.03 M_{Jup}, $e = 0.4$, illustrating the late onset of instability and the large fraction of accreted particles.

MS simulation, these results do not gain us much more insight.

The evolved simulation, however, differed significantly: the increased number of surviving particles and greater duration produced an obvious expansion of the ECZ (Figure 2.12). The ECZ expanded by 10 per cent, less than expected in the circular case but larger than expected from Equation 2.8, 3.1 per cent. This simulation also displayed the accretion and ejection peaking near 10^8 years, as shown in Figure 2.11, with the 20-fold increase from MS peak due to both fewer particles unstable on short time-scales (cleared out in the MS) and the larger planetary SMA. Using the MS-simulation extrapolation, we found that that fewer than 25 per cent of lost particles were contaminants. Significant accretion continued to occur up to the end of the simulation, indicating that a planetary system like this, given certain disk properties, could account for the pollution observed in some polluted WDs. We discuss the feasibility of this mechanism in further detail in Section 2.7.1.

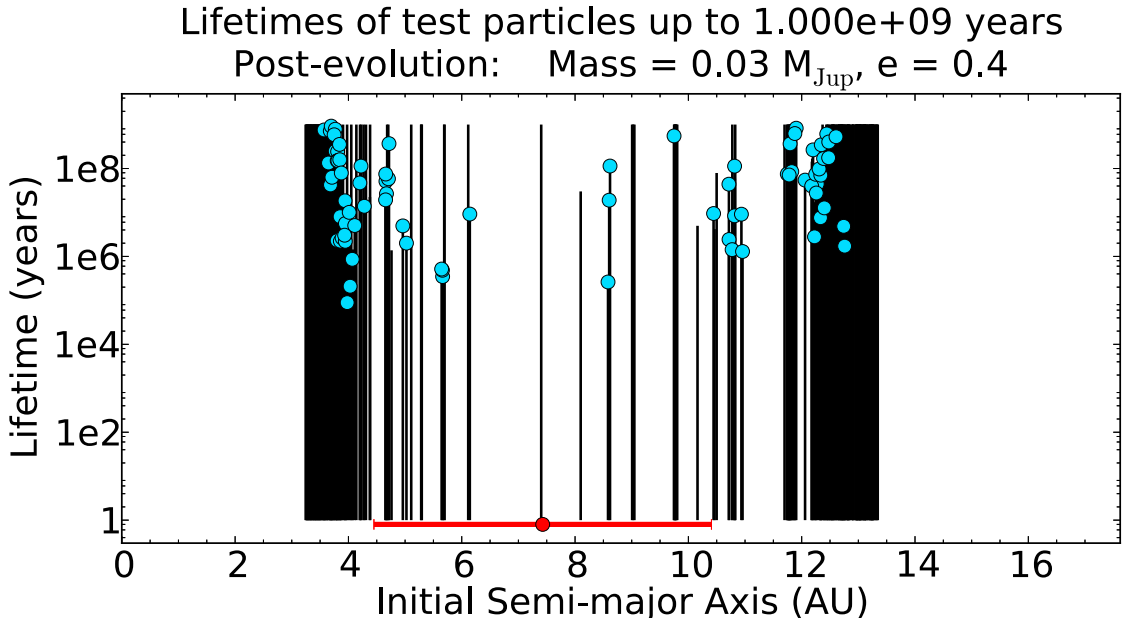

Figure 2.12 Lifetimes of TPs for the evolved extended simulation (0.03 M_{Jup} and $e = 0.4$, initial spacing of 0.004 AU). The expansion of the ECZ due to stellar mass loss is apparent as is the large fraction of accreted particles.

2.6.2 Repopulated simulations

The second set of WD simulations represented complete repopulation by non-gravitation forces, and we populated these with a completely new set of TPs spaced 0.03 AU apart[1] between 0.06 AU and 18.6 AU. For consistency with the MS simulations and the effects described in Section 2.5.1, all particles started at random points on circular orbits. These simulations were similar to the original MS simulations, but with all bodies at greater distances about a reduced stellar mass. As a result, they represented the change in stability of locations within the system, as opposed to the change in stability of individual particles (which showed some small amounts of motion within stable regions during the MS). While complete repopulation of all unstable regions in a system is unrealistic, as much as 1.5 per cent of the mass in a narrow annulus can be expected to move into them during stellar evolution via non-gravitational forces (as described in Section 2.5.1). Alternatively, planetary systems that are near instability would result in a planet ending up on a new orbit after

[1]The spacing was increased from 0.02 AU to allow us to probe the larger spatial scales with similar computation time.

a scattering; the results of Veras et al. (2013) indicate that such scatterings are possible around WDs at late times, and can result in highly-eccentric orbits.

2.6.2.1 Results

As illustrated in Figure 2.13, these simulations behaved similarly to those of Section 2.4, . Increased eccentricity again dramatically increased both the total number of TPs that went unstable as well as the fraction that were accreted by the star, and lower masses again showed equivalent or greater numbers of accreted particles. We noted certain differences between the two sets of simulations, however. Due to the increased distance from the star and the reduced stellar mass, TPs were more weakly bound and a greater fraction ejected in the WD setup. This change can be seen in a comparison of Figures 2.5 and 2.13, and correspondingly led to a smaller accretion fraction.

Compared to the extended simulation, the repopulated 0.03 M_{Jup}, $e = 0.4$ simulation peaked earlier and had a smaller unstable fraction at late times due to the large contribution from TPs in repopulated regions, which rapidly went unstable. Even so, both the repopulated and the extended models showed agreement in the fraction of particles accreted and ejected, allowing us to extrapolate accretion rates to other masses and eccentricities from our single extended simulation. Additionally, the location of the oldest particles remained the same: the edge of the ECZ.

As a result of stellar mass loss and orbital expansion, the width of the ECZ should increase according to Equation 2.8. We observed this expansion in our repopulated simulations, illustrated in Figure 2.14 for a near-circular planet. The sizes of the ECZ were similar to that shown in Figure 2.7, and are not plotted. As described in Section 2.5, the relative increase in the size of the ECZ should decrease with eccentricity when it obeys Equation 2.8. We found that to be generally the case for the interior edge of the ECZ, which followed Equation 2.8 closely in both the MS and the WD cases. Figure 2.15 illustrates this effect, as larger eccentricities generally have ratios closer to one. Conversely, the exterior edge deviated more so from Equation 2.8 in both cases, and thus displayed greater scatter about

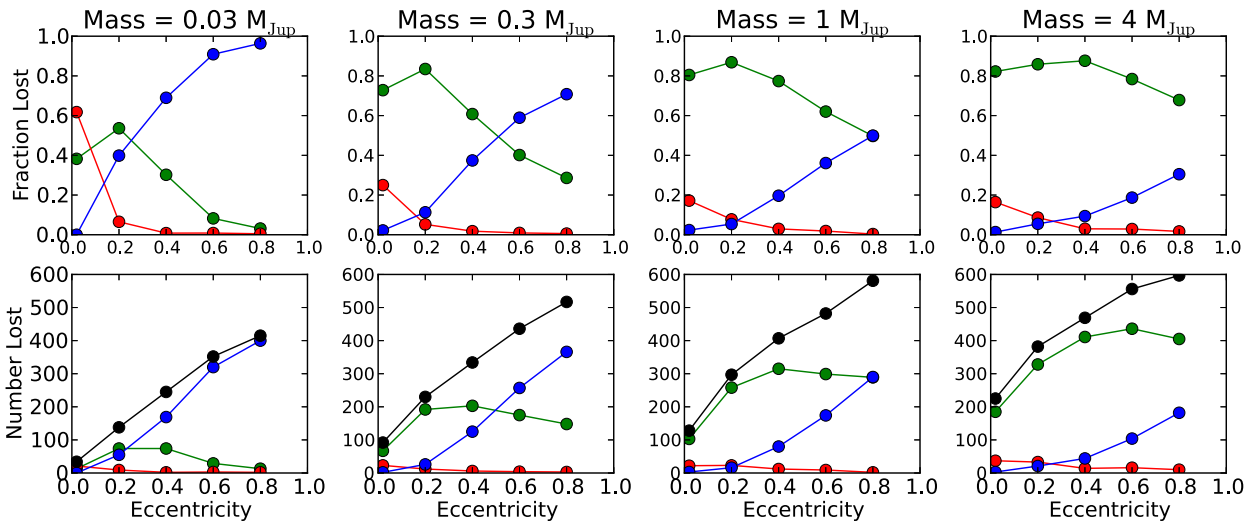

Figure 2.13 Same plots as Figure 2.5, fraction lost (top) and number lost (bottom) for each mechanism as a function of eccentricity, but for our repopulated WD simulations. The same characteristics as in the MS simulations are present (e.g. increase in accretion fraction with planetary eccentricity) but the ejection fraction is systematically higher in all cases.

the expansion relation. Additionally, the full size of the ECZ may be larger than plotted, particularly for the low mass simulations, as our extended simulation showed further particles becoming unstable at the ECZ edge after 10^8 years.

Similar to the ECZ, the widths of MMRs should grow with mass loss and thus can be a valuable source of unstable particles (Debes et al., 2012). Our results showed this widening of MMRs in some of our simulations, particularly in the case of MMRs interior to massive planets. The 3:1 resonance in our $e = 0.2$, 4 M_{Jup} simulation grew from 0.064 AU in the MS case to 0.141 AU in the WD case. While the physical width was expected to increase due to the larger spacing between bodies, that effect would only result in a factor of $M_{MS}/M_{WD} = 1.85$, not 2.2 as we saw. In both cases a large fraction of the unstable particles were accreted (9 out of 16 for MS, 9 out of 19 for WD), despite a low fraction (13 per cent for both) of interior TPs accreted overall. Despite starting with fewer TPs than Debes et al. (2012), these simulations support internal MMRs as another potential source of WD pollution. Given the results of our extended simulation in Section 2.6.1.2, multiple mechanisms may play a role in the pollution observed.

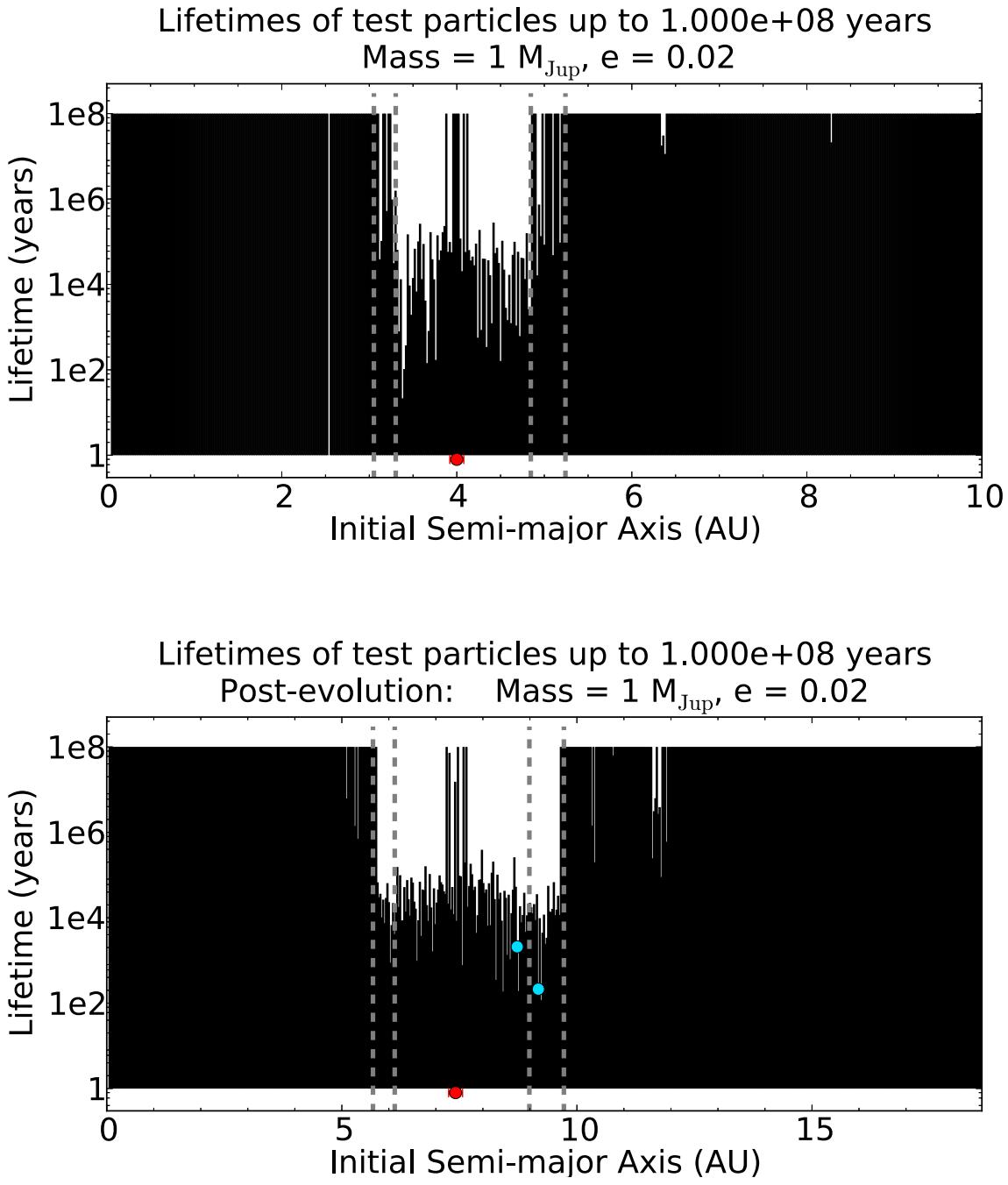

Figure 2.14 A comparison of the MS and WD simulations for a planet with M = 1 M_{Jup} and $e = 0.02$. Note the wider instability in the WD case, located between the 3:2 and 2:1 resonances and between the 1:2 and 2:3 resonances (grey dashed lines).

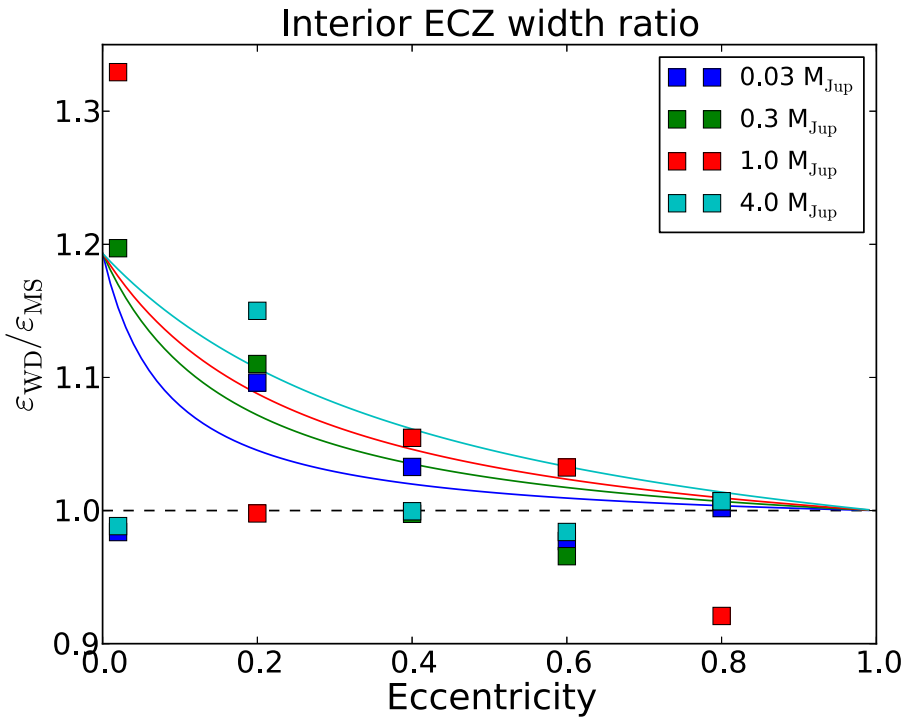

Figure 2.15 Ratio of WD ECZ size to MS ECZ size, for the interior edge, with lines indicating no change in size (black dashed) and a change characterized by Equation 2.8(colored solid). Despite the scatter, the trend of less expansion with greater eccentricity is clear.

2.6.2.2 Accretion at late times

While the relationship between planetary properties and the total number of particles accreted over all time is interesting, it has little bearing on WD pollution unless that accretion occurs at late times. The results from our WD simulations agreed with our findings in Sections 2.4.1 and 2.4.2 regarding particle lifetime: both higher masses and higher eccentricities lead to earlier peak times, as shown in Figure 2.16. Because of this shift in peak time, the maximum amount of accreted material at late times (above 10^6 and 10^7 years) did not always occur in the simulations with the largest eccentricity, as shown in Figure 2.1. Larger eccentricities increased the pollution at late times only up to a point, above which the pollution was reduced. These peak eccentricities depended on planetary mass: $e = 0.6$ in the case of 0.03 and 4 M_{Jup}, and $e = 0.8$ in the case of 0.3 and 1 M_{Jup}. Given such large peak eccentricities, we confirm our previous results: in the vast majority of cases, larger planetary eccentricities (and smaller masses) correspond to larger amounts of polluting material.

2.7 Discussion

These simulations clearly show that planetary mass and eccentricity play an important role in the ability of a planet to pollute the central star. Given the mass dependence of both the fraction and the total number of accreted TPs, it appears that planets do not need to be as massive as Jupiter to be a potential source of WD pollution, and such massive planets may in fact not be the prime candidates. The extended simulation of Section 2.6.1.2 supported the result that small planets deliver as much material or more than massive planets, and at later times, with a 0.03 M_{Jup} planet continuing to deliver material at Gyr time-scales. It would not be unusual for an exoplanet to have these properties: small planets now appear to be more common than large planets, both near the star (Batalha et al., 2013) and further away (Gould et al., 2006; Sumi et al., 2010). Furthermore, a wide range of eccentricities have been detected in exoplanet surveys (Butler et al., 2006), up to 0.4 for 0.03 M_{Jup} planets and above 0.8 for 4 M_{Jup} planets. The planetary mass which produces maximum accretion is still uncertain— the smallest of our planetary masses (0.03 M_{Jup}) produced the highest number of

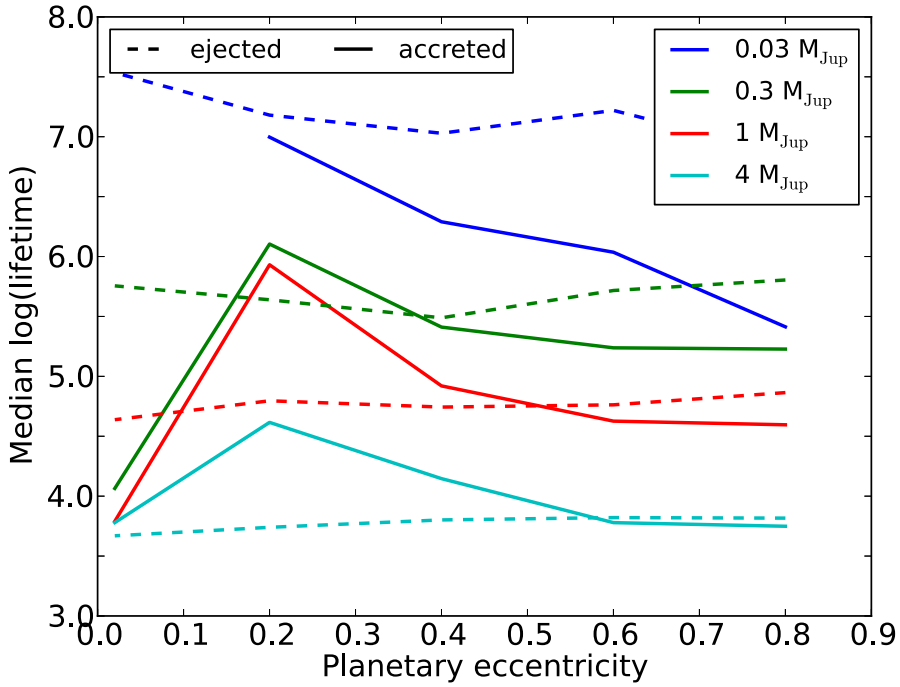

Figure 2.16 Median lifetime of ejected and accreted unstable particles in log space for each planetary mass as a function of eccentricity, for our repopulated WD simulations. Very few particles were accreted in all the $e = 0.02$ simulations (including zero for the 0.03 M_{Jup} case), which accounts for the strange behavior and missing point at that eccentricity. All of the planets show in a decrease in accreted-TP lifetime when the planetary eccentricity is increased above 0.2.

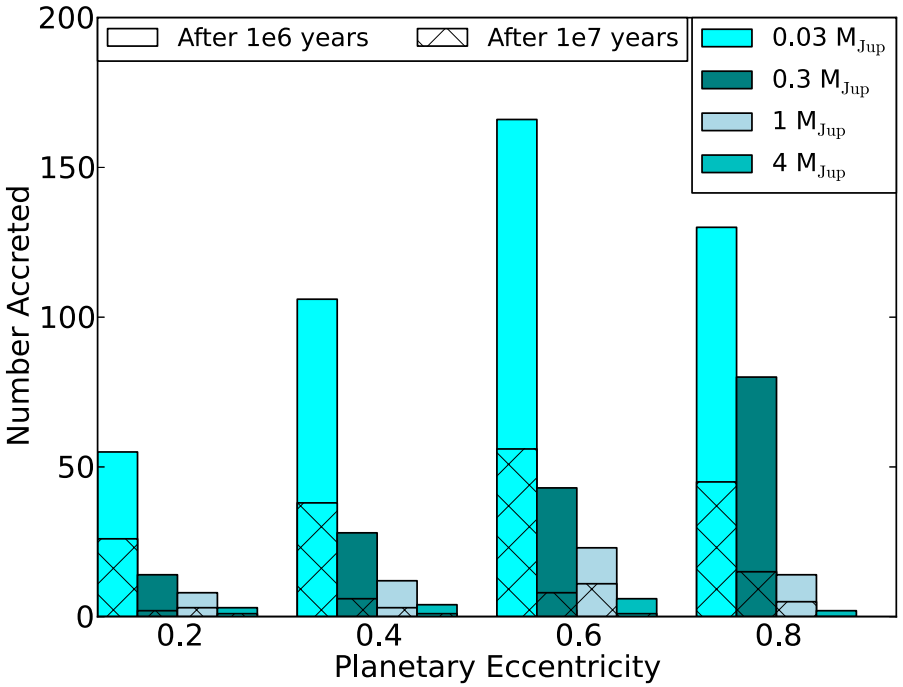

Figure 2.17 Number of particles accreted by the WD in the repopulated simulations after 10^6 and 10^7 years, as a function of mass and eccentricity ($e = 0.02$ not shown, as nearly no particles were accreted in that case). The accretion amounts clearly increase with eccentricity for both times through $e = 0.6$, across all masses, and decreases with mass across all eccentricities.

accretion events, but it is possible that even smaller masses would produce a higher number. However, it is not clear theoretically or observationally whether sub-Neptune-mass planets can form at several AU distances. Such simulations would also be more computationally expensive, and possibly violate the massless-TP assumption.

2.7.1 The WD disk mass from accretion rates

While our simulations did not reach the times corresponding to the oldest cooling ages of polluted WD ($> 10^9$ years, Farihi et al. (2010b)), our longest simulation did reach the time-scales of average polluted WDs (10^8–10^9 years). Determining which planetary properties best cause pollution in a star is only useful if such pollution can match observations, which is set by the disk mass required in our simulations. To determine that mass, we assumed a power law for the loss rate of particles:

$$\frac{\mathrm{d}N_{\mathrm{lost}}}{\mathrm{d}t} = -\frac{\mathrm{d}N_{\mathrm{rem}}}{\mathrm{d}t} = \frac{N_{\mathrm{rem}}^{\alpha}}{t_0} \tag{2.13}$$

Here α and t_0 are constants to be fit by our simulation results, and N_{rem} (N_{lost}) is the number of particles remaining (lost). Solving this equation for N_{rem} gives

$$N_{\mathrm{rem}} = \frac{N_0}{[1 + (\alpha - 1)N_0^{\alpha-1} t/t_0]^{\frac{1}{\alpha-1}}} = \frac{N_0}{[1 + t/t_*]^{\frac{1}{\alpha-1}}} \tag{2.14}$$

where N_0 is the initial number of unstable particles ($N_{\mathrm{rem}} = N_0 - N_{\mathrm{lost}}$), another constant to be fit, and

$$t_* = \frac{t_0}{(\alpha - 1)N_0^{\alpha-1}} \tag{2.15}$$

is the characteristic time scale for losing particles. The loss rate as a function of time is then

$$\frac{\mathrm{d}N_{\mathrm{lost}}}{\mathrm{d}t} = -\frac{\mathrm{d}N_{\mathrm{rem}}}{\mathrm{d}t} = \frac{N_0}{(\alpha - 1)t_*}(1 + t/t_*)^{\frac{-\alpha}{\alpha-1}} \tag{2.16}$$

We determined the values of α, t_*, and N_0 by performing a least-squares fit to the cumulative distribution of lost particles. We selected the evolved extended run (M= 0.03

M_{Jup}, $e = 0.4$) for fitting due to the larger number of TPs and extended duration. This simulation defined the 'best-case' planet, as higher masses resulted in shorter TP lifetimes and greater ejection fractions while larger eccentricities have yet to be observed above 0.4 for low-mass planets. The best-fit values were $\alpha = 7.4$, $t_* = 5.41 \times 10^6$ years, and $N_0 = 196$ particles. We also fit the cumulative distribution with bins in $\log_{10}$ space, which gave different values: $\alpha = 19.6$, $t_* = 2.64 \times 10^6$ years, and $N_0 = 405$ particles. The data and the fits are shown in Figure 2.18. Although the two sets of fitted constants differed greatly, the fits themselves produced similar fractions of material accreted, differing by less than a factor of two at any given time, allowing either fit to work in an estimate of the total unstable disk mass.

For the linear-fit values and a time of 10^9 years, Equation 2.16 gives 1.35×10^{-9} particles removed per year. Dividing by N_0 gives the fractional loss rate, 6.87×10^{-11} per year. We assume that the 25 per cent contamination from MS unstable material (Section 2.6.1.2) affects both the particle loss rate and N_0 equally, so the fraction is unaffected. Examining each loss mechanism individually as a function of time (shown in Figure 2.11), we find that the accretion rate equals roughly double the ejection rate after 10^7 years, and the planetary collision rate is negligible. Therefore we assume the accretion rate is two-thirds of the total loss rate, or $\approx 4.58 \times 10^{-11}$ of the initial material per year. We can compare this to the observed accretion rate of polluted WDs, roughly 10^8 g s^{-1} for WDs with cooling ages of 10^9 years (Farihi et al., 2010b), which gives an initial mass of unstable bodies in this system equivalent to 6.9×10^{25} g. This mass is roughly 23 times that of the asteroid belt, $\sim 3 \times 10^{24}$ g (Pitjeva, 2005), and one per cent the mass of the Earth (0.01 $M_\oplus$). While larger than previous estimates of the total accreted material (Zuckerman et al., 2010), this mass is negligible compared to that of our smallest planet and supports the use of massless TPs.

Using the results from Section 2.6.2, we repeated the calculation for our repopulated simulation with the same mass and eccentricity and found a larger required disk mass—the material in the repopulated regions reduced the fraction accreted at late times and thus the total amount was necessarily larger. More-massive and lower-eccentricity planets, as expected, required even greater initial disk masses, both due to the shorter lifetimes of small

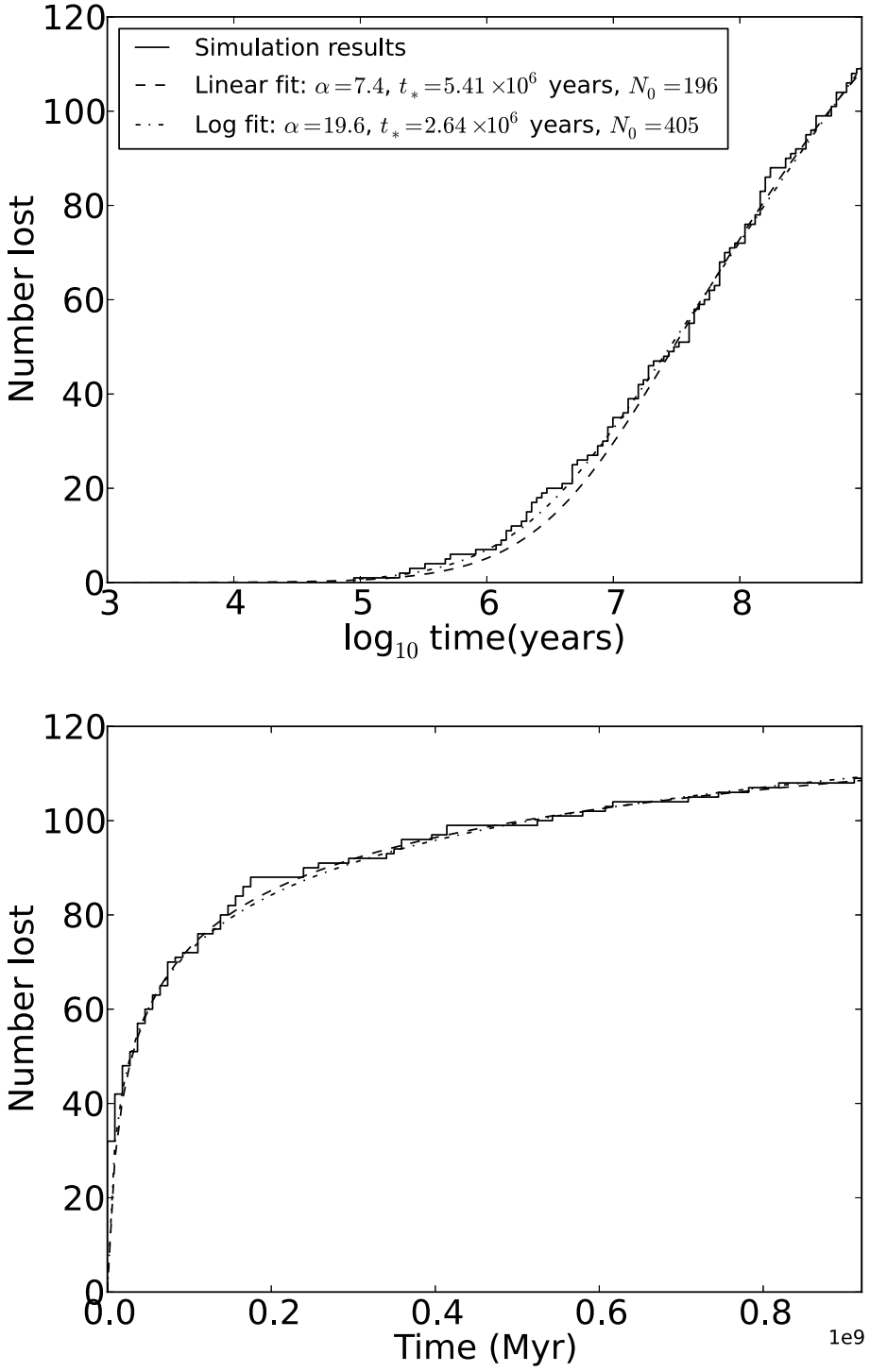

Figure 2.18 The cumulative number of particles lost through all mechanisms, as a function of time in $\log_{10}$ space (top) and linear space (bottom), with the power law fit to the log (linear) distribution shown in as a dash-dotted (dashed) line. These fits allowed us to specify the loss rate at 1 Gyr and beyond, which we compared to accretion rates around WDs to produce an estimate of the initial unstable mass.

bodies (in the case of massive planets) and due to the reduced fraction of accreted material relative to ejected material. Additionally, non-gravitational forces have only a minor effect on the required mass, due to the limited amount of motion provided to large bodies. As such, we conclude that for a planet orbiting at 7.42 AU about a 0.539 $M_\odot$ star with no external companions, an accompanying disk must have at least 0.01 $M_\oplus$ in unstable material in order to account for the observed levels of WD pollution even in the best case (lowest mass and highest eccentricity) scenario.

2.7.2 Observational and dynamical disk constraints

To determine whether this result is reasonable in the context of observed debris-disk masses, we extrapolate the total disk mass from the amount of unstable material. To do so, we assume that the unstable material is localized to a region between 11.7 and 12.7 AU, beyond which the objects are stable. We make this assumption based on the results of our extended-duration simulation (Section 2.6.1.2), in which the majority of unstable particles exterior to the planet were located in that region. We also assume the disk extends to 90 AU (expanded from 50 AU, in analogy with the edge of our solar system (Trujillo & Brown, 2001)) and has a surface density of the form $\Sigma(r) = \Sigma_0(r/r_0)^{-3/2}$ (Kenyon & Bromley, 2004). Integrating over the unstable part of the disk and equating that to the result of Section 2.7.1 allows us to determine Σ_0, from which we can calculate the total disk mass. Doing so, we find that the total mass, in both stable and unstable regions, is 0.5 $M_\oplus$, 50 times the unstable mass. This value is strongly dependent on the size of the disk as well as the presence of any other planets, which would carve out additional ECZs and reduce the amount of material remaining at the end of the MS.

This mass is not unreasonable, as observed debris disks show dust masses of $10^{-2} - 10^{-1}$ $M_\oplus$ around stars older than 1 Gyr (Wyatt, 2008). Due to the fact that large bodies dominate the mass while small bodies dominate the surface area for most planetesimal size distributions (Wyatt et al., 2007), the total mass of these observed disks can be as much as $10^3 - 10^5$ times larger (Löhne et al., 2008), well above our requirement. Furthermore, while this mass

is much larger than the asteroid belt, the latter may have been substantially thinned out by the peculiarities of Solar System evolution (e.g. Walsh et al. (2011)), making such a comparison unnecessarily restrictive. Minimum mass solar nebula estimates yield original masses ~ 100 times larger than the present value (Weidenschilling, 1977), more than enough to meet pollution requirements if concentrated in a narrow region similar to the current asteroid belt.

However, while massive disks are not uncommon around MS stars, the question of whether they survive near the star and at late times arises, due to the effect of collisional evolution and radiative forces depleting much of the material over the stellar lifetime. Assuming an infinite collisional cascade, Wyatt et al. (2007) show that such forces result in a maximum disk mass for a given age. This maximum depends on the physical properties of the disk such as width, distance from the star, and the properties of the constituent particles.

To determine if our required mass can exist in a disk 10 Gyr old, we calculated the maximum disk mass for both the unstable region and the total disk using the Wyatt et al. (2007) model. At the end of MS, the material will not have moved outward due to mass loss, so the unstable region will span 6.3 to 6.8 AU with the entire disk reaching 50 AU. Using these disk dimensions, a largest object size of 2000 km, and an assumed particle eccentricity of 0.25 (the forced eccentricity at 6.5 AU), we find that the maximum amounts of unstable and total material are 6×10^{-5} $M_\oplus$ and 0.16 $M_\oplus$, respectively. While our parameter selections can affect these values and increase the maximum total mass above our 0.5 $M_\oplus$ requirement, the amount of unstable material is dramatically smaller than what needs to exist to account for WD pollution regardless.

The assumption of collision equilibrium holding for all mass sizes has been challenged by Löhne et al. (2008), who argue that it is valid only at very late ages and show that massive disks can exist even at 10 Gyr for a range of parameters. We repeated the mass-remaining calculation using their formalism and the same disk parameters, and found that although the total disk mass was relatively unconstrained, the mass in the unstable region was limited to 10^{-3} $M_\oplus$. These results (shown in Figure 2.19) indicate that, while the disk mass can reach larger values at 10 Gyr than in the Wyatt et al. (2007) case, the masses still fall

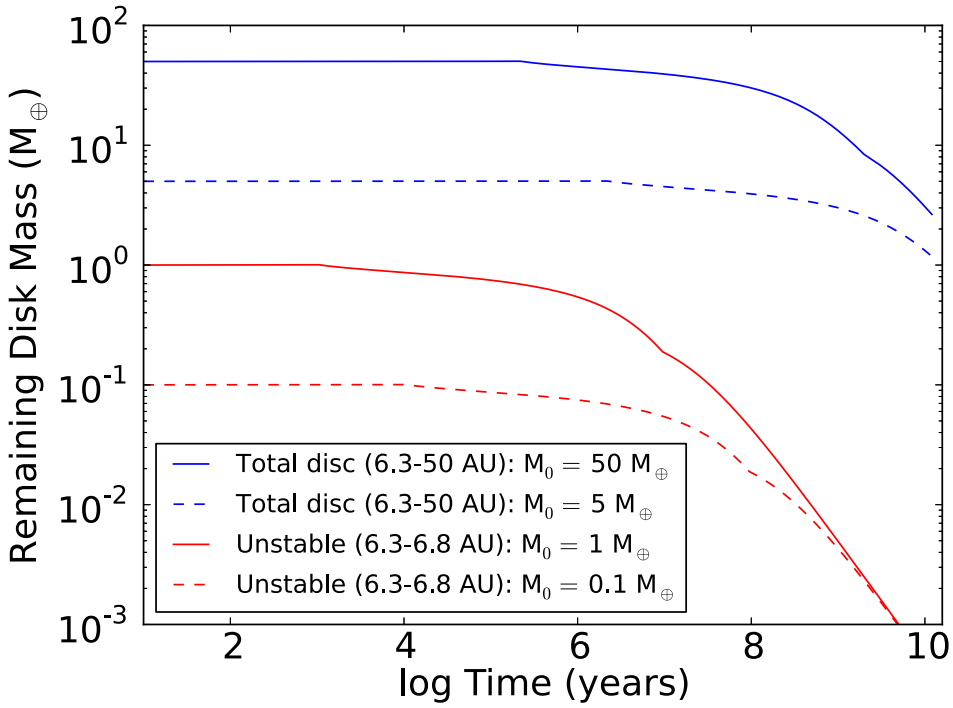

Figure 2.19 Evolution of disk mass as a function of time, for the total mass (blue) and the unstable mass (red). While the total mass is large enough to match the mass required by WD accretion rates, the unstable mass is over an order-of-magnitude smaller than our requirement (0.01 $M_\oplus$).

short of what is required to match observed pollution rates when the disk is near the star. Therefore, we determine that collisional evolution prevents a planet with a narrow unstable region from being a major source of WD pollution, unless it is significantly more distant than 4 AU during the MS or the star loses a significantly larger mass fraction. Alternatively, if collisional evolution of the material progresses differently from what current models predict, the original reservoirs could be massive enough to supply polluting material, depending on the planetary properties. We should mention that this collisional evolution may prevent the MMR-based mechanism discussed in Debes et al. (2012) from being a viable source of pollution as well, due to the massive asteroid belt required (0.35 $M_\oplus$) in their simulations.

2.7.3 Other system parameters

While we examined the effects of some planetary-system properties on WD accretion rates in detail, it is useful to consider the impact of other parameters as well. One such parameter is the initial SMA of the planet, which remained constant at 4 AU between all our cases. We ran a single simulation to investigate this effect, using a 0.03 M_{Jup}, $e = 0.4$ planet with an SMA of 10 AU. We found a small decrease in the fraction of particles accreted (from 83 per cent to 78 per cent) but a substantial increase in the fraction of TPs accreted in the last 50 Myr of the simulation, resulting from the increased orbital time-scale. That fraction increased from 3 per cent in the 4 AU case to 8 per cent in the 10 AU case, indicating that a smaller disk mass (both total and unstable) may be required for planets at larger distances.

Farther from the star the maximum disk mass should be greater, potentially allowing a single planet to be a source of WD pollution. As a test, we repeated our calculations to determine the maximum unstable mass in a disk scaled outward by a factor of 2.5. We found that, in a disk located from 15.75 to 17 AU with the same eccentricity and maximum object sizes as before, the Wyatt et al. (2007) and Löhne et al. (2008) approaches predict 10^{-3} $M_{\oplus}$ and 0.015 $M_{\oplus}$, respectively. Given the potentially-lower disk-mass requirement due to increased late-time accretion, these results indicate that more distant planets and disks may serve as a more-likely source of pollution.

The initial stellar mass also plays a major role in system dynamics, determining the orbital expansion experienced by the planet and other bodies. More-massive stars undergo greater mass loss, resulting in a larger expansion and potentially longer lifetimes as described above. The results of Wisdom (1980) predict that this larger expansion would have a correspondingly larger increase in the unstable region, which could result in a larger population of small bodies accreting on to the star. Furthermore, more-massive stars have shorter lifetimes, allowing them to retain more planetesimals. However, the larger separation from the central star would likely reduce the accretion fraction relative to our results, as we saw in the lower fraction for TPs around the WD compared to the MS star.

Doubling the stellar mass for some MS simulations, we saw a small increase in the fraction

of particles accreted along with a decrease in ECZ size, resulting in fewer total accreted. As a result of the shorter planetary period, the average lifetime of TPs shrank and thus even fewer particles accreted after 10^7 years. While we did not simulate the evolved case of this increased stellar mass, we can assume, from the two prior results, that the particle lifetimes would be longer and the accretion fraction less. The magnitude of the accretion reduction would depend on the total mass loss of the star, and therefore the initial stellar mass.

2.8 Conclusion

In this work we have simulated single-planet systems through stellar evolution, allowing us to detail the effect of planetary parameters on the WD accretion rate and determine that, when started in a disk initially at zero eccentricity, planets of mass ≤ 0.03 M_{Jup} and eccentricity $e \geq 0.4$ are the most-efficient perturbers. We find that more-massive planets deliver less material to their host star due to ejecting a much larger fraction of unstable particles, while smaller eccentricities also produce a lower accretion fraction in addition to fewer unstable particles. The mass in planetesimals, while found to be negligible for Jupiter-mass planets, can have dynamical consequences if the mass of the scatterer is too small; the use of massless TPs in simulations thus limits our results to planetary scatterers larger than several Earth masses. Particle lifetime varies inversely with both planetary mass and eccentricity, but the latter relationship is weak relative to the variation in overall accretion amount. These relationships remain for non-zero particle eccentricity, but are significantly weakened when particle longitude of periapse matches that of the planet.

We further find that stellar evolution has an impact as well, widening planetary and particle orbits thus causing an increase in the fraction of particles ejected and a decrease in the overall accretion amount. Longer orbital periods translate into later peak accretion times, which partially offset the latter effect. Additionally, while non-gravitational forces become stronger during stellar giant phases, they play a negligible role in the amount of stellar accretion due to strong dependence on planetesimal size.

Most importantly, we have demonstrated that single-planet systems within 8 AU of their

host WD can deliver the amount of material observed in polluted-WD atmospheres through the scattering of small bodies from reservoirs similar in mass to that which existed early in our own planetary system. These small bodies were assumed to be at random points on circular orbits at the beginning of the MS. For a low-mass, high-eccentricity planet (0.03 M_{Jup}, $e = 0.4$) at an SMA of 7.42 AU, 10^{-2} $M_{\oplus}$ of unstable material would be required in a disk annulus 1 AU wide, which is within observational amounts. However, current models of collisional evolution predict that the accompanying disk cannot retain an adequate reservoir of material, as much of it is ground down to dust and lost from the system. If these collisional models are correct, more distant planets (where disk evolution progresses more slowly) or planets that are scattered to other portions of the disk (as described in Debes & Sigurdsson (2002)) remain a possible source of pollution.

We finish by mentioning that, so far, no planets have been discovered orbiting a WD, regardless of metal pollution or infrared excess (Faedi et al., 2011; Hogan et al., 2009). This is unsurprising in the context of our results, given the low mass of a planet necessary to destabilize small bodies and the current difficulty in detecting exoplanets around any star at 7 AU. With radial-velocity detections limited to greater than ~ 1 km s^{-1} due to pressure broadening of spectral lines (Maxted et al., 2000), even massive planets are unlikely to be detected in that manner. If planets such as super-Earths and Neptunes are significantly more common than more-massive planets as sources of pollution, then it would further reduce the possibility of detecting them in the future through methods such as direct detection and astrometry.

CHAPTER 3

The Effect of Stellar Evolution on Migrating Warm Jupiters

3.1 Introduction

Arguably the biggest surprise in the field of exoplanets was the discovery of HJs, those extrasolar planets with orbital periods less than 10 days but masses near that of Jupiter (M_J) (Mayor & Queloz, 1995; Butler et al., 1997). The proximity of these planets to their host precludes them from forming at their observed location (Bodenheimer et al., 2000), indicating that they must have migrated after formation. A range of migration mechanisms have been proposed, including disk migration (Lin et al., 1996) and planet-planet scattering (Rasio & Ford, 1996; Weidenschilling & Marzari, 1996), but the existence of HJs that are inclined relative to the spin of their host star (Hébrard et al., 2008; Winn et al., 2010; Triaud et al., 2010; Albrecht et al., 2012) indicates that at least some migrated via a mechanism that excites the planetary inclination to high values. One of these is the Kozai-Lidov (KL) mechanism (Kozai, 1962; Lidov, 1962), in which an inner body oscillates between highly eccentric and highly inclined modes due to an inclined, external perturber. Recent results have shown that the KL mechanism naturally leads to misaligned and flipped planetary orbits, indicating it may contribute significantly to the formation of HJs (Naoz et al., 2011, 2012, 2013a; Li et al., 2014a; Teyssandier et al., 2013; Petrovich, 2015).

Orbital decay and circularization do not occur instantaneously during high-eccentricity migration, which results in the related population of WJs. These planets are similar to HJs but orbit at larger periods of 10 to 100 days. The existence of eccentric WJs implies a migration mechanism that increases planetary eccentricity, which is consistent with KL

oscillations. The dominant migration mechanism has important implications for the WJ population around evolving stars. As stars evolve off the main sequence and increase in size, they can tidally drag in and engulf planets orbiting too closely (Rasio et al., 1996; Passy et al., 2012; Nordhaus & Spiegel, 2013; Li et al., 2014b). The eccentricity of a planet plays an important role in its survival, as tidal effects are dramatically increased for highly eccentric planets. For planets undergoing KL oscillations, the evolution of their orbits would be determined by their maximum rather than current or observed eccentricity. An observed population (or lack thereof) of WJs around evolved stars can then give us insight into whether the population is made up of planets with constant eccentricities, or if most go through phases of significantly larger eccentricity. This process may explain the lack of HJs and WJs observed around subgiant stars (Johnson et al., 2007, 2010; Schlaufman & Winn, 2013), as shown in Figure 1.

In this paper we examine how a population of migrating and oscillating WJs would be affected by the evolution of their host stars compared to an observationally identical population with constant eccentricities, and determine how it compares to observations. To do so, we run numerical simulations of a WJ and a perturber over the full period range and determine the relationship between system properties, the closest approach of the planet, and how rapidly the planets move inward. With this data we calculate at what size the star removes migrating WJs, for the oscillating population and the analogous non-oscillating systems. We find that KL oscillations do cause planets to be removed much earlier in stellar evolution, in line with the observed distribution of stellar sizes for WJ hosts. The oscillations required to induce inward migration also result in planets spending a significant amount of time at eccentricities higher than that seen in the observed WJ population, but the latter may be subject to observational biases.

The structure of the paper is as follows: In Section 3.2 we estimate the number of WJs predicted around evolved stars relative to the number observed. In Section 3.3 we review the relevant dynamics taking place in systems undergoing KL oscillations. In Section 3.4 we setup our numerical simulations of migrating, oscillating WJs. In section 3.5 we discuss our numerical results, and examine the relative effect of stellar expansion on oscillating and non-

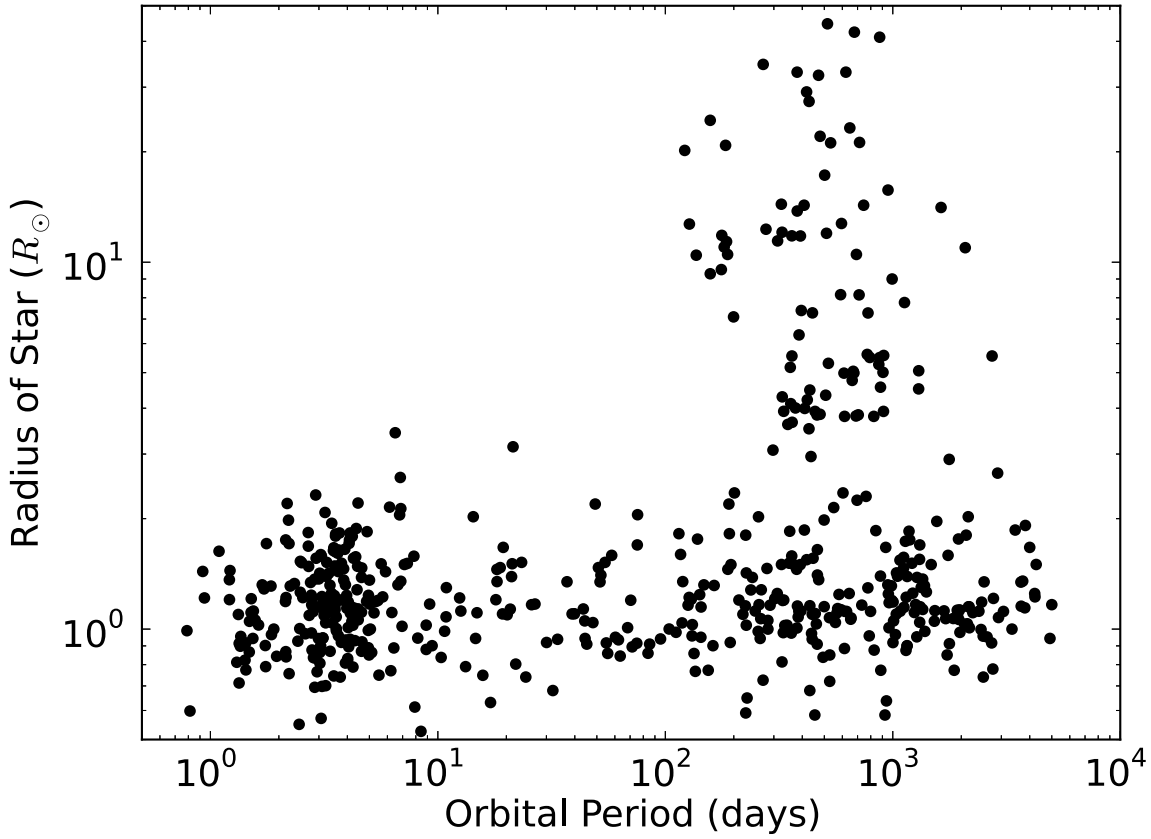

Figure 3.1 Confirmed exoplanets from Exoplanet Orbit Database with $M_{\rm p} \sin i > 0.1 M_{\rm J}$ or $R_{\rm p} > 0.5 R_{\rm J}$. Few WJs are observed around stars larger than $2R_\odot$.

oscillating populations in Section 3.6. In Section 3.7 we compare our results to observations and discuss the possibility that observational bias explains the discrepancy between the observed and simulated eccentricity distributions. In Section 3.8 we review our conclusions.

3.2 The missing warm jupiters

The lack of HJs and WJs around stars larger than $2R_\odot$ is apparent from a cursory examination of Figure 3.1. While the small ($\lesssim$ 10 days) orbits of HJs naturally lead to their engulfment early on in stellar evolution, the lack of WJs at similar stellar sizes in spite of orbits ~ 10 times larger is surprising. However, the number of WJs around stars of all sizes,

and the number of exoplanets around evolved stars at all periods, are both significantly lower than in other regions of exoplanet period–stellar-radius parameter space. This contrast raises the question of whether the number of WJs around larger stars is genuinely below observational predictions, or if they simply reside in a particularly barren region of parameter space. We answer this question using the observed number of WJs around main-sequence stars ($R_* = 1-2R_\odot$) and their observed periapse values, combined with the observed number of lukewarm Jupiters (LJs, periods of $100 - 1000$ days).

The number of planets observed around evolved stars of a radius R_* is

$$N_{\rm p,obs}(R_*) = N_{*,\rm obs}(R_*) f_{\rm p,0} f_{\rm p,S}(R_*) \tag{3.1}$$

where $N_{*,\rm obs}(R_*)$ is the number of stars observed at a given stellar radius, $f_{\rm p,0}$ is the initial frequency of planets around the stars, and $f_{\rm p,S}(R_*)$ is the fraction of planets that have survived prior stellar evolution.

For WJs and LJs around unevolved ($R_* = 1 - 2R_\odot$) stars, we get

$$N_{\rm WJ}(1-2R_\odot) = N_{*,\rm obs}(1-2R_\odot) f_{\rm WJ,0} f_{\rm WJ,S}(1-2R_\odot) \tag{3.2}$$

$$N_{\rm LJ}(1-2R_\odot) = N_{*,\rm obs}(1-2R_\odot) f_{\rm LJ,0} f_{\rm LJ,S}(1-2R_\odot) \tag{3.3}$$

Assuming survival rates are similar without stellar evolution, the relative fraction of stars with WJs and LJs is:

$$\frac{f_{\rm WJ,0}}{f_{\rm LJ,0}} = \frac{N_{\rm WJ}(1-2R_\odot)}{N_{\rm LJ}(1-2R_\odot)} \tag{3.4}$$

Equation 3.1 holds for larger stellar radii as well:

$$N_{\rm WJ}(>2R_\odot) = N_{*,\rm obs}(>2R_\odot) f_{\rm WJ,0} f_{\rm WJ,S}(>2R_\odot) \tag{3.5}$$

$$N_{\rm LJ}(>2R_\odot) = N_{*,\rm obs}(>2R_\odot) f_{\rm LJ,0} f_{\rm LJ,S}(>2R_\odot) \tag{3.6}$$

Dividing these two equations, we get the predicted number of WJs around evolved stars based on their observed number around main-sequence stars and observed number of HJs:

$$N_{\rm WJ}(> 2R_\odot) = \frac{N_{\rm WJ}(1-2R_\odot)}{N_{\rm LJ}(1-2R_\odot)} \frac{f_{\rm WJ,S}(> 2R_\odot)}{f_{\rm LJ,S}(> 2R_\odot)} N_{\rm LJ}(> 2R_\odot) \tag{3.7}$$

Assuming all LJs survive ($f_{\rm LJ,S}(> 2R_\odot) = 1$) gives the most conservative estimate for the number of WJs. Observations provide values for $N_{\rm WJ}(1-2R_\odot)$, $N_{\rm LJ}(1-2R_\odot)$, and $N_{\rm LJ}(R_* > 2R_\odot)$, as detailed below, so an estimate for $f_{\rm WJ,S}(> 2R_\odot)$ allowed us to calculate the predicted number of WJs around evolved stars, $N_{\rm WJ}(R_* > 2R_\odot)$. To do so we assumed the observed periapse distribution for WJs around unevolved stars is representative of the true periapse distribution. We also assumed that exoplanets are removed when their periapse comes within 2.5 stellar radii of their host (based on the smallest observed periapse-to-stellar-radius ratio, 2.7, in the case of WASP-12b as reported by Maciejewski et al. 2011).

The data for this estimation came from Exoplanet Orbit Database (Wright et al., 2011). We limited our dataset to massive planets[1] with listed eccentricity[2] values. We also excluded possible brown dwarfs[3], as such massive bodies may have formed via a different mechanism than exoplanets. Finally, we used the periapse distribution for planets around stars with radii $1 - 2R_\odot$, rather than including planets around smaller or larger stars[4]. From these values we calculated the predicted number of observed WJs as a function of stellar radius.

As illustrated by Figure 3.2, this calculation predicted a significant population (15) of observed WJs around evolved stars, which is inconsistent with the observed number (2). If, however, each WJ is oscillating between some minimum and maximum value of eccentricity, then fewer will survive stellar expansion as they are removed at their minimum periapse (at maximum eccentricity), rather than the value currently observed. By assuming all WJs are undergoing these oscillations up to a maximum eccentricity of $e_{\rm max} = 0.85$, we calculated a predicted number (2) that equals the value from observations (Figure 3.3).

[1]Due to some anomalously low values in the `MASS` keyword, we included planets with either `MSINI > 0.1` or `R > 0.5`.

[2]To avoid excluding planets on circular orbits, we used the filter `ECC > -1`.

[3]using the limit `MASS < 10`.

[4]The periapse dataset used `RSTAR >= 1.0 and RSTAR < 2.0`.

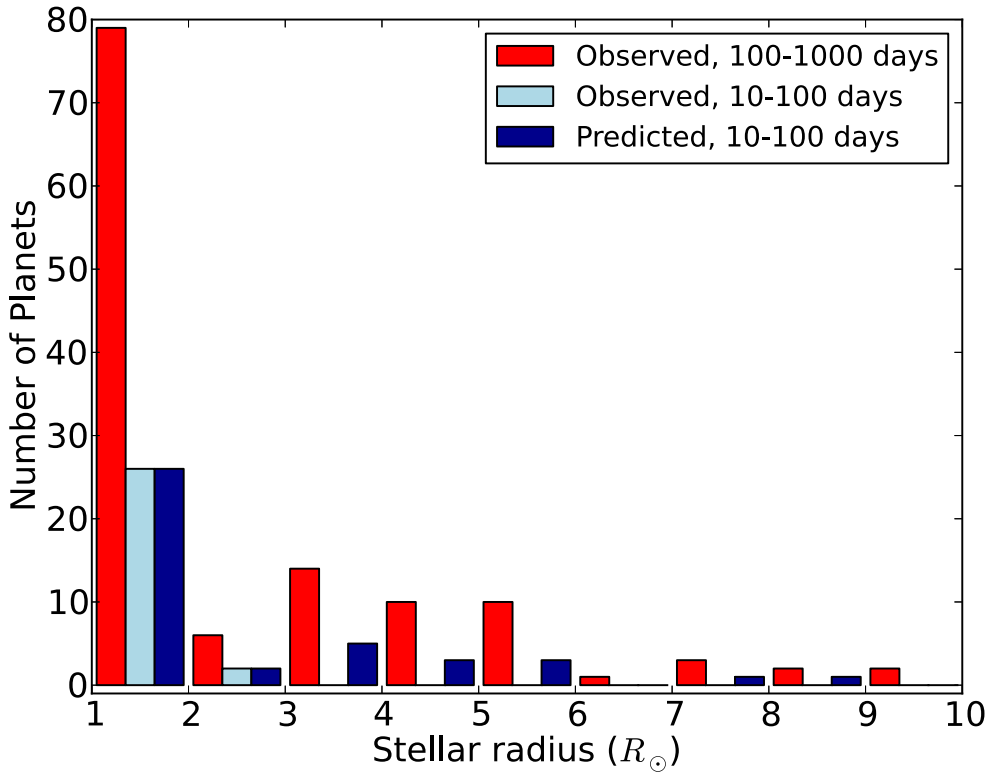

Figure 3.2 The number of observed LJs, WJs, and predicted WJs as a function of stellar radius. Only planets with listed eccentricity values are included. The predicted number is the result of a constant ratio between LJs and WJs along with exoplanet removal for periapse within $2.5R_{\rm star}$.

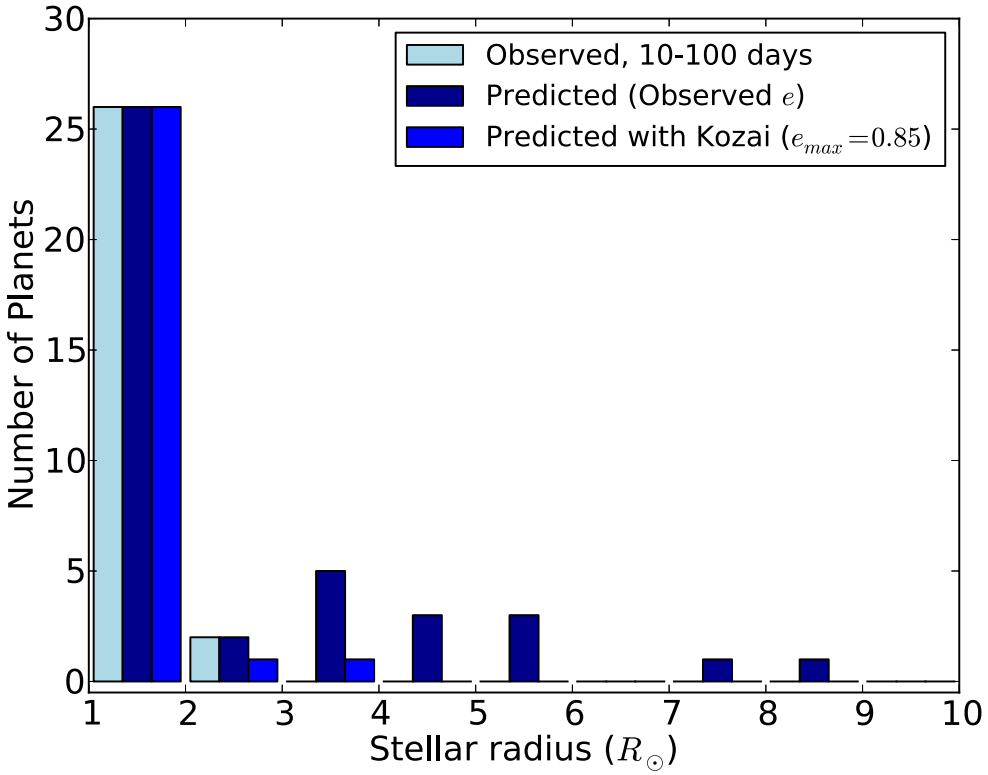

Figure 3.3 Similar to Figure 3.2, but including the predicted number of WJs when they are all assumed to be oscillating up to a maximum eccentricity of 0.85. While the match is not perfect, it dramatically reduces the discrepancy between observed and predicted at stellar radii above $2R_\odot$ compared to the observed eccentricity distribution.

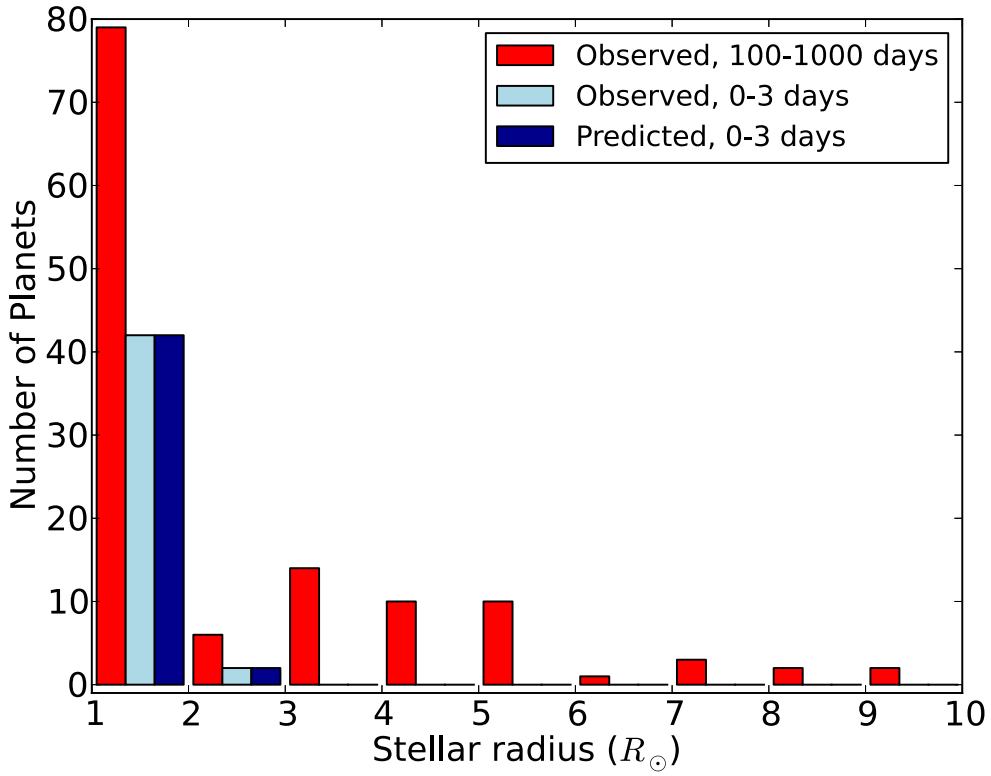

Figure 3.4 The observed number of LJs and the observed and predicted number of very hot jupiters (Period$<$ 3 days) as a function of stellar radius. Unlike the predicted number WJs, the predicted number of these planets matches observations without any variation in the periapse distribution.

We make a similar estimate of the number of missing HJs using planets on periods $<$ 3 days, which are very unlikely to be oscillating given the strong tidal interactions at such short periods. Figure 3.4 shows that the observed number of planets agrees with the number predicted by the current eccentricity distribution and does not benefit from a periapse distribution shifted to lower values.

This brief calculation illustrates that the lack of WJs is unlikely to be a simple statistical fluctuation, and necessitates an explanation. We note that it does include a number of assumptions, foremost being that the relative frequency of WJs to LJs is independent of stellar radius outside of removal via tides. However, the purpose of this calculation is not to determine the precise number of WJs removed to due stellar evolution, but rather to

demonstrate that an absence exists and can be accounted for they are oscillating to higher eccentricity values, as would be required for migration via tides. A more detailed analysis follows in Section 3.6, with further discussion of assumptions in Section 3.7.

3.3 Dynamical effects

3.3.1 The Kozai-Lidov mechanism

The KL mechanism results from secular (long-term) interactions between an inner and outer body when their mutual inclination exceeds some nominal value, or if both bodies have significant eccentricity while coplanar (Li et al., 2014a). In the simplest case, where the inner body has negligible mass and the outer body is on a circular orbit, the z-component of the angular momentum is constant for the inner body:

$$\cos i_{\rm in}\sqrt{1-e_{\rm in}^2} = \text{Const} \tag{3.8}$$

where $i_{\rm in}$ is the inclination of the inner body (identical to the mutual inclination in the massless case) and $e_{\rm in}$ is its eccentricity.

This relationship requires that a decrease in mutual inclination between the two bodies is accompanied by an increase in the eccentricity of the inner body. As a result, the inner body undergoes oscillations in eccentricity and inclination as it is forced by the outer companion. In this simple case these oscillations are characterised by their timescale ($P_{\rm Kozai}$) and maximum eccentricity (Lidov, 1962; Kiseleva et al., 1998):

$$P_{\rm Kozai} = \frac{2}{3\pi}\frac{P_{\rm out}^2}{P_{\rm in}}\frac{M_{tot}}{M_3}(1-e_{\rm out}^2)^{3/2} \tag{3.9}$$

$$e_{\rm calc} = \sqrt{1-(5/3)\cos^2 i_0} \tag{3.10}$$

where $P_{\rm in}$ and $P_{\rm out}$ are the inner and outer periods, respectively; M_3 and $M_{\rm tot}$ are perturber mass and total mass of all the bodies, respectively; $e_{\rm out}$ is the perturber eccentricity; i_0 is

the minimum value of $i_{\rm in}$; and $e_{\rm calc}$ is the calculated maximum eccentricity. The maximum eccentricity has a more complicated, non-linear form when the inner body is massive. Naoz et al. (2013a) derive the equation in the case of no initial eccentricity and a perturber on a circular orbit:

$$\left(\frac{L_1}{L_2}\right)^4 e_{\rm calc}^2 + \left(3 + 4\frac{L_1}{L_2}\cos i_0 + \left(\frac{L_1}{2L_2}\right)^2\right) e_{\rm calc}^2 + \frac{L_1}{L_2}\cos i_0 - 3 + 5\cos^2 i_0 = 0 \tag{3.11}$$

where L_1 and L_2 are the scaled angular momenta of the inner and outer orbit, respectively. These are defined as:

$$L_1 = \frac{M_1 M_2}{M_1 + M_2}\sqrt{G(M_1 + M_2)a_{\rm in}} \tag{3.12}$$

$$L_2 = \frac{M_3(M_1 + M_2)}{M_1 + M_2 + M_3}\sqrt{G(M_1 + M_2 + M_3)a_{\rm out}} \tag{3.13}$$

where M_1, M_2, and M_3 are the masses of the central body, inner body, and perturber, respectively, and $a_{\rm in}$ and $a_{\rm out}$ are the inner and outer SMA. Including the initial eccentricities of both orbits modifies the calculation only slightly and gives a value that differs at most by a few percent.

The KL mechanism has been covered extensively in the literature in a number of contexts, including asteroids (Fang & Margot, 2012), exoplanet systems (Naoz et al., 2011; Petrovich, 2015), the dynamics of the Galactic Center (Löckmann et al., 2008), and stellar triple systems (Eggleton & Kiseleva-Eggleton, 2001; Fabrycky & Tremaine, 2007; Thompson, 2011; Prodan et al., 2013; Naoz & Fabrycky, 2014). Recently it has been shown that the inclusion of higher-order terms can dramatically alter the oscillations induced by the KL mechanism. These octupole terms, which are non-zero if the inner body is not massless or the outer body has a non-zero eccentricity, can result in larger eccentricities, flips of the inner orbit, and chaotic behavior (Katz et al., 2011; Lithwick & Naoz, 2011; Naoz et al., 2013a). The full equations have no analytical solution for the maximum eccentricity of the inner orbit. However, Equation 3.11 still provides an adequate first-order estimate of $e_{\rm max}$, which we

use in Section 3.4 to limit our parameter space to those systems that could be capable of migrating inward.

In the absence of any other effects, oscillating bodies can approach within an arbitrary distance of the surface of the star as long as they avoid collision. However, two effects prevent that from happening: general relativity (GR) and tides.

3.3.2 General relativistic precession

For short-period orbits, GR causes a precession of apsides on a timescale that depends on the properties of the orbit and the host star:

$$P_{\rm GR} = \frac{P_{\rm in}^{5/3} c^2 (1 - e_{\rm in}^2)}{3(2\pi^{5/3})(GM_1)^{2/3}} \tag{3.14}$$

If $P_{\rm Kozai}$ is longer than this timescale, GR precession can damp and eliminate KL oscillations. For this reason, orbits with shorter periods require stronger perturbers to undergo oscillations: those that are more massive, closer, and/or more eccentric. As shown in Dong et al. (2014), WJs need perturbers within 10 AU to undergo the high eccentricity migration discussed here. This constraint is due in part to the eccentricity dependence of the GR timescale. Without a strong enough perturber, oscillating bodies that reach very high eccentricities can be stranded at their maximum eccentricity. When tides are taken into account, that can lead to rapid evolution into a HJ. While the detailed effects of GR are significantly more complicated (Naoz et al., 2013b), the damping interpretation is adequate for our purposes.

3.3.3 Tides

3.3.3.1 Tidal decay

Both the KL mechanism and GR conserve orbital energy, ensuring that the SMA of the inner orbit is constant. WJs can only migrate when under the influence of a dissipative force, which takes the form of tidal friction. The existence of WJs at their current periods, as well as their non-zero eccentricities, indicate that they must have large circularization and tidal decay timescales as a result of weak tidal forces. In this section we describe tidal forces that hold for two bodies in general, but in our simulations apply specifically to the planet and star.

The effects of tidal forces on orbital evolution (first investigated in the context of planets and satellites, see Darwin 1880) have been investigated in detail for stars, showing that tides reduce orbital energy and lead to smaller and more circular orbits (Hut, 1981; Eggleton et al., 1998; Kiseleva et al., 1998). For two tidally interacting bodies, whether massive planets or stars, the strength of tides raised on an object 1 by an object 2 is characterised by the tidal friction timescale, as described in Eggleton & Kiseleva-Eggleton (2001) and Fabrycky & Tremaine (2007):

$$t_{F1} = \frac{t_{V1}}{9}\frac{a^8}{R_1^8}\frac{M_1^2}{(M_1+M_2)M_2}(1-Q_1)^2 \tag{3.15}$$

where a is the SMA of the orbit and R_1 is the radius of object 1. The internal structure of object 1 is included by way of k, the classical apsidal motion constant, which represents the quadrupolar deformability of the star or planet, and t_V, the viscous timescale, which is a parametrization of internal dissipation in the star (Zahn, 1977). The physical values parametrizing tidal evolution are still not fully understood, although they have been investigated by a number of authors. The planetary k is frequently set to $k_{\rm P} = 0.25$, the result for a $n = 1$ polytrope representing gas giants. Recent research has gone into matching t_V to observations, including the Jupiter-Io system, the eccentricity distribution of hot Jupiters, and the existence of high eccentricity exoplanets. Hansen (2010) calibrated tidal models to observa-

tions of massive exoplanets (0.3-3 M_J) around solar-type stars using a single tidal dissipation constant for each population, and found that t_V for a Jupiter-mass planet with moderate eccentricity is $t_{Vp} = 150$ years. More recently, Socrates et al. (2012) determined that planets undergoing high-eccentricity migration require significantly stronger tides, equivalent to $t_{Vp} = 1$ year. It is this value we use in the numerical simulations of Section 3.5.

Hansen (2010) also found that tides raised on the solar-type host stars by Jovian-mass planets were a factor of 50 weaker than those raised on the planets by the stars, allowing us to ignore stellar tides for our numerical simulations. However, this inequality does not hold as stars evolve. The strong radius dependence of t_{F*} indicates that as a star leaves the main sequence it will increase its contribution to the planet's orbital evolution until stellar tides dominate or the star engulfs the planet. Once the star dominates tidal effects the strong radius dependence will rapidly accelerate the inward migration of the planet. Whether this increase in migration rate occurs before direct collision with the star depends on the migration rate due to planetary tides alone, as discussed in greater detail in Section 3.6.2. When stellar tides are included, we use the values $k_* = 0.014$, based on an $n = 3$ polytrope, and $t_{V*} = 50$ years, from the equation provided in Eggleton & Kiseleva-Eggleton (2001). Stellar tides are likely weaker than this value, as seen by the results of Hansen (2010), but our choice of t_{V*} does not affect our conclusion as long as it is longer than t_{Vp}.

3.3.3.2 Rotational effects

Tidal forces also exert a torque on a planet, changing its spin and aligning it on timescales much shorter than those required to circularize the orbit or move the planet inward. Planetary systems residing in the WJ period range as a result of migration should have reached an equilibrium in their spin as a result of this effect. In the case of planets not undergoing oscillations in eccentricity, the equilibrium spin can be determined by the value which results in no torque, or pseudo-synchronous (PS) spin (Hut, 1981). In the case of low eccentricity, the planetary spin period is the same as its orbital period (synchronous rotation). For large values of eccentricity, the planet is moving much more rapidly at periapse, where tidal forces

are strongest, and as a result the planet rotation period can be less than 1 percent of the orbital period. Those planets rotating faster than the PS value will have angular momentum transferred from its rotation to its orbit, which can result in a modest increase in SMA.

3.3.4 Stability

Finally, for these three-body systems to exist they must be stable. While KL oscillations require a strong perturber to avoid damping by GR, a perturber that is too near to the inner orbit will destabilize the system. The limit for stability in mutually inclined systems with an eccentric perturber was calculated by Mardling & Aarseth (2001):

$$\frac{a_{\rm out}}{a_{\rm in}} > 2.8(1+q)^{2/5}\frac{(1+e_{\rm out})^{2/5}}{(1-e_{\rm out})^{6/5}}\left(1-0.3\frac{i_{\rm tot}}{180^\circ}\right) \tag{3.16}$$

where $q = M_3/(M_* + M_p)$.

With these effects in mind, the planetary systems we want to investigate are those that are undergoing KL oscillations, requiring $P_{\rm Kozai} < P_{\rm GR}$ over the full range of eccentricities that the planet reaches. The maximum eccentricity due to oscillations should be large enough to induce tidal decay, but over a timescale large enough that a population of WJs would be detectable.

3.4 Numerical simulations

The orbital evolution of an oscillating planet depends on both the maximum eccentricity and the distribution of eccentricity values over time. These properties of the system do not have an analytical form; the maximum eccentricity deviates from $e_{\rm calc}$ in Equation 3.11 due to octupole terms, while the eccentricity distribution has no analytic form even without octupole terms. In order to understand the orbital evolution of migrating WJs, we need to use numerical simulations spanning the parameter space of interesting systems. These simulations allow us to determine the orbital decay as a function of initial period, mass, and eccentricity, as well as determine the relationship between calculated ($e_{\rm calc}$) and true maxi-

mum eccentricity. In our simulations we used S. Naoz secular code (private communications) which integrates the three-body secular equations up to the octupole level of approximation (Naoz et al., 2013a), including GR effects for the inner and outer orbits (Naoz et al., 2013b) and tidal effects following Eggleton & Kiseleva-Eggleton (2001) and Fabrycky & Tremaine (2007). This code has been used extensively in numerous calculations e.g. Naoz et al. (2011, 2012); Naoz & Fabrycky (2014); Li et al. (2014b, 2015).

3.4.1 Creating a population

Each system is composed of a central star, an inner body (hereafter referred to as "planet"), and an outer body (hereafter referred to as "perturber"). For our star, we selected a mass of 1.2 $M_{\odot}$ and ignored the contribution of tides raised on the star to the tidal evolution of our planetary orbit (see Section 3.3.3.1). The other properties of our systems were chosen to produce all three of the following properties in the planet:

1. Warm ($P = 10 - 100$ days) Jupiters ($M_p = 0.1 - 10 M_J$)
2. Undergoing KL oscillations
3. Experiencing migration

Each of these qualities introduces constraints onto the population: 1) constrains the mass and period of the planets, 2) constrains the perturber such that GR timescale is longer than the KL timescale, and 3) constrains the planet to reach high eccentricities during oscillations. Our choice in perturber and planet properties are discussed below.

3.4.1.1 Perturber properties

We limited the parameter space of our primary simulations by keeping the perturber constant across them. We selected its properties such that it caused KL oscillations in the systems at ~ 0.1 AU, which were most sensitive to quenching by GR (Section 3.3.2, constraint 2 above), while avoiding system instability in the largest orbits (0.45 AU). We arrived at a 4 M_J body at 2 AU with an eccentricity of 0.13, similar to the planets that appear to be common

companions to HJs (Knutson et al., 2014). Plugging these numbers into Equation 3.16, we find that the limit for stability is $a_{\rm out}/a_{\rm in} > 3.5$. Our systems have $a_{\rm out}/a_{\rm in} = 4.4-20$, clearly in the stable regime. Additionally, we ran two other sets of simulations: one with simply a larger eccentricity (0.35), and one with a larger ($30M_J$), more eccentric ($e = 0.64$) perturber at a larger distance (10 AU), both discussed in Section 3.5.3.2. These simulations showed that while the perturber plays a pivotal role in the planetary oscillations and migration, the perturber properties did not impact our general results.

3.4.1.2 Inner planet properties

We defined our population of WJs to be $0.1 - 10M_J$ and $10 - 100$ days, or $0.1 - 0.45$ AU. For simplicity, we set the size of all planets to 1 Jupiter radius, with $k_p = 0.25$ and $t_V = 1$ year as described in Section 3.3.3.1. While planets at the low-mass end of our population are unlikely to be this large, there is not a firm mass-radius relationship for extrasolar planets at this point. We discuss the impact of this assumption in Section 3.5.2.2. To generate the properties of our planet, we first randomly sampled the mass range, initial eccentricity, and mutual inclination. We did so logarithmically in mass and uniformly in eccentricity and inclination, limiting the latter to $0 - 0.1$ and the former to $70° - 90°$. We chose these boundaries with the goal of matching the high number of observed WJs with near-circular orbits while still allowing planets to reach large eccentricities and migrate inward.

From these properties and those of the perturber, we calculated $e_{\rm calc}$ for all samples using Equation 3.11. We then selected a uniform distribution in initial eccentricity and $e_{\rm calc}$ by dividing the parameter space up into a grid and selecting systems from each grid box, as shown in Figure 3.5. This approach allowed us to probe the wide range of behavior caused by different minimum periapse values while still limiting computation time. We constrained the initial eccentricity to between 0 and 0.1 and $e_{\rm calc}$ between 0.75 and 1.0 to produce oscillating systems that eccentricity values enabling migration. While $e_{\rm calc}$ is only accurate for systems without any contribution from octupole terms, it gave us a first approximation and allowed us to exclude systems that are unlikely to migrate. We also set both arguments of periapse

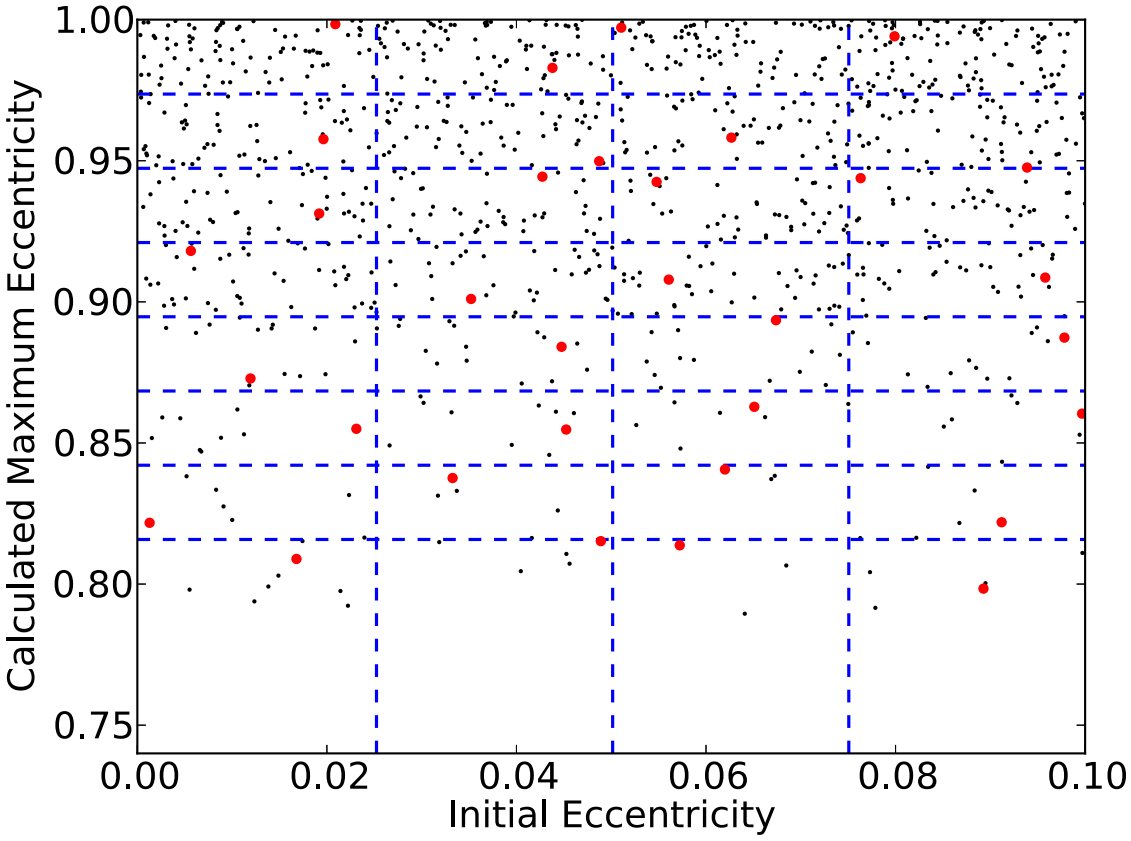

Figure 3.5 A randomly generated distribution of planets based on our limits (black points), along with the bins (blue lines), and a set of selected systems (red dots). This approach ensured we simulated a wide range of systems rather than be dominated by the portions of parameter space with the majority of points.

to zero in order to limit our parameter space, as other groups have done (Teyssandier et al., 2013). Generally speaking, this assumption is equivalent to maximizing the effect of the companion, leading to the largest peak eccentricity.

3.4.1.3 Planetary rotation

As described in Section 3.3.3.2, planetary rotation can have a significant effect on orbital evolution via tides. We tested this by running a set of simulations with a range of planetary rotation rates and found that as expected planets spinning faster than the equilibrium (PS) rate migrated more slowly, or in some cases migrated outwards. Because these systems are

assumed to be migrating WJs, which originated beyond periods of 100 days, they should have already reached PS rotation. For our main simulations, we used $e_{\rm calc}$ to estimate the PS rotation period. However, the planets nearest to the star (10 and 20 days) reached maximum eccentricity values significantly different from $e_{\rm calc}$, resulting in planets spinning too rapidly. To correct for this, we performed a linear fit between the calculated and simulated maximum eccentricity, and used the derived eccentricity value to set the correct rotation rate. We also set a lower limit on the spin period by capping the eccentricity used in its calculation to $1-2R_{\odot}/a$, the value that brings the planetary periapse to $2R_{\odot}$. This limit avoided spin rates that were unreasonably fast, exceeding the maximum physical rotation rate of a Jupiter-mass planet.

3.4.2 The full population

We ran a total of 1,320 simulations across 6 period values: 10, 20, 30, 50, 70 and 100 days. We also ran another 384 with different perturbers and 192 with reduced viscous timescale, both across the same period range. The number of simulations was chosen based on computational constraints, but effectively probed the parameter space (see Figure **??**). All simulations lasted 10^6 years or until the orbit of the planet decayed by 10 percent, whichever occurred first. While this is not enough time for most systems to complete migration, we are only interested in finding systems that have some measurable change in SMA and do not need to simulate the actual transition from WJ to HJ.

For comparison to systems not undergoing oscillations, we also ran an additional set of 192 simulations over the same period bins without the effects of a perturber. These simulations spanned both the same mass range (3 bins: 0.1, 1, 10 M_J) and the full eccentricity range (19 bins from 0 to 0.95), and began with the theoretical value for PS rotation at their eccentricity.

3.5 The results

3.5.1 A single system

As a case study, we selected a system with $M_p = 0.6 M_J$ at 50 days (0.28 AU), with an initial eccentricity of $e = 0.08$ and an initial mutual inclination of $i_0 = 72.3°$. Using Equation 3.11 we determined $e_{calc} = 0.91$, which is large enough to induce inward migration as long as the planet is not spinning extremely rapidly. This eccentricity corresponds to $5R_\odot$ at closest approach, well outside of the $2R_\odot$ limit we set for PS rotation calculations in Section 3.4.1.3. We set the rotation period to the calculated value of $P_{\rm rot}/P_{\rm orb} = 42$, or $P_{\rm rot} = 1.2$ days.

Simulating this planet for 10^6 years, we found that it peaked at an eccentricity of 0.93, slightly larger than our calculation (Figure 3.6). Additionally, the difference between the full 10^6 year distribution and the distribution in the last 10^5 years (thick line) showed that the minimum eccentricity during oscillations increased slightly over time. Given the distribution of eccentricity as a function of time, a system with these properties would most likely be observed with $e < 0.4$, but would be detected 25 percent of the time with $e > 0.7$. Migrating inward at 3 AU per Gyr, such a planet would survive for significantly less than the migration timescale $a/\dot{a} = 0.094$ Gyr, due the increase in the strength of tides as the SMA gets smaller. A migration timescale of this duration is short compared to the ages of WJ host stars, indicating that this type of system could have migrated to its current location from farther out.

3.5.2 All systems

Repeating this process on all 1,320 systems produces the results shown in Figure **??**: migration rate ($\Delta a/\Delta t$) as a function of minimum periapse/maximum eccentricity and planetary mass. These plots illustrate the extremely strong dependence of migration rate on maximum eccentricity, as expected. In all simulations with planet periods longer than 10 days, orbital migration only took place when the maximum eccentricity exceeded 0.8. This result is significant, as all observed WJs have eccentricities below this value (see Figure 3.19),

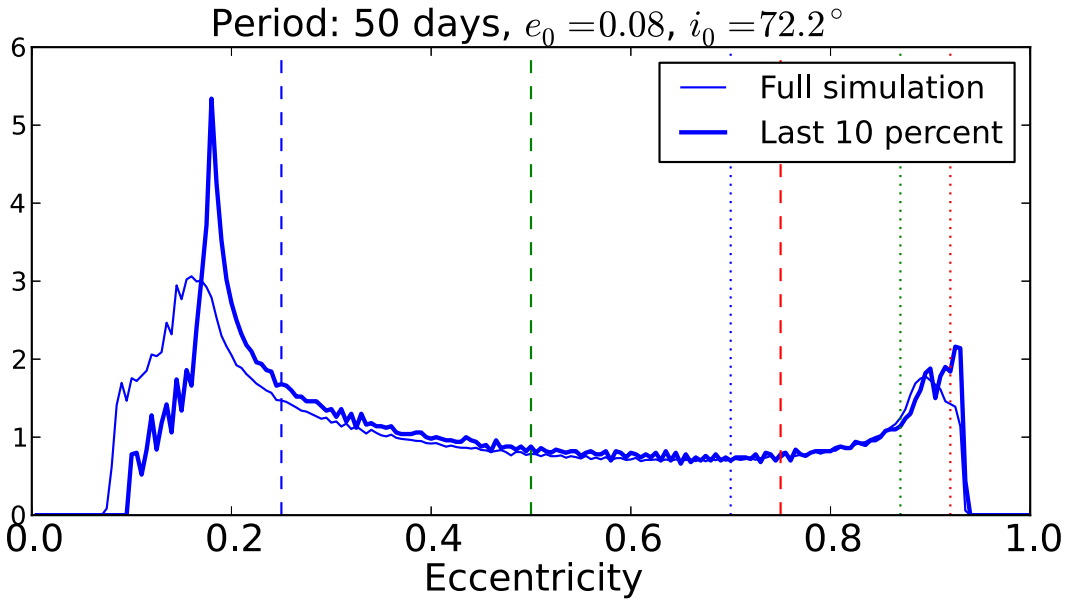

Figure 3.6 Eccentricity distribution of our 50-day case study planet, migrating inwards with $\Delta a/\Delta t = -3$ AU/Gyr, during the full 10^6 year simulation (thin line) and the final 10^5 years (thick line). The vertical lines show the distribution of observed WJ eccentricities (dashed, from the Exoplanet Orbit Database) and the simulated eccentricity distribution (dotted) at cumulative fractions of 0.75, 0.9, and 0.98.

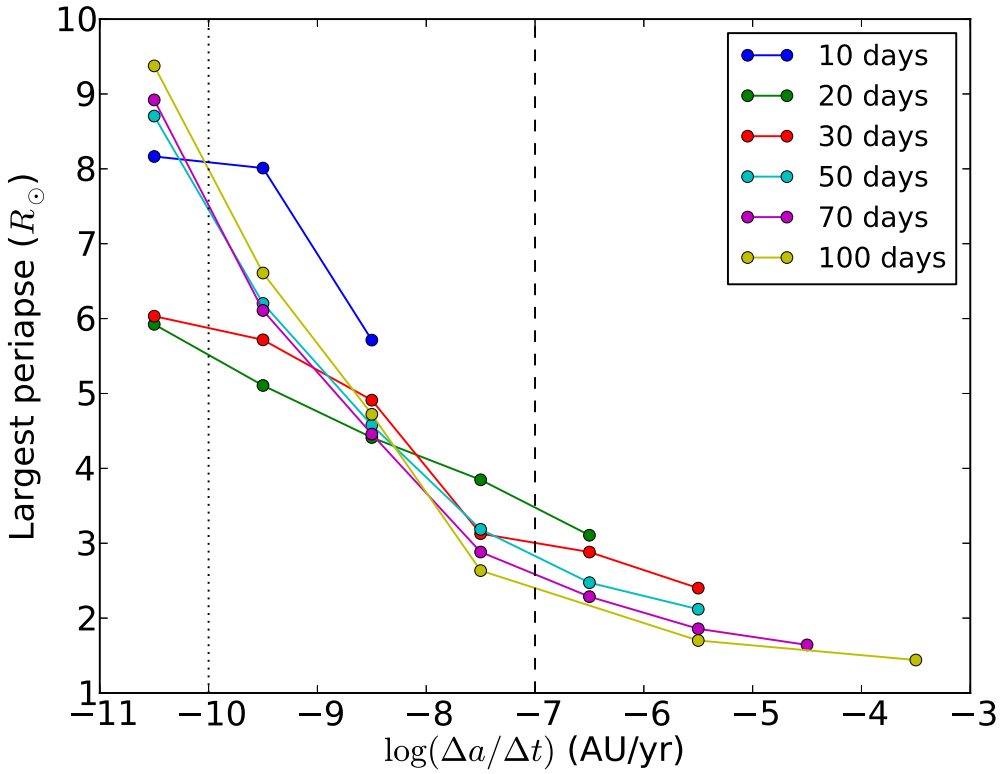

Figure 3.7 The largest minimum periapse that resulted in the planet migrating at a given rate, for each orbital period. The systems used in Section 3.6 fall between the dotted and dashed lines.

which will be discussed in Section 3.7. Notably, the same periapse distance results in similar migration rates regardless of period (Figure 3.7). This result plays an important role when determining how the population of WJs is affected by stellar evolution in Section 3.6. The partial exception to this phenomenon are those planets at 10 day periods, which are near enough to their host to experience tidal effects with even moderate eccentricity.

Additionally, some systems at larger periods migrated outward rather than inward. In these cases our estimate for the rotation rate was too high, possibly due to the effect of octupole terms in the KL oscillations or tidal effects, and they experienced outward migration due to their spin down. The relative symmetry between the outward and inward moving planets is due to the magnitude of migration being set primarily by the product of the tidal friction timescale (Equation 3.15) and a function of eccentricity dominated by a $(1-e^2)^{-13/2}$

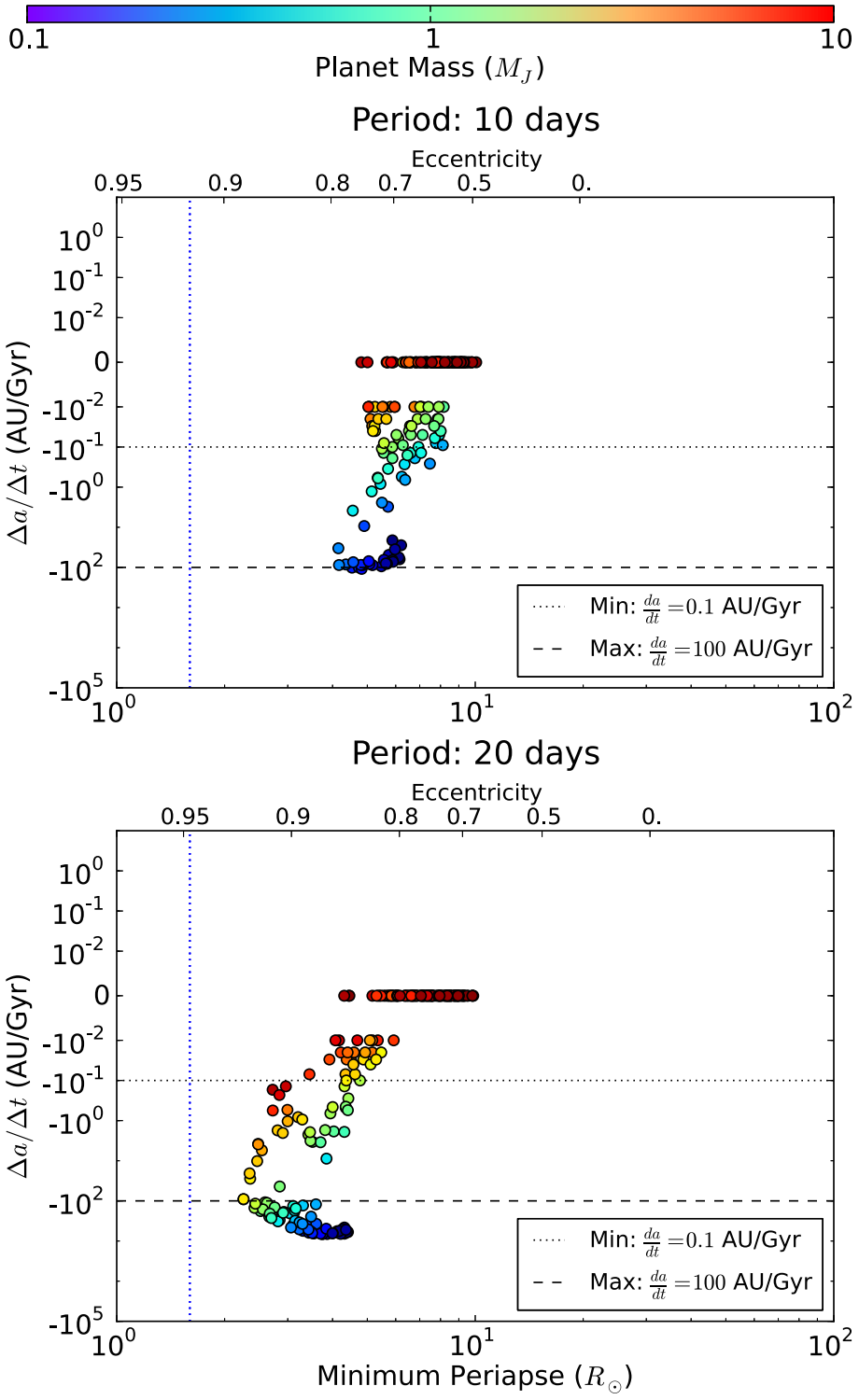

Figure 3.8 The change in semi-major axis over the duration of the simulation, for planets at 10- and 20-day periods. The x-axis is minimum periapse/maximum eccentricity while the color of the scatter points gives the mass of planet. Probable migration rates for the observed population of WJs are indicated by the region between the dotted and dashed black lines, while the blue dotted line indicates the tidal disruption radius.

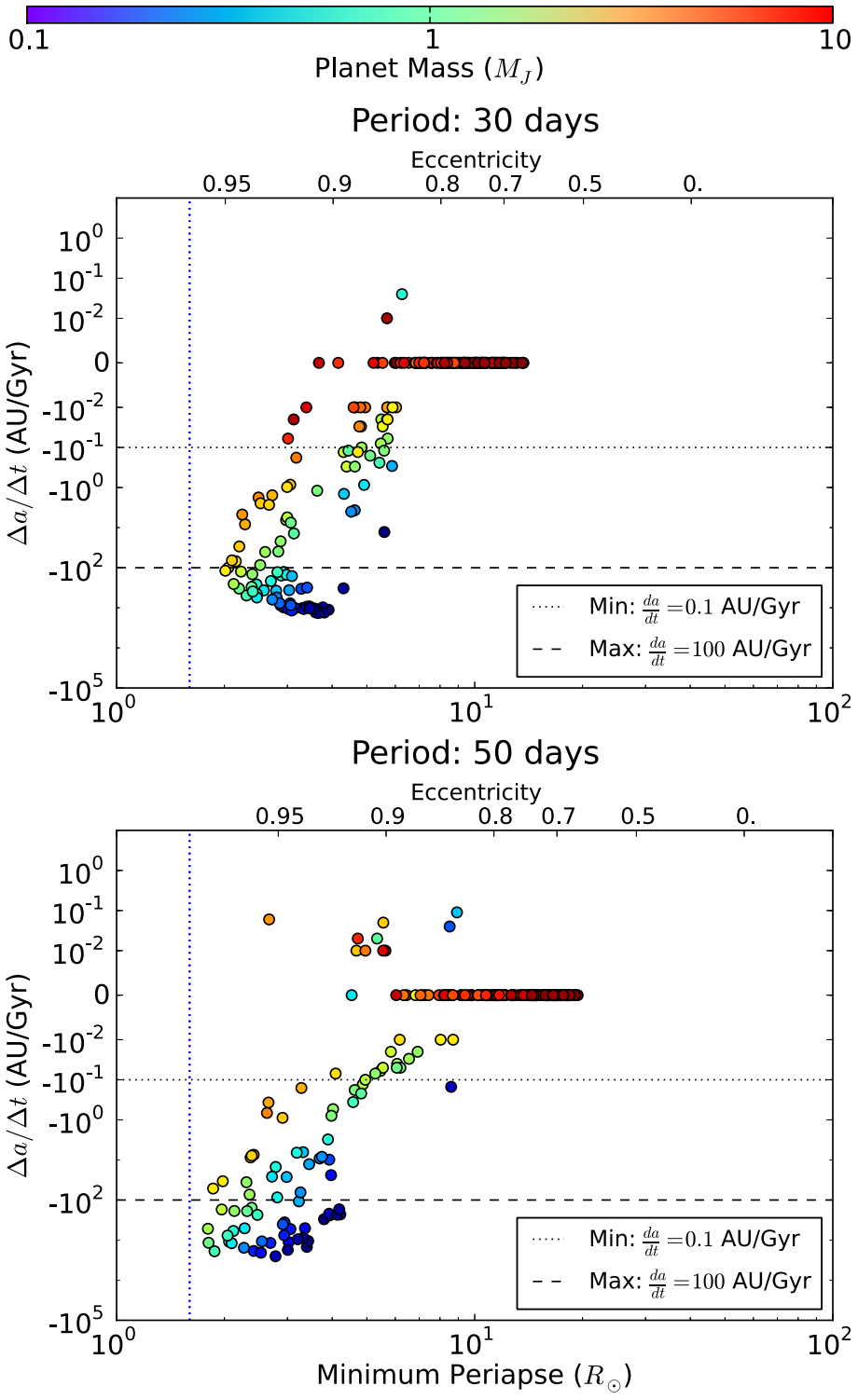

Figure 3.9 Same as Figure 3.8, for inner planets with periods of 30 and 50 days.

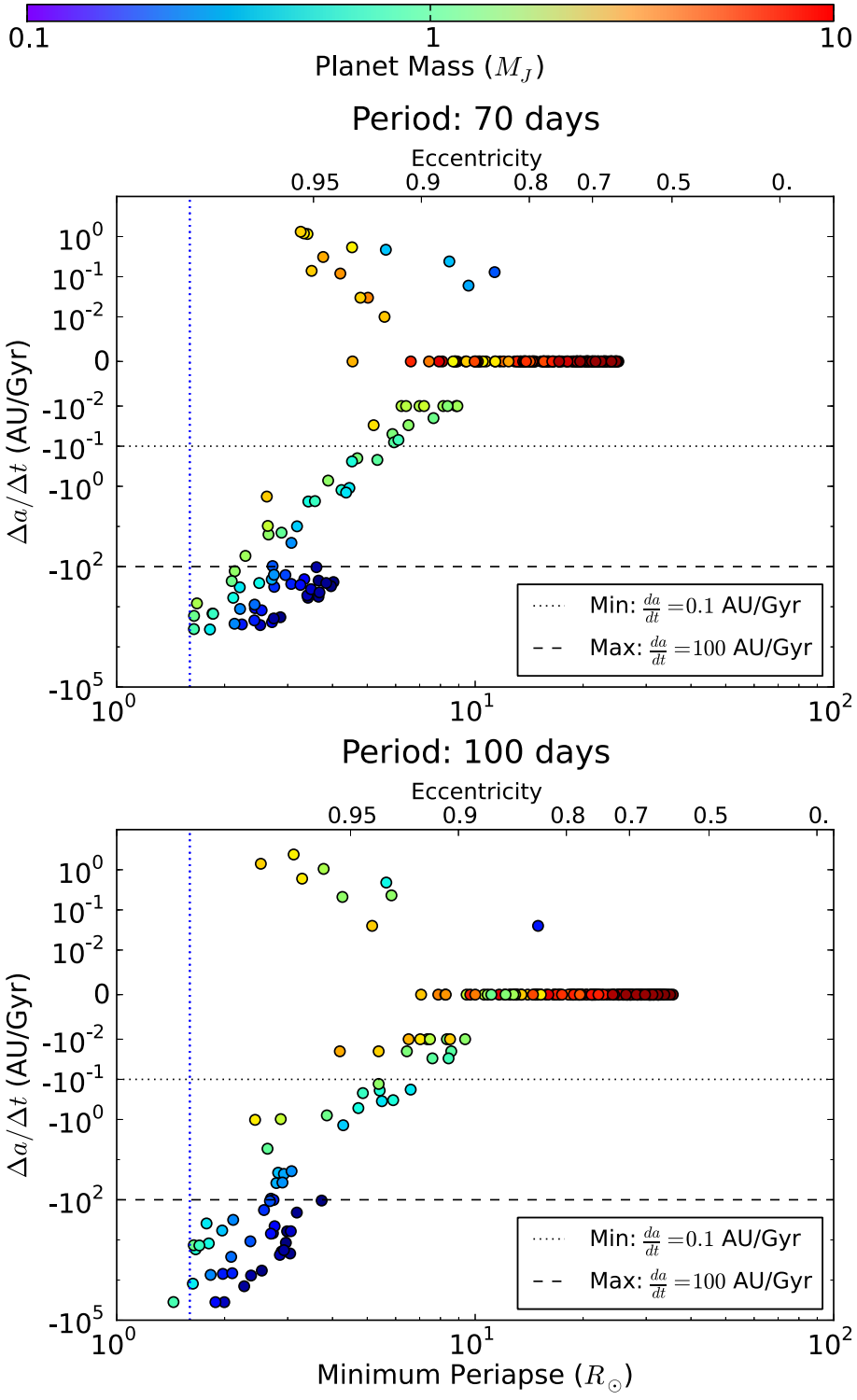

Figure 3.10 Same as Figure 3.8, for inner planets with periods of 70 and 100 days.

coefficient. We also note that none of our systems spent any time on retrograde orbits. This result is in line with the findings of Teyssandier et al. (2013), which showed that highly inclined systems are significantly poorer at causing flips in the planet. In our simulations only highly inclined systems produce large eccentricities, and as a result all stayed prograde.

3.5.2.1 Eccentricity frequency distributions

The eccentricity distributions of individual planets, along with the setup of the system, determined the magnitude of migration. Systems rapidly migrating ($da/dt > 10^2$ AU/Gyr) tended to peak more strongly at the high-eccentricity value, as seen in Figure 3.11. Systems migrating on smaller timescales ($10^{-1} - 10^2$ AU/Gyr) generally peaked near $e = 0 - 0.2$ with a smaller additional peak between 0.8 and 1.0 (Figure 3.6). Those systems not migrating generally appeared similar to the latter distributions but peaked at a lower maximum eccentricity due to our choice of initial conditions. Finally, some systems had their minimum eccentricity increase, leading to small oscillation magnitudes (Figure 3.12). In a small minority of simulations, the maximum eccentricity deviated significantly from Equation 3.11, due to the effect of octupole terms or, for short-period planets, tides.

3.5.2.2 Planetary mass effects

The relationship between mass and migration rate, with more massive planets migrating slower and less massive planets migrating rapidly, showed up in all periods (Figures 3.8 – 3.10) as a result of Equation 3.15. The strength of tides depends on planetary mass and radius, with more massive planets having stronger surface gravity and correspondingly weaker tides. Massive planets do produce larger tides in their host star, but our simulations ignored stellar tides due to their relative weakness, even with large planetary mass. As a result of keeping a constant perturber and planetary radius, small planets migrated the fastest and larger planets the slowest.

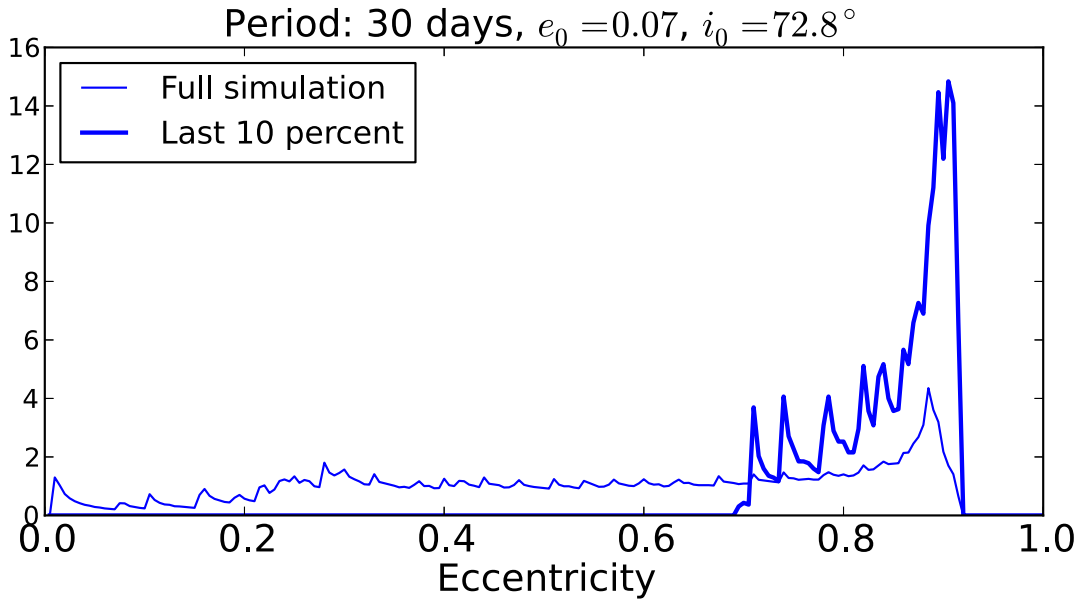

Figure 3.11 Eccentricity distribution of a rapidly migrating planet at 30 days ($da/dt = -4 \times 10^2$ AU/Gyr), illustrating that the majority of time is spent at high eccentricities during the last 10 percent of simulation time.

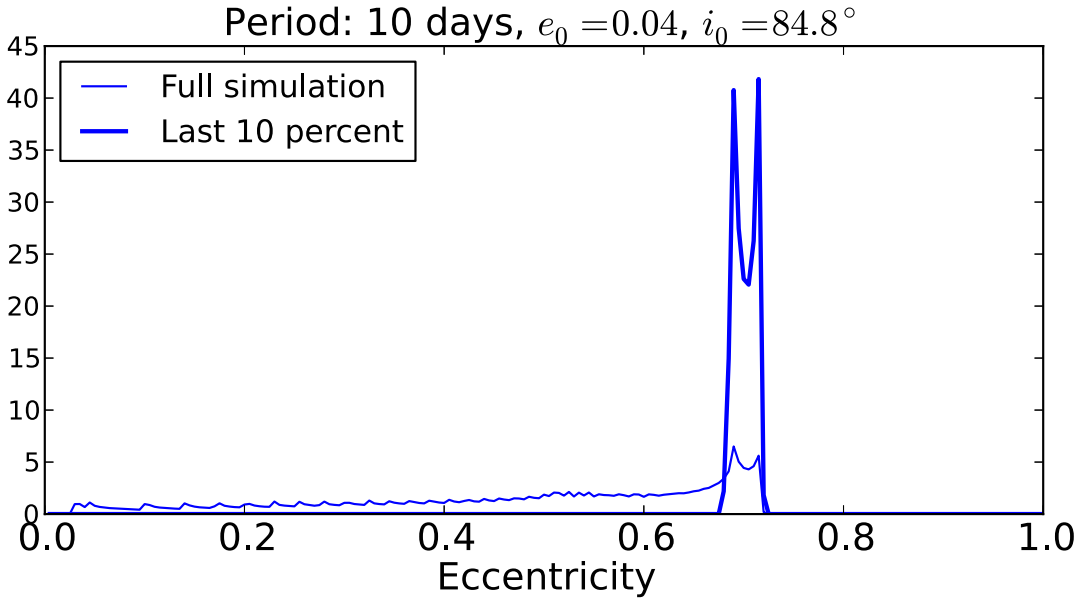

Figure 3.12 Eccentricity distribution of a planet at 10 days with damped eccentricity oscillations, where the KL timescale is roughly equal to the GR timescale.

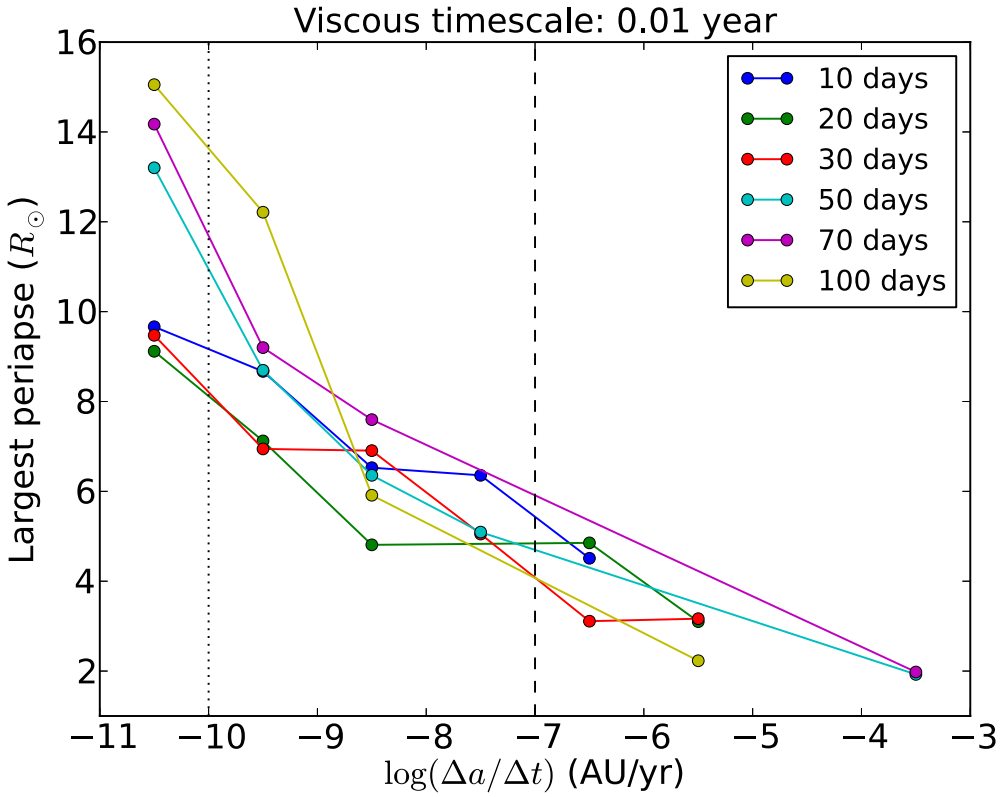

Figure 3.13 Same as Figure 3.7, but in the case of a much smaller (0.01) viscous timescale. Note the larger scale on the y-axis due to smaller maximum eccentricity at similar migration rates.

3.5.3 Other effects

3.5.3.1 Changing the viscous timescale

A viscous timescale of 0.01 year resulted in planets with higher migration rates and smaller maximum eccentricities than our primary ($t_v = 1$ year) simulations (Figure 3.13). Planets on 10-day periods did not require any eccentricity to migrate inward, and reached much smaller maximum eccentricities than other periods due to their rapid circularization. This shorter viscous timescale led to fewer planets reaching very high eccentricities, which is more similar to what is seen in observations (Figure 3.19). However, the smaller maximum eccentricities result in larger periapse distances, which results in a larger population surviving to larger stellar radii. Comparison to observations will be discussed more thoroughly in Section 3.7.

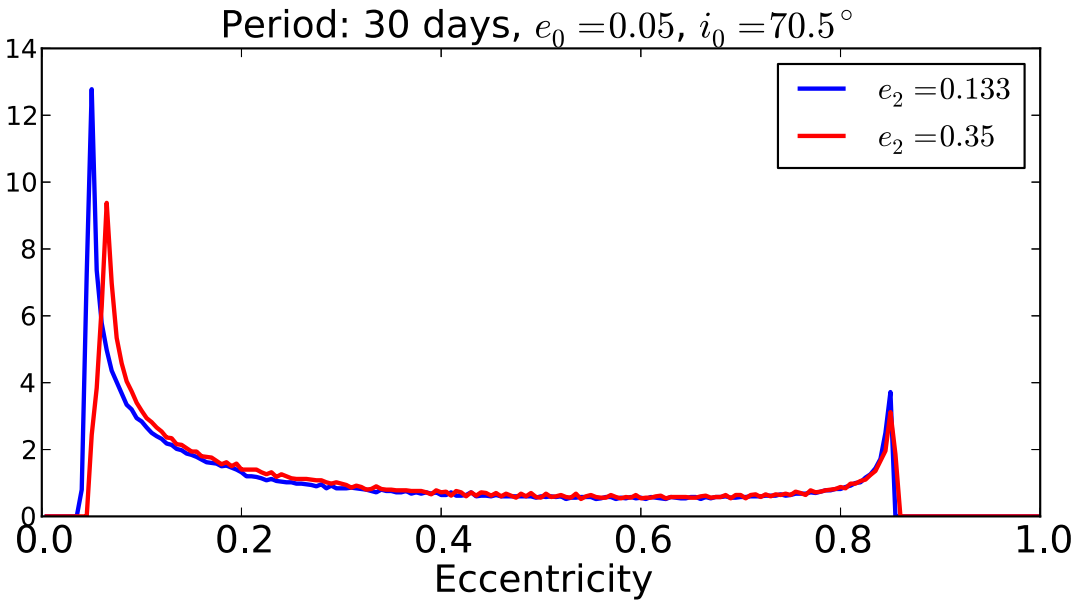

Figure 3.14 Eccentricity frequency distribution of a 30-day period planet (in arbitrary units), for both the default perturber eccentricity (0.133) and the larger value (0.35). The more eccentric perturber produces marginally higher eccentricities on average.

3.5.3.2 Changing the perturber

As described in Section 3.4.1.1, our simulations also included two smaller samples with altered perturbers for comparison. In the first of these, we increased the perturber eccentricity to near the limit of stability, 0.35, while leaving the other properties (period and mass) the same. The increase in eccentricity resulted in a small shift to larger maximum eccentricities and a resulting slight increase in the overall inward migration rate. The effect was extremely minor, as seen in Figure 3.14.

The second sample had a dramatically different perturber, one on a significantly larger orbit (10 AU = 10^4 day period), with a larger mass (30 M_J), and greater eccentricity (e_2 = 0.6380). The eccentricity value was chosen so that it was also near the limit of stability for the system. For some systems, the larger period resulted in weaker or nonexistent oscillations compared to the closer perturber. This was the case in many of short-period systems through 30 days; the larger period systems averaged more moderate migration rates. Fewer had $da/dt = 0$ than with the close in perturber, due to larger maximum eccentricities,

but fewer reached very high migration rates.

Regardless of perturber or planetary properties, significant da/dt required the planet to reach very large eccentricity values in the vast majority of those with periods longer than 10 days. Additionally, of those undergoing migration without reaching large maximum eccentricity, the majority did so due to a minimum eccentricity above 0.2, a value higher than most observed WJs.

3.5.4 Migration rates in the absence of a perturber

Those planets without a perturber behaved as expected, migrating by much larger amounts as compared to oscillating systems of equal maximum eccentricity. As shown by the lines in Figure 3.15, the migration magnitude is well fit by an analytical formula of the form

$$\frac{da}{dt} = -4 \times 10^{-4} f_e(e^2) \left(\frac{a_p}{0.1 \text{ AU}}\right)^{-8} \left(\frac{M_p}{1 M_J}\right)^{-2.4} \text{ AU/Gyr} \tag{3.17}$$

where $f_e(e^2)$ is a function of eccentricity derived from the tidal equations in the case of PS rotation (see Equation 3.29). Direct calculation of the migration rate leads to a different dependence on SMA and planetary mass (see Equation 3.31). The discrepancy is likely due to the planet rotating slightly faster in our simulations. Similar to the oscillating systems, the larger planets migrated less due to experiencing weaker tides from the star, and the larger periods required correspondingly larger eccentricities.

3.6 Stellar evolution effect

To test if KL oscillations can account for the missing WJs around evolved stars, we must determine the stellar size required to remove each of our simulated planets in the case of both oscillating and constant eccentricity. Here we focus on the planetary systems that could be observed around other stars. For this reason, we limit the migration rate to $10^{-1} - 10^2$ AU/Gyr as indicated by the lines in Figures 3.7, **??**, and 3.15. This rate is rapid enough that WJs can have entered the $10 - 100$ day-period regime in the lifetime of their star, but long

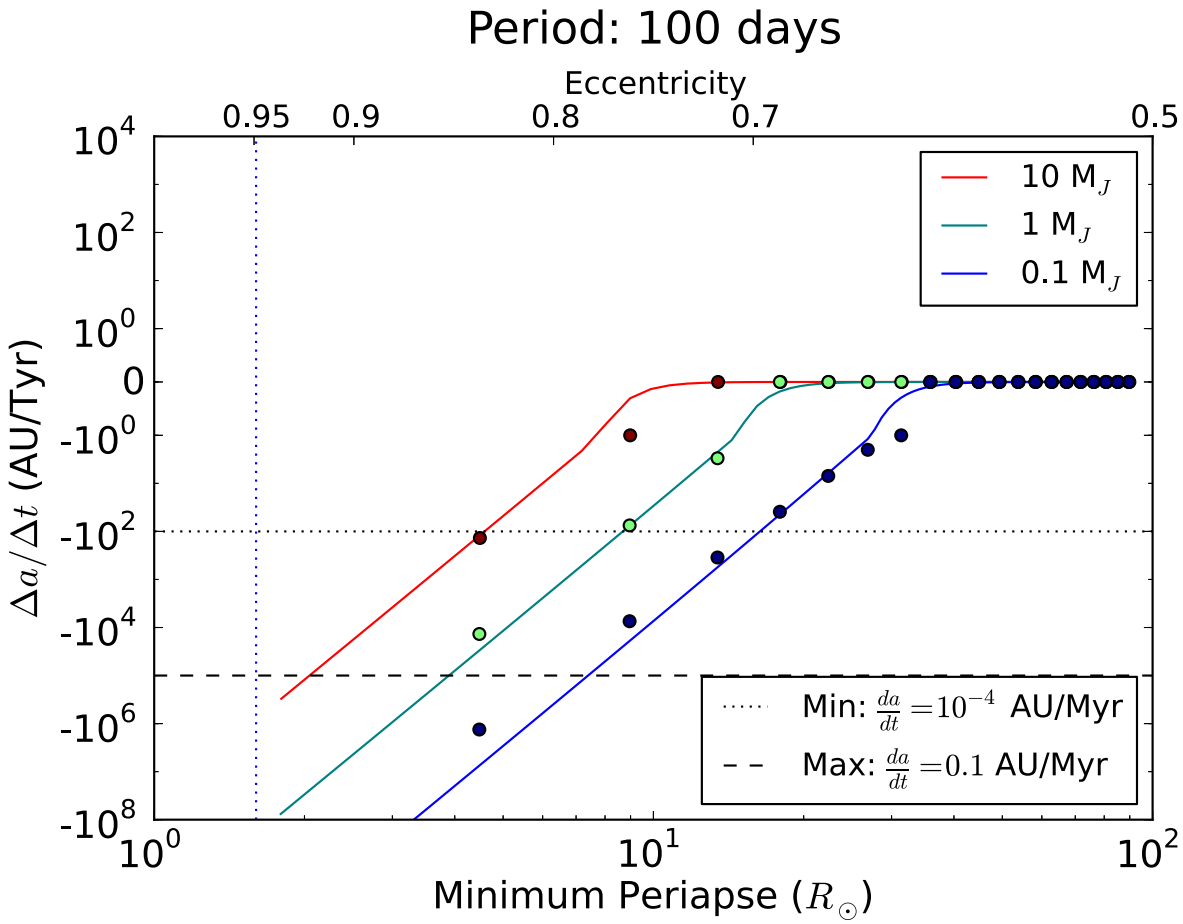

Figure 3.15 Migration rate as a function of periapse distance/eccentricity for 100-day planets without a perturber, and thus non-oscillating eccentricity. The dependence of migration rate on planetary mass and maximum eccentricity is apparent.

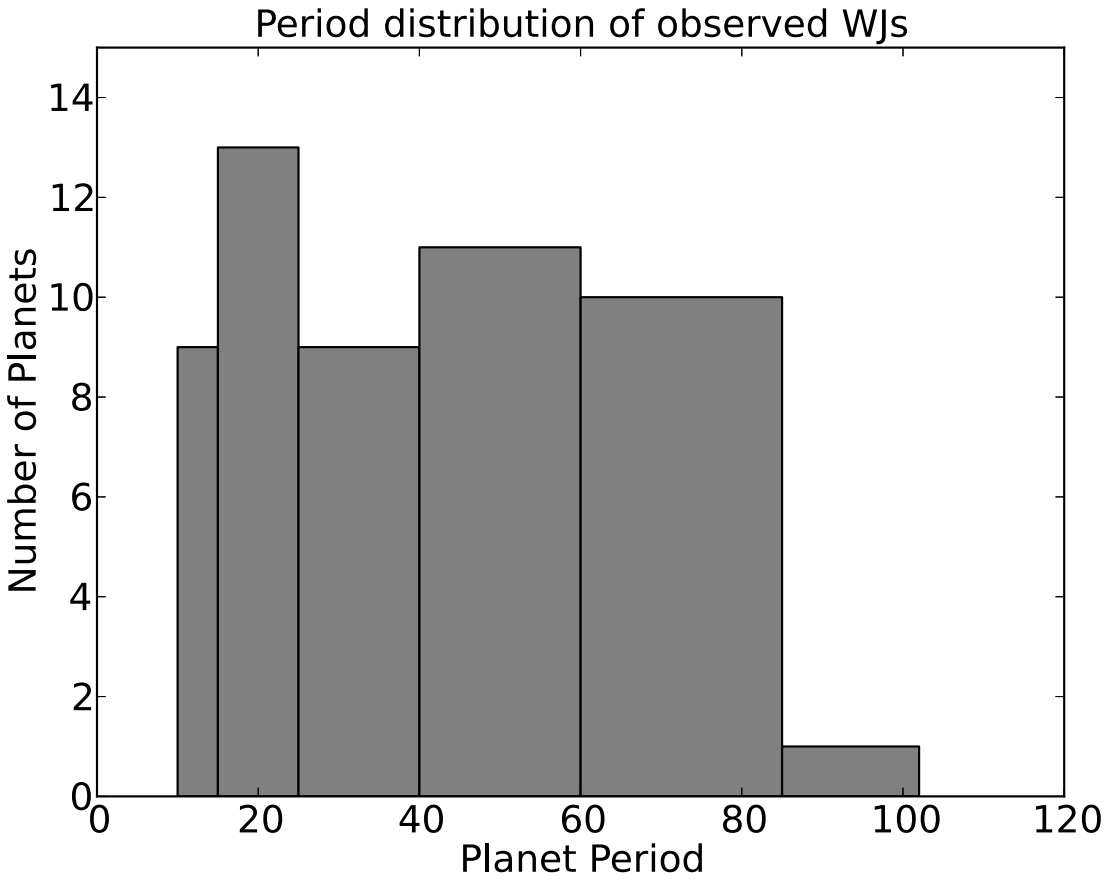

Figure 3.16 The period distribution of observed WJs, binned according to our simulation periods. This distribution informed us how many eccentricity samples to draw from each period.

enough that a significant number are observed there. Furthermore, we limit the planet mass to $0.3 - 3M_J$. This limit is to avoid being influenced both by both low-mass planets, whose large migration rates may be inaccurate due to our choice of uniform planetary radius, and massive planets, which are more likely to be affected by tides raised on the star that we did not include.

65 systems across the six orbital periods meet these criteria. We create a population of planets for comparison by drawing from the period bins according to the observed WJ distribution (Figure 3.16). With each draw from a given period, we randomly select one of the systems and a value from its eccentricity distribution. We repeat this process until we obtain

a final set of 848 planets, each with an eccentricity, period, and planet mass, which match the observed period distribution. These systems represent what the oscillating systems, or an analogous population with constant eccentricity, would look like in observations. With our population of oscillating- and constant-eccentricity planets, we then determine the criteria for removal.

3.6.1 Evolution timescale

It is only only appropriate to assume the planet is removed at its maximum eccentricity if the evolution timescale of the star ($R_*/\dot{R}_*$) is significantly longer than the KL timescale. In the case of very brief evolution timescales, the WJ eccentricity would remain relatively constant and the planets would be removed at whatever eccentricity they happened to have at that point in stellar evolution. Using MESA (Paxton et al., 2011, 2013) models, we calculated the expansion timescale of the host star to be $> 10^7$ years through $R_* = 40R_\odot$, or roughly half the size of our largest planetary orbits. The KL timescale for our simulations ranged from $7 \times 10^3 - 8 \times 10^4$ years, depending on the period of the planet, which are orders of magnitude shorter than the stellar evolution time. As a result, we safely assume the maximum eccentricity determines when the planet is removed via contact. In addition, this portion of stellar evolution occurs without any measurable change in mass, so we can safely ignore the effect of mass loss on the planetary orbits.

3.6.2 Planetary removal mechanism

A WJ can be removed in one of two ways: First, the planet can come into direct contact with the star, being disrupted as it collides with the stellar surface: $R_* = a(1 - e_{\max})$. Alternatively, the planet can migrate interior to 10 days, becoming a HJ until it is removed via direct contact. This migration occurs more quickly as the star evolves than during the main sequence because the star expands to the point where stellar tides dominate the tidal decay (Villaver et al., 2014). Once this occurs, inward migration increases dramatically with continued stellar expansion due to the R^8 dependence in the tidal friction timescale

(Equation 3.15). A planet will migrate out of the WJ period space on a timescale of roughly $P_T = -a/(da/dt)$.

The value of da/dt caused by tides in the planet, paired with some assumptions about stellar and planetary tides, allow us to quantify the increase in migration rate due to stellar expansion. We take the contribution from the star to be

$$P_T = \frac{P_{T_p}}{1 + (R_*/R_{*,eq})^8} \tag{3.18}$$

where P_{T_p} is the migration timescale before stellar evolution (due only to planetary tides) and $R_{*,eq}$ is the size of the star at which stellar tides match planetary tides. The value of P_{T_p} for oscillating systems comes from our simulation results, while P_{T_p} for constant eccentricity systems comes from Equation 3.17. Importantly, $f(0) = 10^{-3}$ in Equation 3.17, so that even planets on circular orbits are migrating slowly inward.

To determine the value of $R_{*,eq}$, we set the tidal timescales of the star equal to that of the planet times a coefficient, which accounts for the different spins between the two: $t_{\mathrm{F}_*} = f_s t_{\mathrm{F}_p}$. We assume viscous timescales of $t_{\mathrm{V}_*} = 50$ years based the planet-to-star strength from Hansen (2010), and $f_s = 0.2$ based on calculations of $f(e^2, \Omega)$, our function $f(e^2)$ with a non-PS spin value.

$$R_{*,eq} = R_p \left(f_s \frac{t_{\mathrm{V}_*}}{t_{\mathrm{V}_p}} \right)^{1/8} \left(\frac{M_*}{M_p} \right)^{3/8} \tag{3.19}$$

We note that this equation assumes the viscous timescale for the star stays constant over stellar evolution, which is not strictly true. However, the very weak dependence on t_{V_*} means it should not have a significant effect. Using the calculation from Zahn (1977), $t_{\mathrm{V}_*} \propto (L/R^2)^{-4/3} \propto T_{\mathrm{eff}}^{-4/3}$. For our stellar model, the surface temperature drops from 6300K to 3200K as the star grows to $50 R_\odot$, corresponding to an increase in viscous timescale by a factor of 2.5, or a 12% increase in $R_{*,eq}$ at its largest.

We consider a planet with a migration timescale $P_T < P_{\mathrm{short}} = 10^6$ years to be removed, due to the comparatively brief period of stellar evolution relative to the main sequence

e	$a(1-e)$ ($R_\odot$)	da/dt (AU/yr)	$R_{\rm rem}$ ($R_\odot$)
$0.07-0.93$	$53-4.0$	-3.0e-9	4.0
0.11	50	-5.4e-17	38
0.22	44	-1.4e-16	33
0.25	42	-1.9e-16	32
0.46	30	-4.2e-15	22
0.15	48	-7.0e-17	37
0.67	19	-3.6e-13	13
0.25	42	-2.0e-16	32
0.56	25	-2.4e-14	18
0.91	5.0	-4.1e-8	2.9
0.46	30	-4.1e-15	22

Table 3.1 Migration values and stellar size at planetary engulfment ($R_{\rm rem}$) for a simulated oscillating planet and 10 constant-eccentricity realisations. The da/dt values for the latter group were calculated using Equation 3.17.

lifetime. Rearranging Equation 3.18, we can solve for $R_{\rm short}$ as a function of migration timescales and $R_{*,eq}$:

$$R_{\rm short} = R_{*,eq}\left(\frac{P_{T_p}}{P_{\rm rem}} - 1\right)^{1/8} \tag{3.20}$$

Therefore we define a planet to be removed when the size of the star reaches $R_{\rm rem}$, the smaller of $a(1-e_{\rm max})$ and $R_{\rm short}$.

3.6.3 Stellar expansion results

As an example, we draw 10 random samples from the eccentricity distribution of our case study (Figure 3.6) and calculate the size of the star when the planet is removed assuming the eccentricity is constant. Table 3.1 lists these values along with the periapsides and migration rate. The oscillating eccentricity is listed for comparison, showing that only in that case is the planet removed via collision; the constant-eccentricity planets are all removed via migration out of the WJ region, caused by stellar tides.

We perform the same analysis on all eligible systems, scaling the contribution from systems of each period according to the observed period distribution. Our results are shown

in Figure 3.17: the oscillating population drops off as soon as the star exceeds $3R_\odot$, removing all but a handful of planets by $5R_\odot$. By requiring these planets to have a measurable migration rate ($10^{-1} - 10^2$ AU/Gyr), we required them to have small periapsides as well. As a result, those systems are removed almost exclusively by collision with the star. The constant-eccentricity population drops off much more slowly, with some planets surviving until the star is over $50R_\odot$. A small fraction of these planets are on very eccentric orbits due to the oscillating systems reaching large maximum eccentricities. As a result, those planets are removed by collision with the star. In general, however, most had low or moderate eccentricity (as seen in Figure 3.18) and are removed when the star dominates their migration rate. We note that varying t_{V*} does have an effect for those systems, but only serves to shift the constant-eccentricity population to stellar sizes larger by a factor of $2 - 3$.

The discrete periods of our simulations are identifiable in the constant eccentricity population as small, steep drops at specific stellar radii. This effect results from the minimum da/dt at a given period: all low-eccentricity planets of a given period have similar da/dt values and are removed at similar stellar radii. When the minimum migration rate is removed, the bumps are smoothed out. The 100-day population between 50 and 60 $R_\odot$ is negligible, due to the small number of such planets in the observed WJ period distribution.

3.7 Comparison to observations

The model described here is motivated by the claimed deficit of WJs around moderately evolved stars (Johnson et al., 2007, 2011), as seen in Figure 3.1 and Section 3.2. We postulate that the reason for this deficit is that the observed eccentricity distribution of WJs around main sequence stars is really a snapshot of a population whose eccentricities are oscillating via the KL mechanism while they migrate inwards due to tidal friction. The fact that the oscillation timescale is short compared to the characteristic timescale for the stellar evolution means that planets are removed from the observed sample when their periapsides oscillate to the minimum value and interact with the host star. Figure 15 shows the result of such a model and demonstrates that, under these conditions, a pre-existing WJ population will

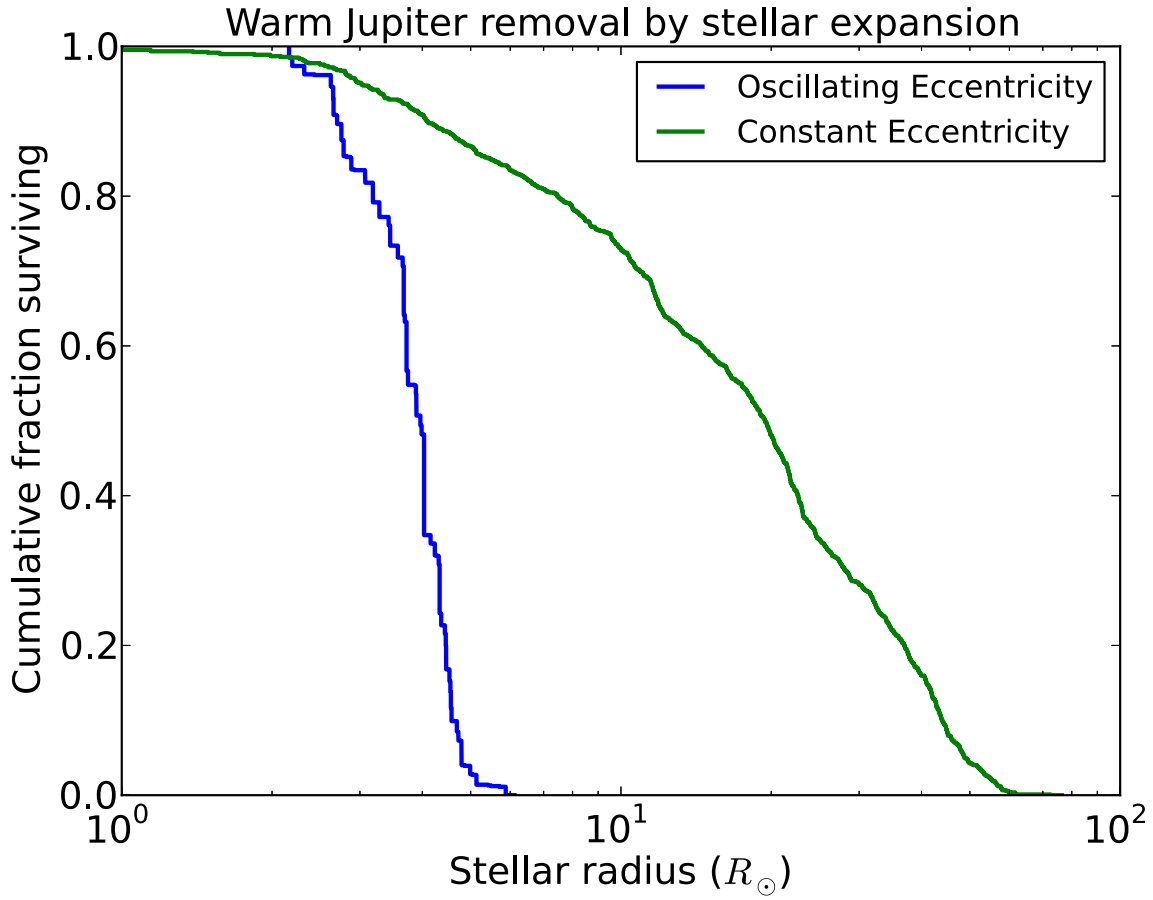

Figure 3.17 The fraction of oscillating and constant-eccentricity WJs that survive as a function of stellar radius. While the fraction of oscillating planets drops off dramatically above $3R_\odot$, the fraction with constant eccentricity is significant even as the stellar radius exceeds $20R_\odot$, which indicates that the lack of WJs around evolved stars can be effectively explained by eccentricity oscillations.

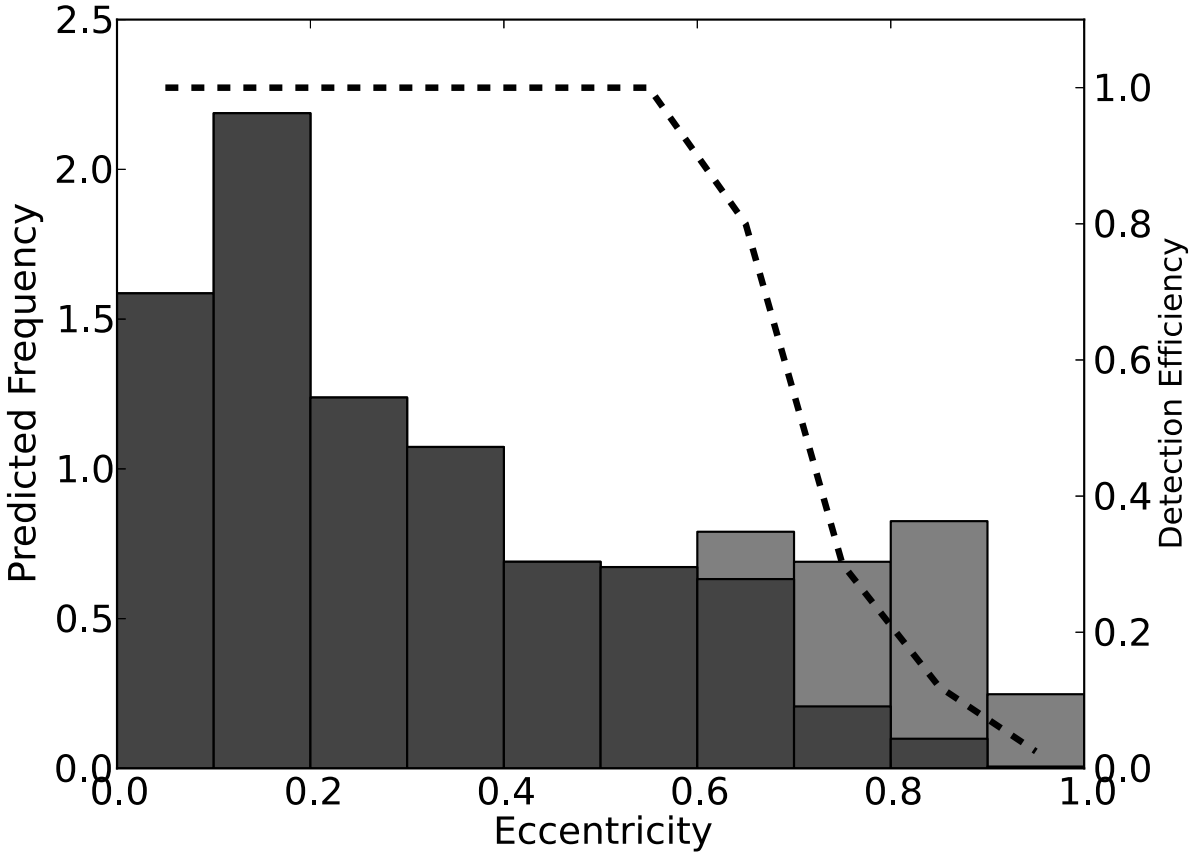

Figure 3.18 The distribution of eccentricity values drawn from our simulated oscillating systems, with the same period distribution as observed (grey). The detection efficiency of 100-day planets with signal-to-noise of 10 (dashed line), obtained from Cumming (2004), drops off dramatically at high eccentricities and produces the eccentricity distribution predicted in observations (dark grey).

be largely removed by the time the stars evolve to 4 $R_{\odot}$, in contrast to the case where the eccentricities of the observed population do not oscillate. The exact location of WJ removal depends on the details of tidal forces and the perturber, but the general behavior is well described by Figure 3.17.

However, our results do not match all observations. Figures 3.18 and 3.19 show the distribution of eccentricities for our simulated systems and observed WJs (from the Exoplanet Orbit Database), respectively, with our simulated population drawn from the same period distribution. In both cases the systems are restricted to the Jupiter mass range (0.3-3)

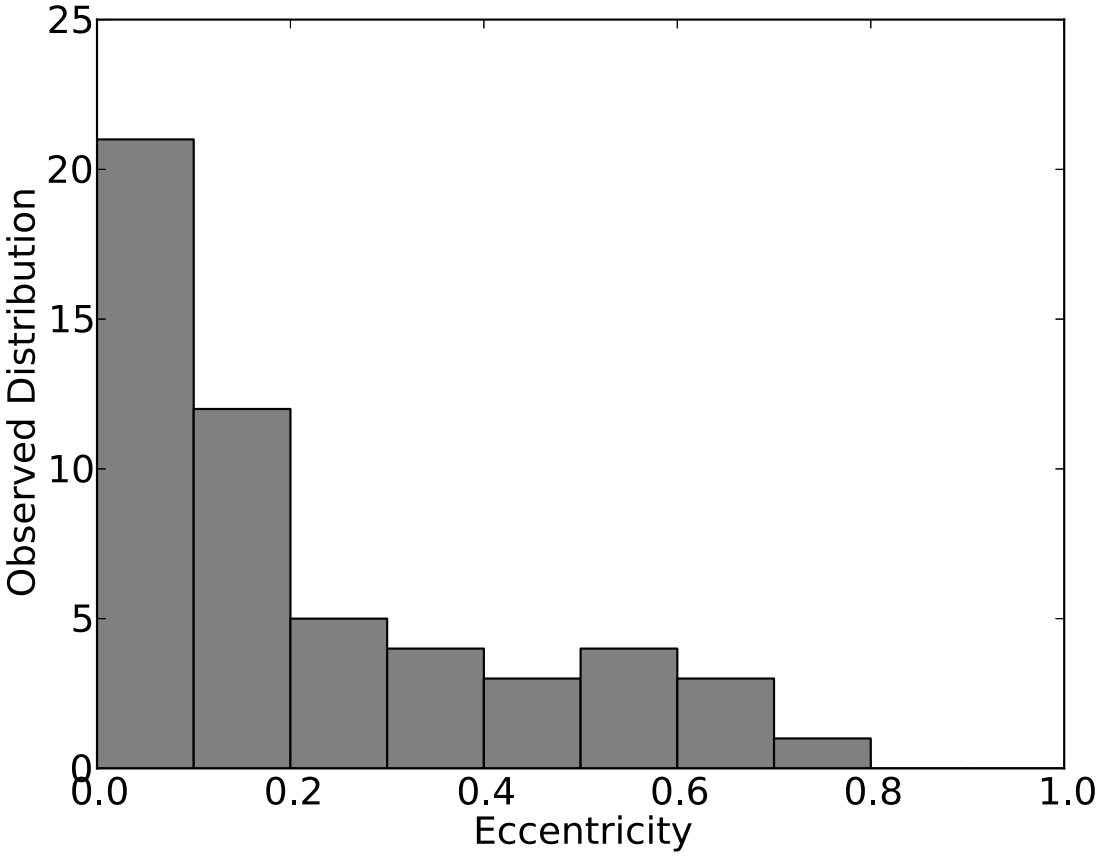

Figure 3.19 The eccentricity distribution for observed WJs, taken from the Exoplanet Orbit Database. The small number of highly eccentric planets differs significantly from the oscillating distribution, but that may be a result of low detection efficiency..

and the period range of $10 - 100$ days. Comparison of these two populations using the Kolmogorov–Smirnov (KS) test gives a p-value of 1×10^{-4}, indicating they are unlikely to be drawn from the same underlying population. The discrepancy is primarily due to the significant fraction (15%) of simulated WJs with high eccentricity ($e > 0.8$), while no observed WJs have such high values. The lack of high-eccentricity WJs has also been noted by Dawson et al. (2015).

The observed population also includes an excess number of low-eccentricity planets, which is difficult to reconcile with the orbital behavior of our planets. Many of the simulated planets, even those started with eccentricity of 0.05, had a minimum eccentricity peak above 0.1, similar to the eccentricity distribution shown in Figure 3.6. This figure also shows the cumulative distribution of eccentricity values; blue, green, and red dashed lines indicate the cumulative observed distribution at 75, 90, and 98 percent of WJs, respectively, for the simulated planet (dotted lines) and eccentricity distribution of all observed WJs (dashed lines). While tidal effects can cause circularisation, the accompanying orbital decay produces HJs, not WJs, on circular orbits.

3.7.1 Observational biases

One of the two major discrepancies between the eccentricity distribution of our simulated population and that of observed WJs lies at the highest eccentricities. In order for host stars to remove their orbiting WJs early on in stellar evolution, as observations imply, the minimum periapsides must be quite small. As a result planets must undergo KL oscillations to large eccentricities, leading to a small but significant fraction of WJs inhabiting that portion of the eccentricity distribution at any given time. Even oscillating systems peaking strongly near $e = 0$ have a significant tail at high eccentricities, in conflict with observations.

However, if eccentric planets are more difficult to detect than low-eccentricity or circular planets, then the dearth of high-eccentricity systems could be an observational effect, not a physical one. Studies of exoplanet detectability in radial velocity surveys (Cumming, 2004; O'Toole et al., 2009) have shown that that appears to be the case above eccentricities ~ 0.5,

where the largest difference between observed and simulated populations exists. To test how much this effect can improve the fit between our results and observations, we apply the detection efficiency (DE) of Figure 4 in Cumming (2004) to our eccentricity distribution. We use the DE found for fitting to a Lomb-Scargle periodogram with $N = 39$ observations short-period (100 day) planets, with a signal-to-noise ratio of 10, shown in Figure 3.18. After application, the KS test gives a p-value of 4×10^{-4}, somewhat improved compared to the distribution without correcting for DE. Including an additional 10 percent of the population in circular planets leads to a p-value of 0.03, indication a population primarily oscillating is consistent with observations. A population of circular WJs this small would not have a high probability of being detected around evolved stars even if they existed, and could have originated via an alternative migration mechanism, such as disk migration.

Given the specificity of this detection efficiency function and the inclusion of a separate, distinct population, we do not claim that this calculation proves that our population matches that of observations. An in-depth examination of the detection efficiency of WJs around evolved stars is outside the scope of our work. However, this calculation does show that the difference in eccentricity distributions may not be as insurmountable as would appear from direct comparison. As more eccentricities are determined in systems detected via the transit method, these biases may be reduced, allowing us a better view of the underlying eccentricity distribution. We finish by noting that our DE-corrected distribution predicts that ~ 1 percent of observed WJs should have eccentricities greater than 0.8. Given that there are currently only 63 WJs listed in the Exoplanet Orbit Database, it is unsurprising that none has high eccentricity. As the number of confirmed WJs increases and improved methods of analyzing data are implemented (see O'Toole et al. 2009), the high eccentricity population, if it exists, should become apparent.

3.7.2 Assumptions of physical effects

Our simulations ignored the effect of stellar tides, which were only included in the evolved star calculations. Larger stellar tides would increase the tidal decay for a planet with a smaller

maximum eccentricity and strengthen that decay as the star evolved. However, limits can be placed on the strength of tides in stars from the population of WJs (Hansen, 2012). Stellar tides must be weak enough that planets can exist on orbits shorter than one day for an observationally significant amount of time. For that reason, it is unlikely that stellar tides can dominate the evolution of most planets except for the most massive ones. As a test, we simulated 32 systems at 50 days with identical properties to our primary simulations, but with the stellar tidal timescale set to 50 years. The simulations were qualitatively identical to those without stellar tides, indicating they would need to be significantly stronger than the current limits in order to account for the lack of observed eccentric WJs.

Our simulations also assumed the equilibrium model for tides, which is an approximation. Tidal effects may differ significantly, both in the star and in the planet, when they are forced on an eccentric orbit. The existence of HJs would not constrain such effects due to their uniformly near-circular orbits. Additionally, we ignored the size difference between 1 M_J planets and 0.1 M_J planets. Correcting for this would likely reduce the migration rate for low-mass planets, leading to a larger population in our defined migrating region. However, many WJs are Jupiter-mass and above, and the issue of a large periapse preventing prompt removal remains.

3.8 Conclusion

A number of planets have been found around evolved stars, but there appears to be a lack of massive planets interior to 0.6 AU (Johnson et al., 2007; Bowler et al., 2010; Johnson et al., 2011). Two possibilities exist: either the underlying population of planets differs around the unevolved progenitors of these generally more massive ($> 1.5 M_{\odot}$) stars, or stellar evolution has led to their removal. The results of Lloyd (2011, 2013) have called into question whether the evolved stars truly originate from a more massive population, supporting the latter reason for the absence of WJs. Additionally, Schlaufman & Winn (2013) showed that some evolved stars have a different population of planets than their unevolved progenitors of the same mass, indicating that stellar evolution is a cause in at least some cases. Most recently,

Johnson et al. (2014) showed that at least one evolved star in the disputed population has a mass truly greater than 1.5 $M_{\odot}$, as they claimed in prior works. Taken together, these results leave considerable ambiguity as to the explanation of missing WJs.

Here we have simulated planets undergoing KL oscillations as part of their migration inward and examined how the population decays with stellar evolution. By using a model population of WJs and their perturbing companions, we have shown that KL oscillating WJs explain the observed absence around evolved stars better than a constant-eccentricity population. A population of migrating, KL oscillating WJs is almost entirely removed around an evolving star by the time it reaches $5R_{\odot}$, while an observationally identical population with constant eccentricity survives stellar expansion beyond $40R_{\odot}$. Finally, although we have adopted a stellar mass of 1.2 $M_{\odot}$ in our simulations, it should be noted that the rapid removal of WJs migrating via KL oscillations is applicable regardless of stellar mass. Therefore the absence observed by Johnson et al. (2007) and related works need not indicate that WJs are absent around more massive stars in general.

3.9 APPENDIX: Planetary migration during pseudo-synchronous rotation

The orbital evolution of a planet due to tides is given by

$$\frac{da/dt}{a} = -2\left[W_p + W_* + \frac{e^2}{1-e^2}(V_p + V_*)\right] \tag{3.21}$$

where the subscripts p and $*$ correspond to the planet and host star, respectively. V and W are given in Eggleton & Kiseleva-Eggleton (2001):

$$V = \frac{9}{t_F}\left[\frac{1+(15/4)e^2+(15/8)e^4+(5/64)e^6}{(1-e^2)^{13/2}} - \frac{11\Omega}{18n}\frac{1+(3/2)e^2+(1/8)e^4}{(1-e^2)^5}\right] \tag{3.22}$$

$$W = \frac{1}{t_F}\left[\frac{1+(15/2)e^2+(45/8)e^4+(5/16)e^6}{(1-e^2)^{13/2}} - \frac{\Omega}{n}\frac{1+3e^2+(3/8)e^4}{(1-e^2)^5}\right] \tag{3.23}$$

where n is the mean motion of the orbit and Ω is the rotation rate of the body. A migrating WJ will have already reached pseudo-synchronous rotation, which occurs when $W_p = 0$ (Hut, 1981). The rotation rate in that case is given by

$$\frac{\Omega_{ps}}{n} = \frac{1 + (15/2)e^2 + (45/8)e^4 + (5/16)e^6}{(1 + 3e^2 + (3/8)e^4)(1 - e^2)^{3/2)}} \tag{3.24}$$

Plugging in Ω_{ps}, we get the strength of tides for a pseudo-synchronous planet:

$$V_p(\Omega_{ps}) = \frac{9}{t_{Fp}} \left[\frac{1792 + 5760e^2 + 14336e^4 + 5480e^6 + 1020e^8 + 25e^{10}}{4608(1 - e^2)^{15/2}} \right] \tag{3.25}$$

Assuming planetary tides dominate during the main sequence ($V_p >> V_*$) and that the planet is in PS rotation ($W_p = 0$), we can simplify the tidal decay equation:

$$\frac{da/dt}{a} = -2 \left[W_* + \frac{e^2}{1 - e^2}(V_p) \right] \tag{3.26}$$

$$= -2 \left[W_* + \frac{e^2}{1 - e^2} \frac{9}{t_{Fp}} \left(\frac{1792 + 5760e^2 + 14336e^4 + 5480e^6 + 1020e^8 + 25e^{10}}{4608(1 - e^2)^{15/2}} \right) \right] \tag{3.27}$$

$$= -\frac{2 f_e(e^2)}{t_{Fp}} \tag{3.28}$$

where

$$f_e(e^2) = t_{Fp} W_* + \left(\frac{1792e^2 + 5760e^4 + 14336e^6 + 5480e^8 + 1020e^{10} + 25e^{12}}{512(1 - e^2)^{17/2}} \right) \tag{3.29}$$

We have retained W_* because it tends to t_{F*}^{-1} as $e \to 0$, assuming the star is rotating slowly, while the remainder of the expression tends to 0. The limits for $f_e(e^2)$ are therefore t_{Fp}/t_{F*} near $e = 0$ and $3.5(1 - e^2)^{17/2}$ for $e \sim 1$. From the definition of t_F, Equation 3.15:

$$\frac{t_{Fp}}{t_{F*}} = \frac{t_{Vp}}{t_{V*}} \left(\frac{R_p}{R_*} \right)^{-8} \left(\frac{M_p}{M_*} \right)^{3} \left(\frac{1 + 2k_p}{1 + 2k_*} \right)^{-2} \tag{3.30}$$

In Section 3.3.3.1 we assume the following values for the planetary systems: $t_{Vp} = 1$ year, $t_{V*} = 50$ years, $M_* = 1.2 M_\odot$, $M_p = 0.1 - 10 M_J$, $k_p = 0.25$, and $k_* = 0.014$. Entering these

values, we we get a ratio ranging from $10^{-6} - 1$. For the subset in Sections 3.6 and 3.7, $0.3 - 3M_J$, the values range from $2.7 \times 10^{-5} - 2.6 \times 10^{-2}$. We assume $t_{Fp}/t_{F*} = 10^{-3}$ in all cases for simplicity, and note that it is a small correction in all cases.

Plugging in for t_{Fp} using Equation 3.15, we get the expected value for tidal migration:

$$\frac{da}{dt} = -18 f_e(e^2) \frac{a}{t_{Vp}} \left(\frac{R_p}{a}\right)^8 \left(\frac{M_*}{M_p}\right)^2 \frac{1}{(1+2k_p)^2} \tag{3.31}$$

Bibliography

Albrecht, S., Winn, J. N., Johnson, J. A., Howard, A. W., Marcy, G. W., Butler, R. P., Arriagada, P., Crane, J. D., Shectman, S. A., Thompson, I. B., Hirano, T., Bakos, G., & Hartman, J. D. 2012, ApJ, 757, 18

Batalha, N. M., Rowe, J. F., Bryson, S. T., Barclay, T., Burke, C. J., Caldwell, D. A., Christiansen, J. L., Mullally, F., Thompson, S. E., Brown, T. M., Dupree, A. K., Fabrycky, D. C., Ford, E. B., Fortney, J. J., Gilliland, R. L., Isaacson, H., Latham, D. W., Marcy, G. W., Quinn, S. N., Ragozzine, D., Shporer, A., Borucki, W. J., Ciardi, D. R., Gautier, III, T. N., Haas, M. R., Jenkins, J. M., Koch, D. G., Lissauer, J. J., Rapin, W., Basri, G. S., Boss, A. P., Buchhave, L. A., Carter, J. A., Charbonneau, D., Christensen-Dalsgaard, J., Clarke, B. D., Cochran, W. D., Demory, B.-O., Desert, J.-M., Devore, E., Doyle, L. R., Esquerdo, G. A., Everett, M., Fressin, F., Geary, J. C., Girouard, F. R., Gould, A., Hall, J. R., Holman, M. J., Howard, A. W., Howell, S. B., Ibrahim, K. A., Kinemuchi, K., Kjeldsen, H., Klaus, T. C., Li, J., Lucas, P. W., Meibom, S., Morris, R. L., Prša, A., Quintana, E., Sanderfer, D. T., Sasselov, D., Seader, S. E., Smith, J. C., Steffen, J. H., Still, M., Stumpe, M. C., Tarter, J. C., Tenenbaum, P., Torres, G., Twicken, J. D., Uddin, K., Van Cleve, J., Walkowicz, L., & Welsh, W. F. 2013, ApJS, 204, 24

Bennett, D. P., Rhie, S. H., Nikolaev, S., Gaudi, B. S., Udalski, A., Gould, A., Christie, G. W., Maoz, D., Dong, S., McCormick, J., Szymański, M. K., Tristram, P. J., Macintosh, B., Cook, K. H., Kubiak, M., Pietrzyński, G., Soszyński, I., Szewczyk, O., Ulaczyk, K., Wyrzykowski, Ł., OGLE Collaboration, DePoy, D. L., Han, C., Kaspi, S., Lee, C.-U., Mallia, F., Natusch, T., Park, B.-G., Pogge, R. W., Polishook, D., μFUN Collaboration, Abe, F., Bond, I. A., Botzler, C. S., Fukui, A., Hearnshaw, J. B., Itow, Y., Kamiya, K., Korpela, A. V., Kilmartin, P. M., Lin, W., Ling, J., Masuda, K., Matsubara, Y., Motomura, M., Muraki, Y., Nakamura, S., Okumura, T., Ohnishi, K., Perrott, Y. C., Rattenbury, N. J., Sako, T., Saito, T., Sato, S., Skuljan, L., Sullivan, D. J., Sumi, T., Sweatman, W. L., Yock, P. C. M., MOA Collaboration, Albrow, M., Allan, A., Beaulieu,

J.-P., Bramich, D. M., Burgdorf, M. J., Coutures, C., Dominik, M., Dieters, S., Fouqué, P., Greenhill, J., Horne, K., Snodgrass, C., Steele, I., Tsapras, Y., PLANET, F. t., RoboNet Collaborations, Chaboyer, B., Crocker, A., & Frank, S. 2010, ApJ, 713, 837

Bodenheimer, P., Hubickyj, O., & Lissauer, J. J. 2000, Icarus, 143, 2

Bonsor, A., Mustill, A. J., & Wyatt, M. C. 2011, MNRAS, 414, 930

Bonsor, A. & Wyatt, M. C. 2012, MNRAS, 420, 2990

Bottke, Jr., W. F., Rubincam, D. P., & Burns, J. A. 2000, Icarus, 145, 301

Bottke, Jr., W. F., Vokrouhlický, D., Rubincam, D. P., & Nesvorný, D. 2006, Annual Review of Earth and Planetary Sciences, 34, 157

Bowler, B. P., Johnson, J. A., Marcy, G. W., Henry, G. W., Peek, K. M. G., Fischer, D. A., Clubb, K. I., Liu, M. C., Reffert, S., Schwab, C., & Lowe, T. B. 2010, ApJ, 709, 396

Butler, R. P., Marcy, G. W., Williams, E., Hauser, H., & Shirts, P. 1997, ApJL, 474, L115

Butler, R. P., Wright, J. T., Marcy, G. W., Fischer, D. A., Vogt, S. S., Tinney, C. G., Jones, H. R. A., Carter, B. D., Johnson, J. A., McCarthy, C., & Penny, A. J. 2006, ApJ, 646, 505

Chambers, J. E. 1999, MNRAS, 304, 793

Chary, R., Zuckerman, B., & Becklin, E. E. 1999, in ESA Special Publication, Vol. 427, The Universe as Seen by ISO, ed. P. Cox & M. Kessler, 289

Chirikov, B. V. 1979, Phys. Rep., 52, 263

Cumming, A. 2004, MNRAS, 354, 1165

Darwin, G. H. 1880, Royal Society of London Philosophical Transactions Series I, 171, 713

Dawson, R. I., Murray-Clay, R. A., & Johnson, J. A. 2015, ApJ, 798, 66

Debes, J. H. & Sigurdsson, S. 2002, ApJ, 572, 556

Debes, J. H., Walsh, K. J., & Stark, C. 2012, ApJ, 747, 148

Dong, R., Wang, Y., Lin, D. N. C., & Liu, X.-W. 2010, ApJ, 715, 1036

Dong, S., Katz, B., & Socrates, A. 2014, ApJL, 781, L5

Duncan, M., Quinn, T., & Tremaine, S. 1989, Icarus, 82, 402

Eggleton, P. P., Kiseleva, L. G., & Hut, P. 1998, ApJ, 499, 853

Eggleton, P. P. & Kiseleva-Eggleton, L. 2001, ApJ, 562, 1012

Fabrycky, D. & Tremaine, S. 2007, ApJ, 669, 1298

Faedi, F., West, R. G., Burleigh, M. R., Goad, M. R., & Hebb, L. 2011, MNRAS, 410, 899

Fang, J. & Margot, J.-L. 2012, AJ, 143, 59

Farihi, J., Barstow, M. A., Redfield, S., Dufour, P., & Hambly, N. C. 2010a, MNRAS, 404, 2123

Farihi, J., Jura, M., Lee, J.-E., & Zuckerman, B. 2010b, ApJ, 714, 1386

Farihi, J., Jura, M., & Zuckerman, B. 2009, ApJ, 694, 805

Farinella, P., Vokrouhlicky, D., & Hartmann, W. K. 1998, Icarus, 132, 378

Frewen, S. F. N. & Hansen, B. M. S. 2014, MNRAS, 439, 2442

Gaudi, B. S., Bennett, D. P., Udalski, A., Gould, A., Christie, G. W., Maoz, D., Dong, S., McCormick, J., Szymański, M. K., Tristram, P. J., Nikolaev, S., Paczyński, B., Kubiak, M., Pietrzyński, G., Soszyński, I., Szewczyk, O., Ulaczyk, K., Wyrzykowski, Ł., OGLE Collaboration, DePoy, D. L., Han, C., Kaspi, S., Lee, C.-U., Mallia, F., Natusch, T., Pogge, R. W., Park, B.-G., μ-Fun Collabortion, Abe, F., Bond, I. A., Botzler, C. S., Fukui, A., Hearnshaw, J. B., Itow, Y., Kamiya, K., Korpela, A. V., Kilmartin, P. M., Lin, W., Masuda, K., Matsubara, Y., Motomura, M., Muraki, Y., Nakamura, S., Okumura, T., Ohnishi, K., Rattenbury, N. J., Sako, T., Saito, T., Sato, S., Skuljan, L., Sullivan, D. J.,

Sumi, T., Sweatman, W. L., Yock, P. C. M., MOA Collaboration, Albrow, M. D., Allan, A., Beaulieu, J.-P., Burgdorf, M. J., Cook, K. H., Coutures, C., Dominik, M., Dieters, S., Fouqué, P., Greenhill, J., Horne, K., Steele, I., Tsapras, Y., Planet Collaboration, RoboNet Collaborations, Chaboyer, B., Crocker, A., Frank, S., & Macintosh, B. 2008, Science, 319, 927

Gould, A., Udalski, A., An, D., Bennett, D. P., Zhou, A.-Y., Dong, S., Rattenbury, N. J., Gaudi, B. S., Yock, P. C. M., Bond, I. A., Christie, G. W., Horne, K., Anderson, J., Stanek, K. Z., DePoy, D. L., Han, C., McCormick, J., Park, B.-G., Pogge, R. W., Poindexter, S. D., Soszyński, I., Szymański, M. K., Kubiak, M., Pietrzyński, G., Szewczyk, O., Wyrzykowski, Ł., Ulaczyk, K., Paczyński, B., Bramich, D. M., Snodgrass, C., Steele, I. A., Burgdorf, M. J., Bode, M. F., Botzler, C. S., Mao, S., & Swaving, S. C. 2006, ApJL, 644, L37

Hansen, B. M. S. 2010, ApJ, 723, 285

—. 2012, ApJ, 757, 6

Hébrard, G., Bouchy, F., Pont, F., Loeillet, B., Rabus, M., Bonfils, X., Moutou, C., Boisse, I., Delfosse, X., Desort, M., Eggenberger, A., Ehrenreich, D., Forveille, T., Lagrange, A.-M., Lovis, C., Mayor, M., Pepe, F., Perrier, C., Queloz, D., Santos, N. C., Ségransan, D., Udry, S., & Vidal-Madjar, A. 2008, A&A, 488, 763

Hogan, E., Burleigh, M. R., & Clarke, F. J. 2009, MNRAS, 396, 2074

Hut, P. 1981, A&A, 99, 126

Johnson, J. A., Bowler, B. P., Howard, A. W., Henry, G. W., Marcy, G. W., Isaacson, H., Brewer, J. M., Fischer, D. A., Morton, T. D., & Crepp, J. R. 2010, ApJL, 721, L153

Johnson, J. A., Clanton, C., Howard, A. W., Bowler, B. P., Henry, G. W., Marcy, G. W., Crepp, J. R., Endl, M., Cochran, W. D., MacQueen, P. J., Wright, J. T., & Isaacson, H. 2011, ApJS, 197, 26

Johnson, J. A., Fischer, D. A., Marcy, G. W., Wright, J. T., Driscoll, P., Butler, R. P., Hekker, S., Reffert, S., & Vogt, S. S. 2007, ApJ, 665, 785

Johnson, J. A., Huber, D., Boyajian, T., Brewer, J. M., White, T. R., von Braun, K., Maestro, V., Stello, D., & Barclay, T. 2014, ApJ, 794, 15

Jura, M. 2003, ApJL, 584, L91

—. 2006, ApJ, 653, 613

—. 2008, AJ, 135, 1785

Jura, M., Farihi, J., & Zuckerman, B. 2009, AJ, 137, 3191

Kalirai, J. S., Hansen, B. M. S., Kelson, D. D., Reitzel, D. B., Rich, R. M., & Richer, H. B. 2008, ApJ, 676, 594

Katz, B., Dong, S., & Malhotra, R. 2011, Physical Review Letters, 107, 181101

Kenyon, S. J. & Bromley, B. C. 2004, AJ, 127, 513

Kilic, M., von Hippel, T., Leggett, S. K., & Winget, D. E. 2006, ApJ, 646, 474

Kiseleva, L. G., Eggleton, P. P., & Mikkola, S. 1998, MNRAS, 300, 292

Klein, B., Jura, M., Koester, D., & Zuckerman, B. 2011, ApJ, 741, 64

Klein, B., Jura, M., Koester, D., Zuckerman, B., & Melis, C. 2010, ApJ, 709, 950

Knutson, H. A., Fulton, B. J., Montet, B. T., Kao, M., Ngo, H., Howard, A. W., Crepp, J. R., Hinkley, S., Bakos, G. Á., Batygin, K., Johnson, J. A., Morton, T. D., & Muirhead, P. S. 2014, ApJ, 785, 126

Koester, D. 2009, A&A, 498, 517

Koester, D. & Wilken, D. 2006, A&A, 453, 1051

Kozai, Y. 1962, AJ, 67, 591

Li, G., Naoz, S., Kocsis, B., & Loeb, A. 2014a, ApJ, 785, 116

—. 2015, ArXiv e-prints

Li, G., Naoz, S., Valsecchi, F., Johnson, J. A., & Rasio, F. A. 2014b, ApJ, 794, 131

Lidov, M. L. 1962, Planet. Space Sci., 9, 719

Lin, D. N. C., Bodenheimer, P., & Richardson, D. C. 1996, Nature, 380, 606

Lithwick, Y. & Naoz, S. 2011, ApJ, 742, 94

Lloyd, J. P. 2011, ApJL, 739, L49

—. 2013, ApJL, 774, L2

Löckmann, U., Baumgardt, H., & Kroupa, P. 2008, ApJL, 683, L151

Löhne, T., Krivov, A. V., & Rodmann, J. 2008, ApJ, 673, 1123

Maciejewski, G., Errmann, R., Raetz, S., Seeliger, M., Spaleniak, I., & Neuhäuser, R. 2011, A&A, 528, A65

Mardling, R. A. & Aarseth, S. J. 2001, MNRAS, 321, 398

Maxted, P. F. L., Marsh, T. R., & Moran, C. K. J. 2000, MNRAS, 319, 305

Mayor, M. & Queloz, D. 1995, Nature, 378, 355

Mullally, F., Coughlin, J. L., Thompson, S. E., Rowe, J., Burke, C., Latham, D. W., Batalha, N. M., Bryson, S. T., Christiansen, J., Henze, C. E., Ofir, A., Quarles, B., Shporer, A., Van Eylen, V., Van Laerhoven, C., Shah, Y., Wolfgang, A., Chaplin, W. J., Xie, J.-W., Akeson, R., Argabright, V., Bachtell, E., Barclay, T., Borucki, W. J., Caldwell, D. A., Campbell, J. R., Catanzarite, J. H., Cochran, W. D., Duren, R. M., Fleming, S. W., Fraquelli, D., Girouard, F. R., Haas, M. R., Hełminiak, K. G., Howell, S. B., Huber, D., Larson, K., Gautier, III, T. N., Jenkins, J. M., Li, J., Lissauer, J. J., McArthur, S., Miller, C., Morris, R. L., Patil-Sabale, A., Plavchan, P., Putnam, D., Quintana, E. V., Ramirez, S., Silva Aguirre, V., Seader, S., Smith, J. C., Steffen, J. H., Stewart, C., Stober, J., Still, M., Tenenbaum, P., Troeltzsch, J., Twicken, J. D., & Zamudio, K. A. 2015, ApJS, 217, 31

Murray, C. D. & Dermott, S. F. 2000, Solar System Dynamics (Cambridge University Press)

Mustill, A. J., Veras, D., & Villaver, E. 2014, MNRAS, 437, 1404

Naoz, S. & Fabrycky, D. C. 2014, ApJ, 793, 137

Naoz, S., Farr, W. M., Lithwick, Y., Rasio, F. A., & Teyssandier, J. 2011, Nature, 473, 187

—. 2013a, MNRAS, 431, 2155

Naoz, S., Farr, W. M., & Rasio, F. A. 2012, ApJL, 754, L36

Naoz, S., Kocsis, B., Loeb, A., & Yunes, N. 2013b, ApJ, 773, 187

Nordhaus, J. & Spiegel, D. S. 2013, MNRAS, 432, 500

O'Toole, S. J., Tinney, C. G., Jones, H. R. A., Butler, R. P., Marcy, G. W., Carter, B., & Bailey, J. 2009, MNRAS, 392, 641

Paquette, C., Pelletier, C., Fontaine, G., & Michaud, G. 1986, The Astrophysical Journal Supplement Series, 61, 197

Passy, J.-C., Mac Low, M.-M., & De Marco, O. 2012, ApJL, 759, L30

Paxton, B., Bildsten, L., Dotter, A., Herwig, F., Lesaffre, P., & Timmes, F. 2011, ApJS, 192, 3

Paxton, B., Cantiello, M., Arras, P., Bildsten, L., Brown, E. F., Dotter, A., Mankovich, C., Montgomery, M. H., Stello, D., Timmes, F. X., & Townsend, R. 2013, ApJS, 208, 4

Petrovich, C. 2015, ApJ, 799, 27

Pitjeva, E. V. 2005, Solar System Research, 39, 176

Prodan, S., Murray, N., & Thompson, T. A. 2013, ArXiv e-prints

Quillen, A. C. & Faber, P. 2006, MNRAS, 373, 1245

Rasio, F. A. & Ford, E. B. 1996, Science, 274, 954

Rasio, F. A., Tout, C. A., Lubow, S. H., & Livio, M. 1996, ApJ, 470, 1187

Reach, W. T., Kuchner, M. J., von Hippel, T., Burrows, A., Mullally, F., Kilic, M., & Winget, D. E. 2005, ApJL, 635, L161

Rieke, G. H., Su, K. Y. L., Stansberry, J. A., Trilling, D., Bryden, G., Muzerolle, J., White, B., Gorlova, N., Young, E. T., Beichman, C. A., Stapelfeldt, K. R., & Hines, D. C. 2005, ApJ, 620, 1010

Schlaufman, K. C. & Winn, J. N. 2013, ApJ, 772, 143

Socrates, A., Katz, B., & Dong, S. 2012, ArXiv e-prints

Spitale, J. & Greenberg, R. 2001, Icarus, 149, 222

—. 2002, Icarus, 156, 211

Sumi, T., Bennett, D. P., Bond, I. A., Udalski, A., Batista, V., Dominik, M., Fouqué, P., Kubas, D., Gould, A., Macintosh, B., Cook, K., Dong, S., Skuljan, L., Cassan, A., Abe, F., Botzler, C. S., Fukui, A., Furusawa, K., Hearnshaw, J. B., Itow, Y., Kamiya, K., Kilmartin, P. M., Korpela, A., Lin, W., Ling, C. H., Masuda, K., Matsubara, Y., Miyake, N., Muraki, Y., Nagaya, M., Nagayama, T., Ohnishi, K., Okumura, T., Perrott, Y. C., Rattenbury, N., Saito, T., Sako, T., Sullivan, D. J., Sweatman, W. L., Tristram, P. J., Yock, P. C. M., MOA Collaboration, Beaulieu, J. P., Cole, A., Coutures, C., Duran, M. F., Greenhill, J., Jablonski, F., Marboeuf, U., Martioli, E., Pedretti, E., Pejcha, O., Rojo, P., Albrow, M. D., Brillant, S., Bode, M., Bramich, D. M., Burgdorf, M. J., Caldwell, J. A. R., Calitz, H., Corrales, E., Dieters, S., Dominis Prester, D., Donatowicz, J., Hill, K., Hoffman, M., Horne, K., Jørgensen, U. G., Kains, N., Kane, S., Marquette, J. B., Martin, R., Meintjes, P., Menzies, J., Pollard, K. R., Sahu, K. C., Snodgrass, C., Steele, I., Street, R., Tsapras, Y., Wambsganss, J., Williams, A., Zub, M., PLANET Collaboration, Szymański, M. K., Kubiak, M., Pietrzyński, G., Soszyński, I., Szewczyk, O., Wyrzykowski, Ł., Ulaczyk, K., OGLE Collaboration, Allen, W., Christie, G. W., DePoy, D. L., Gaudi, B. S., Han, C., Janczak, J., Lee, C.-U., McCormick, J., Mallia, F., Monard, B., Natusch, T., Park, B.-G., Pogge, R. W., Santallo, R., & μFUN Collaboration. 2010, ApJ, 710, 1641

Teyssandier, J., Naoz, S., Lizarraga, I., & Rasio, F. A. 2013, ApJ, 779, 166

Thompson, T. A. 2011, ApJ, 741, 82

Triaud, A. H. M. J., Collier Cameron, A., Queloz, D., Anderson, D. R., Gillon, M., Hebb, L., Hellier, C., Loeillet, B., Maxted, P. F. L., Mayor, M., Pepe, F., Pollacco, D., Ségransan, D., Smalley, B., Udry, S., West, R. G., & Wheatley, P. J. 2010, A&A, 524, A25

Trujillo, C. A. & Brown, M. E. 2001, ApJL, 554, L95

Veras, D., Mustill, A. J., Bonsor, A., & Wyatt, M. C. 2013, MNRAS, 431, 1686

Villaver, E. & Livio, M. 2007, ApJ, 661, 1192

Villaver, E., Livio, M., Mustill, A. J., & Siess, L. 2014, ApJ, 794, 3

von Hippel, T., Kuchner, M. J., Kilic, M., Mullally, F., & Reach, W. T. 2007, ApJ, 662, 544

Walsh, K. J., Morbidelli, A., Raymond, S. N., O'Brien, D. P., & Mandell, A. M. 2011, Nature, 475, 206

Weidemann, V. 2000, A&A, 363, 647

Weidenschilling, S. J. 1977, Ap&SS, 51, 153

Weidenschilling, S. J. & Marzari, F. 1996, Nature, 384, 619

Winn, J. N., Fabrycky, D., Albrecht, S., & Johnson, J. A. 2010, ApJL, 718, L145

Wisdom, J. 1980, AJ, 85, 1122

—. 1982, AJ, 87, 577

Wood, M. A. 1992, ApJ, 386, 539

Wright, J. T., Fakhouri, O., Marcy, G. W., Han, E., Feng, Y., Johnson, J. A., Howard, A. W., Fischer, D. A., Valenti, J. A., Anderson, J., & Piskunov, N. 2011, PASP, 123, 412

Wyatt, M. C. 2008, ARAA, 46, 339

Wyatt, M. C., Smith, R., Greaves, J. S., Beichman, C. A., Bryden, G., & Lisse, C. M. 2007, ApJ, 658, 569

Xu, S. & Jura, M. 2012, ApJ, 745, 88

Zahn, J.-P. 1977, A&A, 57, 383

Zuckerman, B. & Becklin, E. E. 1987, Nature, 330, 138

Zuckerman, B., Koester, D., Melis, C., Hansen, B. M., & Jura, M. 2007, ApJ, 671, 872

Zuckerman, B., Koester, D., Reid, I. N., & Hünsch, M. 2003, ApJ, 596, 477

Zuckerman, B., Melis, C., Klein, B., Koester, D., & Jura, M. 2010, ApJ, 722, 725